APPLICATIONS OF TAP-NDE TECHNIQUE TO NON-CONTACT ULTRASONIC INSPECTION IN TUBULARS

A Dissertation

by

MARTIN EDUARDO BALTAZAR-LOPEZ

Submitted to the Office of Graduate Studies of
Texas A&M University
in partial fulfillment of the requirements for the degree of

DOCTOR OF PHILOSOPHY

December 2003

Major Subject: Interdisciplinary Engineering

APPLICATIONS OF TAP-NDE TECHNIQUE TO NON-CONTACT ULTRASONIC INSPECTION IN TUBULARS

A Dissertation

by

MARTIN EDUARDO BALTAZAR-LOPEZ

Submitted to the Office of Graduate Studies of
Texas A&M University
in partial fulfillment of the requirements for the degree of

DOCTOR OF PHILOSOPHY

Approved as to style and content by:

Christian P. Burger (Co-Chair of Committee)	Ravinder Chona (Co-Chair of Committee)
Chii-Der Suh (Member)	Henry Taylor (Member)
Hans Schuessler (Member)	Karen Butler-Purry (Head of Department)

December 2003

Major Subject: Interdisciplinary Engineering

ABSTRACT

Applications of TAP-NDE Technique to Non-Contact
Ultrasonic Inspection in Tubulars. (December 2003)

Martin Eduardo Baltazar-Lopez, B.S., Inst. Tec. De Aguascalientes, Mexico;
M.S., Centro Nacional de Investigación y Desarrollo Tecnológico, Mexico
Co-Chairs of Advisory Committee: Dr. Christian P. Burger
Dr. Ravinder Chona

The possibility and feasibility of experimental detection of localized defects in tubes using laser-induced ultrasonic wave approach through Thermo Acousto Photonic Non Destructive Evaluation (TAP-NDE) and Signal processing through wavelet transform is examined in this research. Guided waves in cylindrical surfaces provide solutions for detection of different defects in the material. Several experiments were conducted to this respect. Wave propagation in both axial and circumferential directions was studied. The dispersive wave propagation of ultrasonic waves in hollow cylinders has been investigated experimentally, primarily for use in non-contact and nondestructive inspections of pipes and tubes. The laser ultrasonic waves propagated in cylindrical waveguides are particularly attractive because of their unique characteristics in the applications of nondestructive evaluation (NDE). Contrary to studies making use of only axially symmetric guided waves in hollow cylinders, here are analyzed also non-axisymmetric waves. The analysis of data is made by using the Gabor wavelet transform. The capability of modeling the guided wave dispersion in hollow cylinders is used in developing guided wave experimental techniques for flaw detection. Good agreement was obtained when comparing the dispersion spectra between theory and experimentation. Measurement of group velocities of guided waves, which are obtained directly from the wavelet transform coefficients, can be used to determine allocation and sizing of flaws.

DEDICATION

I dedicate this work to my family, who with their unconditional love has been the light that guides my life. My wife Crisanta, with their love and affection, always in disposition to understand me and to impel me, Axel with their tenderness and imagination and Uziel with his singular smile and pranks make of every day a special day to live. Without them it had been not possible to conclude this work. Thanks to God, the Creator, to give me the opportunity of this precious life.

Porque la sabiduría entrará en tu corazón y el conocimiento será grato a tu alma. Proverbios 2:10.

For wisdom will enter your heart and knowledge will be pleasant to your soul. Proverbs 2:10.

ACKNOWLEDGEMENTS

I would like to thank Dr. Chris Burger for his advice and patience during this research project. His vision, wisdom and passion as an engineer and as a professor will always be greatly appreciated. I am proud to be part of the many generations influenced by his enthusiasm and challenging thinking.

I am deeply grateful to Dr. Ravi Chona for his unconditional support, especially on critical moments during my stay at this great university. His ideas and suggestions led into large improvements of the research project. It has been my privilege to work with him.

My deep appreciation goes to Dr. Suh for his continuous and valuable encouragement, for his "short lectures" that really helped me to understand wavelets, for letting me share my frustrations with him and for his generously given time to discuss several topics of this project.

I would like to express my gratitude to Dr. Schuessler and Dr. Taylor for serving on my doctoral committee and for taking the time to read and review this manuscript.

I would like to thank all my professors, classmates, and personnel of the mechanical engineering department, especially Ms. Kim Moses whose readiness and support has been invaluable throughout these years.

Finally, I am thankful to the government of México for their financial support through the Consejo Nacional de Ciencia y Tecnología (CONACYT) and the Centro Nacional de Investigación y Desarrollo Tecnológico (CENIDET), to carry out my doctoral studies.

TABLE OF CONTENTS

Page

LIST OF FIGURES

FIGURE Page

FIGURE Page

FIGURE Page

FIGURE Page

FIGURE Page

LIST OF SYMBOLS

ℓ	travel distance of the propagating wave
ϕ and ψ	wave potentials
ψ	analyzing function (or wavelet function).
ω	angular frequency
ρ	mass density
δ	nondimensional wave number
γ	number of oscillations in the Gabor wavelet
ν	Poisson's ratio
α	wave number
Ψ	wavelet transform
ψ^*	complex conjugate of the analyzing function (or wavelet function).
σ_{ij}	components of stress in Cartesian coordiantes if (x,y,z) and components of stress in cylindical coordiantes if (x,θ,z)
α_l	wave number of the longitudinal mode
α_R	Rayleigh wave number
α_t	wave number of the transverse mode
a	scale parameter of the wavelet transform
A_0	first antisymmetric Lamb mode
A_1, A_2, B_1, B_2	arbitrary constants,
b	translation parameter of the wavelet transform
c_g	group velocity
c_l	longitudinal wave velocity
c_o	velocity of long waves in a bar
c_p	phase velocity
c_R	Rayleigh wave velocity
c_t	transverse wave velocity

D	plate flexural modulus.
d_s	spot diameter
E	elastic modulus
$e_{i,j}$	components of strain
E_p	plate compressional modulus
f	frequency
$F_{i,j}$	elements of the characteristic frequency equation (i,j=1..5)
G	shear modulus
h	thickness of wall
I	moment of inertia
k_θ	thickness-shear adjustment coefficient in circunferential direction
k_x	thickness-shear adjustment coefficient in axial direction
L	longitudinal wavelength
$m=h/R$	ratio of wall thickness to mean radius of hollow cylinder
M_{ij}	moment resultant ($i,j = x, \theta$)
n	number of waves propagating circumferentially
N_{ij}	normal force resultant ($i,j = x, \theta$)
Q_i	shear force resultant ($i = x, \theta$)
R	mean radius of a tubular (hollow cylinder)
s	nondimensional phase wave velocity
s	velocity ratio (c_p/c_t)
S_0	first symmetric Lamb mode
S_i	dispersive modes in cylindrical waveguides (i=1,2,…)
t	time
U	longitudinal particle displacement in x-direction
u_x, u_θ,u_z	axial,tangential and radial components of displacement, respectively
V	particle displacement in y-direction
W	transverse particle displacement in z direction
x,θ,z	cylindical coordiantes

x,y,z	Cartesian coordinates
φ_x	angle of rotation of a normal to the middle surface in the x-z plane
$\varphi\theta$	angle of rotation of a normal to the middle surface in the x-θ plane

CHAPTER I

INTRODUCTION

Detection of material defects including voids and surface cracks in pipelines is a very important issue for the energy and petrochemical industry; as such, there is a need for a technique feasible for inspecting pipes in the field rapidly and non-destructively.

Ultrasonic testing is one of the most widely used nondestructive evaluation (NDE) techniques in engineering practice. However, traditional ultrasonic techniques, using contact transducers, are not well suited to interrogate cylindrical specimens, because such techniques encounter problems associated with the curvature, the complicated nature of the reflected waveforms and accessibility difficulties. Therefore, there is a necessity of developing a more robust ultrasonic nondestructive method to detect these defects before failure occurs. The current methods of detection other than image acquisition and processing[1] ,a.k.a. computer vision, are invasive in the sense that they interfere with the ultrasonic signals because they are in direct contact with the surface of the specimen; therefore the sensor itself disturbs the wave propagation mistaking the signal being detected. Additionally, contact transducers that are needed to initiate and obtain interrogating signals in the process of testing need to be located on surfaces, which sometimes are difficult to reach. Some existing techniques use laser-generated ultrasound, and the aspect of signal detection associated with these techniques is often realized by the use of contact transducers and thus invasive in nature.

An alternative to the transducer-based methods is to employ non-contact and non-invasive guided wave techniques to characterize the location and sizing of defects.

This dissertation follows the style of *Experimental Mechanics.*

By coupling optical detection of ultrasound and laser ultrasonic generation, it is possible to implement a powerful inspection system for many structures and materials.

These electro-optic ultrasonic methodologies have the advantages of being remote, of using the geometry of the layered cylinder to their advantage, and of being well suited to real- time analysis. While guided waves have been commonly used to interrogate simple geometries such as beams, solid rods, and plates however the application to cylindrical geometries is very limited.

One such laser-optic technique that has been successfully applied[2,3,4] to the characterization of metallic and non-metallic materials of various types of geometry was employed to demonstrate the feasibility of real-time, non-contact inspection of tubulars. The technique consists of the application of Thermo-Acoustic-Photonic Non-Destructive Evaluation (TAP-NDE)[5] using a pulsed laser as the generation source and an interferometric sensing system referred to as a Fiber Tip Interferometer (FTI) to acquire the signals. It is noted that most of the non-contact and non-invasive techniques reported in the literature have been developed and applied to survey flat surfaces only [6,7]. In this work, the generation and propagation of thermally induced broadband ultrasound in tubulars are experimentally studied. More specifically, the dispersion of the broadband ultrasound, as revealed by employing wavelets, is used to facilitate the detection of surface defects. Because wavelets are closely related to the concept of a filter bank[8], an algorithm effective for pipe and tube inspection can be easily implemented into digital hardware for real-time field applications. In the past, the wavelet analysis has been used mainly in acoustic emission techniques[9] and composite materials in the case of Laser-generated waves[10].

An important consideration in this study is the dispersion along curved surfaces. For Rayleigh waves one must distinguish between convex surfaces, and concave surfaces.

There are several studies on wave propagation on curved surfaces, most of them restricted to plane problem on solid cylinder.

The expanded study for hollow cylinders and the mathematical approach will be presented along with the theoretical basis on which the dispersion phenomenon is based. This would serve as a starting point and reference for the research being done because both Rayleigh waves and Lamb waves behave differently in plane surfaces than in curved surfaces.

Also for some applications (i. e. for on-line inspection and quality control), it is important to measure the properties non-destructively on the parts to be used. The study of dispersion of waves offers wide possibilities in this respect. The guided wave technique based on dispersion has been used for inspecting aircraft joints by Hansch et al.[11], and for defect detection in pipes by Lowe et al.[12] and by Park et al.[13]. A different perspective on the study of low frequency guided waves is used by León and Maze[14], where an isolation and identification of resonances is used to detect circumferential waves. Even stress distribution can be determined via ultrasonic wave dispersion as investigated by Ditri and Hongerholt[15]. Koshiba et al.[16] used finite-element method to predict dispersion characteristics of acoustic waves in cylindrically layered wave-guides. For the applications mentioned above, a thorough knowledge of the propagation characteristics of the waves, used from a theoretical and an experimental viewpoint, is essential.

The theory of waves on cylinders and their geometric dispersion, which is the phenomena by which a stress pulse changes shape as it propagates, is studied. The challenge of using guided waves is due to the complexity of the received signals, caused by multiple reflections and mode conversions of the bulk waves off the boundary surfaces of the structure (as they propagate over many wavelengths) and the resulting interference between the different rays. These phenomena (called geometric dispersion) result in signals of different frequency content propagating at different speeds within the structure. Therefore, understanding dispersion is a critical first step for understanding guided waves. The so-called dispersion curves relate how the phase velocity of a given normal mode changes as a function of frequency. Dispersion curves also provide valuable information concerning the normal modes in the structure being studied.

The dispersion relation of a dispersive medium is directly related to phase spectrum of a broadband pulse.

The wave velocity known also as phase velocity is

$$c_p = \frac{\omega}{\alpha} \tag{1.1}$$

Where ω= frequency, and α = wave number.

When the phase velocity is a function of its frequency or wavelength, then the propagating medium is dispersive. For tubulars, this dispersion is due to geometry. By definition, the group velocity of the wave is

$$c_g = \frac{d\omega}{d\alpha} = c_p + \alpha \frac{dc_p}{d\alpha} \tag{1.2}$$

In order to determine the group velocity by using phase spectral analysis it is necessary to make multiple measurements of the phase versus frequency of continuous waves. The technique was developed originally using the Fourier-analyzed pulse to evaluate its phase function[17]. This method was extended to broadband excitation signals, which excite multiple propagating modes[18].

For this work, instead of Fourier transforms, Wavelets transforms are used to get the dispersion as group velocity directly from the peaks of wavelet coefficients.

Several methods have been developed for dispersion analysis. Those, which are intended for single or dual mode analysis [17], i.e. where a Phase Spectra Analysis is introduced. This work was extended to multiple modes [18], where a 2-dimensional FFT-based method was developed, which maps over frequency and time domains. More recently those concepts were applied using wavelet analysis instead of FFT [19,20]. Two-dimensional-FFT-based dispersion curves of broadband laser generated waves in cylinders were developed[21].

In a more recent theoretical study, dispersive phase and group velocities are evaluated by using harmonic wavelet transform[22]. Dispersion curves in plates by using broadband laser ultrasonics were studied[23,24]. A different signal processing technique for capturing dispersion effects of multi-mode nature is based on the so-called re-assignation of spectrogram[25] claims to clearly separate dispersion effects from those due to a flaw.
In another study, the propagation of circumferential waves in an assumed infinitely long hollow cylinder with an inner shaft is examined[26].

1.1 Motivation of this Research

The majority of the existing methods for pipe inspection are invasive and use narrow-band transducer technology which constitute an ineffective way to get a reliable study of wave dispersion on cylindrical surfaces and consequently voids detection. Yet, transducers introduce additional complications (couplant use, contact, and frequency bias) that complicate the signals. Some of them present a lack of resolution due to unavailability of analysis tools in the past and ineffectiveness of others. Also studies of the dispersion on pipes are very limited and rarely exploited using non-contact broadband generation techniques. This research would provide a substantially better understanding of wave dispersion on the inherently dispersive cylindrical surfaces. Application of numerical tools like wavelets allow enhanced resolution and improved insight into the studied phenomena. Unlike other methodologies actually used, the study presented in this dissertation will be a completely non-contact and non-invasive transducer technology for inspecting pipes along both the axial and the circumferential directions.

1.2 Organization of this Dissertation

This dissertation is organized as follows. Chapter I is an introduction. The theory of Elastic Wave Dispersion Phenomena on Hollow cylinders is given in Chapter II. Chapter III addresses the Gabor Wavelet Analysis. The experimental Setup for generation and detection of Ultrasonic waves in cylinders is detailed in Chapter IV. Results are presented in Chapter V. Chapter VI summarizes the conclusions and list suggestions for future work.

CHAPTER II

THEORY OF ELASTIC GUIDED WAVE DISPERSION ON HOLLOW CYLINDERS

2.1 Introduction

This research work is based on the study of guided waves. Contrary to bulk waves which refers to waves that propagate in infinite media, meaning that the waves travel in the bulk of the material and away from the boundaries. Guided waves are those that require a boundary for their existence[27]. Although bulk and guided waves are fundamentally different, they are actually governed for the same set of partial differential equations of motion. Mathematically, the main difference is that for bulk waves there are no free boundary conditions that need to be satisfied by the proposed solution. Contrarily, a guided wave solution must satisfy the governing wave equations as well as physical boundary conditions. Examples of guided waves are Stoneley waves, Rayleigh waves and Lamb waves, the names are inherited from the investigators who solved those problems respectively. The last two, Rayleigh and Lamb, are the more important kind of waves in ultrasonics. In this chapter will be detailed the basic concepts of guided wave analysis and its application to a cylindrical geometry.

2.2 Overview of Rayleigh Wave Theory

Rayleigh waves are free waves on the surface of a semi-infinite solid. Traction forces must vanish on the boundary and the waves must decay with depth.

According to Viktorov [28], the following wave equation,

$$\frac{\partial^2\phi}{\partial x^2}+\frac{\partial^2\phi}{\partial z^2}+\alpha_l{}^2\phi=0$$
$$\frac{\partial^2\psi}{\partial x^2}+\frac{\partial^2\psi}{\partial z^2}+\alpha_t{}^2\psi=0 \qquad (2.1)$$

describes either Lamb or Rayleigh waves as a function of the longitudinal and transverse wave potentials ϕ and ψ respectively. α_l and α_t are the wave numbers of the longitudinal and transverse modes. Fig. 2.1 shows the reference axis used when deriving the Rayleigh relations.

The particle displacements U (longitudinal) and W (transverse)

$$U=\frac{\partial\phi}{\partial x}-\frac{\partial\psi}{\partial z}$$
$$W=\frac{\partial\psi}{\partial x}+\frac{\partial\phi}{\partial z} \qquad (2.2)$$

represent displacements along the x and z axes as seen in Fig. 2.1.

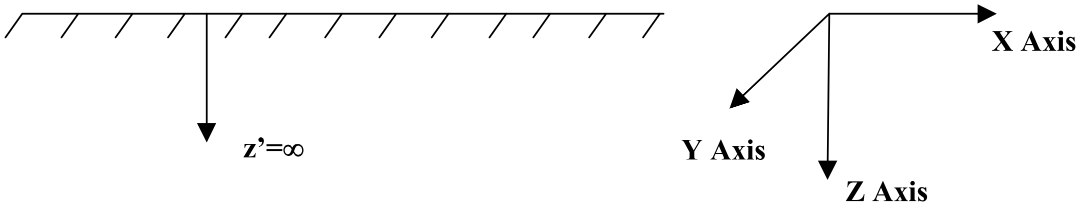

Fig. 2.1--Rayleigh reference axis.

For a Rayleigh wave propagating in the x-direction, the x-y plane describes the free surface of an infinite half space. The thickness z' determines the mode of wave propagation. Rayleigh type modes propagate in a medium with an infinite half space (z'=∞). Since an infinite half-space can never be physically achieved, the above statements imply that a "pure" Rayleigh wave can never occur. However, when the thickness of a medium is greater than two times the wavelength of the interrogating frequency, that waveform approximate the Rayleigh wave type characteristics. In other words, if the wavelength of the waveform is small enough, it will not realize that the opposite boundary exists and will propagate approximately as a wave in an infinite half-space.

Rayleigh waves represent elastic perturbations propagating near the free boundary of a solid and decaying with depth. These displacements can be calculated from the following representation of wave potentials ϕ and ψ:

$$\phi = Ae^{-qz}e^{i(\alpha x-\omega t)}$$

$$\psi = Be^{-sz}e^{i(\alpha x-\omega t)} \tag{2.3}$$

where A and B are arbitrary constants, $\alpha = \dfrac{2\pi f}{c_p}$ where α is the Rayleigh wave number, f is the frequency, and c_p is the phase velocity, and

$$q = \left(\alpha^2 - \alpha_l{}^2\right)^{-\frac{1}{2}} \text{ and } s = \left(k^2 - k_t{}^2\right)^{-\frac{1}{2}}$$

Equation (2.3) satisfies the wave equation (2.1). The negative radicals, e^{-qz} and e^{-sz}, in equation (2.3), indicate exponentially decaying motion with increasing depth. By definition, this indicates a surface or Rayleigh wave.

The conditions of the problem require that the stresses σ_{xz} and σ_{zz} go to zero at the boundary of the half space (z'=0) as seen in Fig. 2.1. This condition allows the development of the characteristic equation. Upon solving the characteristic equation, the solutions can be substituted into equation (2.3) to develop the `Rayleigh' wave potentials.

Using the Rayleigh wave potentials and the displacement relations in equation (2.3), a set of displacement components U and W are developed:

$$U_R = A\alpha_R(e^{-q_R z} - \frac{2q_R S_R}{\alpha_R^{\ 2} + S_R^{\ 2}} e^{-s_R z})\sin(\alpha_R x - \omega t)$$

$$W_R = Aq_R(e^{-q_R z} - \frac{2\alpha_R^{\ 2}}{\alpha_R^{\ 2} + S_R^{\ 2}} e^{-s_R z})\cos(\alpha_R x - \omega t) \tag{2.4}$$

In this equation, α_R is the wave number or roots from the characteristic equation, q_R and s_R are calculated as before (q and s) except that, instead of α, the value is α_R.

Fig. 2.2 shows the theoretical and experimental displacements plots for the laser-generated ultrasonic Rayleigh wave pulse on steel. Note that the relative amplitude of a single point-excited Rayleigh wave is dipolar representing a true pulse shape in contrast to the multi-pole representation obtained when using contact transducers. The multi-pole response is typical from contact transducers where internal reflections in the transducer and averaging over the length of the capture area pollute and distort the apparent pulse shape. For Figure 2.2, the theoretical displacements are calculated based on the next expression[29,30]:

$$\mathrm{h(t)} = (\ell - c_R t)e^{\frac{-4(\ell - c_R t)^2}{d_s^{\ 2}}} \tag{2.5}$$

where:

ℓ = propagation distance,

c_R = Rayleigh wave velocity,

t = time,

d_s = Generation point spot size.

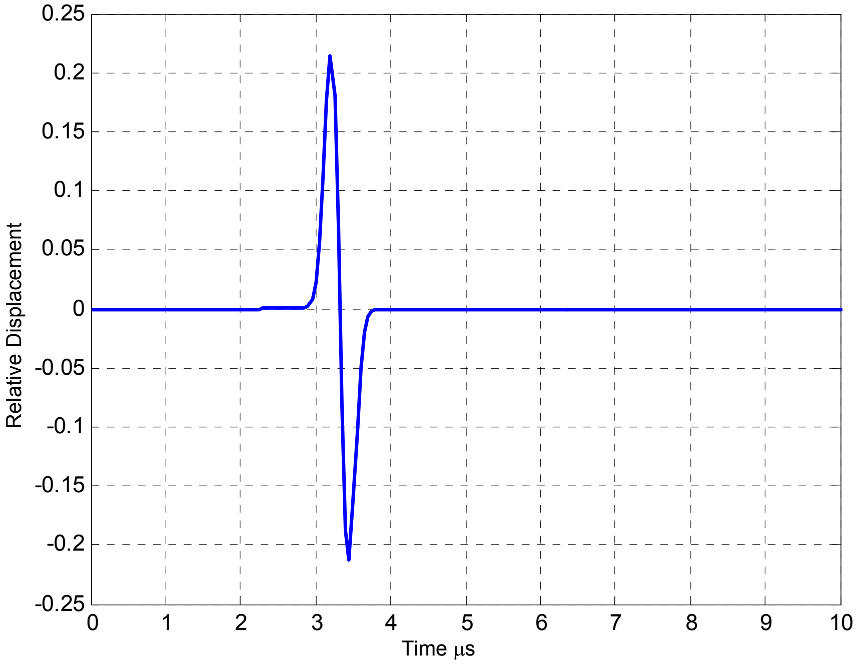

(a) Theoretical Single-point-Excited Rayleigh Wave

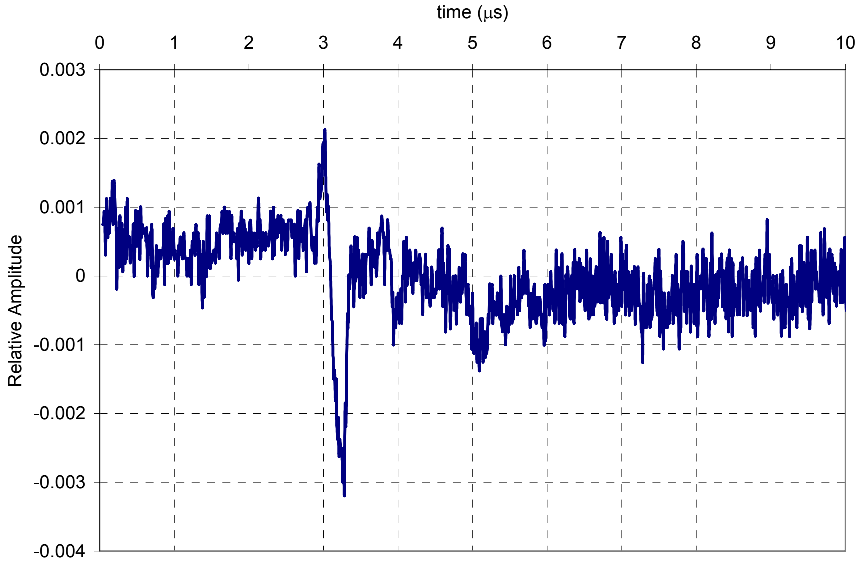

(b) Typical Rayleigh Wave (Single Pulse)

Figure 2.2--Out of plane displacement of a laser-generated Rayleigh wave on steel. (a) Theoretical (after Huang et al.[29] and Berthelot et al.[30]), (b) Experimental. Travel distance ℓ =10mm, spot size d_s= 1mm, Rayleigh wave velocity on steel c_R= 2.9 Km/s.

The next values were applied, for both calculation and experimental setup: Travel distance ℓ=10mm, Spot size d_s= 1mm, and for theoretical solution a nominal Rayleigh wave velocity on steel c_R= 2.9 Km/s, was assumed.

The Rayleigh displacements become more and more like Lamb displacements, which will be explained later, as the depth to wavelength ratio reduces.

Computer programs for calculation of theoretical single pulse Rayleigh wave (dipolar) is included in Appendix A. Multi-poled Displacement Components W_R and U_R; and stress σ_{zz}; of a Rayleigh wave are included in Appendix B.

Another important aspect of the Rayleigh wave is that it is not dispersive on flat free surfaces, that is, all of the frequencies travel at the same velocity. Since the characteristic equation and the transverse wave velocity, c_t, are not functions of frequency, the phase velocity (the rate of travel of a wave crest) and the group velocity (the velocity of a short pulse of waves) are the same. A schematic representation of particle motion on a steel surface due to such a Rayleigh wave is shown in figure 2.3.

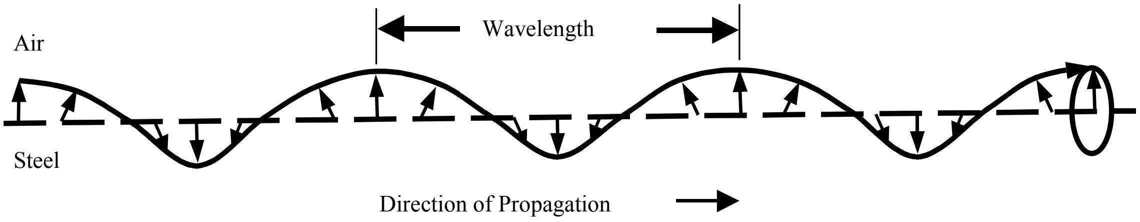

Fig. 2.3--Schematic representation of particle motion on a free steel surface due to a Rayleigh wave.

The main difference between Rayleigh waves and Lamb waves is the propagation mode. A Rayleigh mode develops when the waveform interacts with only one surface of a solid. In this case, the wave penetrates the medium to a depth of $2L_R$, which is twice the Rayleigh wavelength. The waveform will continue to propagate in the Rayleigh mode until the thickness of the solid approaches $2L_R$. When this thickness change occurs, the Rayleigh mode of propagation will transform into a Lamb type mode of propagation.

2.2 Lamb Wave Theory

The other important kind of guided wave in ultrasonics is the Lamb wave. The classical problem of Lamb wave propagation is associated with the wave motion in a homogeneous, isotropic plate with parallel traction-free upper and lower surfaces. A standard Cartesian coordinate system as shown in Figure 2.4 delimits the plate. The x-z plane defines the cross section while the x-y directions define the in-plane dimensions.

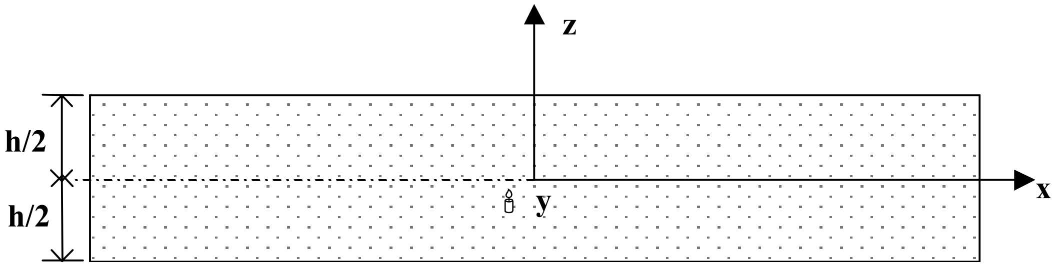

Figure 2.4--Cross section of a homogenous flat plate with thickness h. It is assumed to be in a state of plane strain in the x-z plane.

The plate is h units thick, z = h/2. Assume that U, V, and W represent displacements in the x, y, and z directions respectively. Assuming the plate in a state of plane strain, where the y dimension is large and the elastic wave is traveling in the x direction, the displacements and all partial differentials with respect to the y direction vanish. It is now possible to decompose the displacement field into scalar and vector potentials. A state of plane strain imposes the following conditions:

$$V = 0 \text{ and } \frac{\partial}{\partial \mathrm{y}} = 0 \tag{2.6}$$

As in Rayleigh wave formulation, the displacements can be decomposed using a scalar potential, ϕ, and a vector potential, ψ_i, (i = x,y,z) that satisfy the equation of motion for a homogeneous material. Consider decomposing the displacements in the x and z directions in the following form:

$$U = \frac{\partial \phi}{\partial x} + \frac{\partial \psi_y}{\partial z} \tag{2.7}$$

and

$$W = \frac{\partial \phi}{\partial z} - \frac{\partial \psi_y}{\partial x}. \tag{2.8}$$

The differential equations of motion must be satisfied by the potentials

$$\frac{\partial^2 \phi}{\partial x^2} + \frac{\partial^2 \phi}{\partial z^2} = \frac{1}{c_l^2}\frac{\partial^2 \phi}{\partial t^2} \tag{2.9}$$

and

$$\frac{\partial^2 \psi}{\partial x^2} + \frac{\partial^2 \psi}{\partial z^2} = \frac{1}{c_t^2}\frac{\partial^2 \psi}{\partial t^2} \tag{2.10}$$

again c_l and c_t are the longitudinal and transverse waves speeds of the material, respectively. Time harmonic solutions are assumed for plane waves traveling in the x-direction. Then the potentials are:

$$\phi = \Phi(z)\, e^{i(\alpha x - \omega t)} \tag{2.11}$$

and

$$\psi = \Psi(z)\, e^{i(\alpha x - \omega t)}, \tag{2.12}$$

where α represents the wavenumber, ω is the angular frequency, and t is time. Substituting these equations into the differential equations of motion and solving leads to:

$$\Phi(z) = A_1 \sin(p\, z) + A_2 \cos(p\, z) \tag{2.13}$$

and

$$\Psi(z) = B_1 \sin(q\,z) + B_2 \cos(q\,z) \;, \tag{2.14}$$

where

$$p^2 = \frac{\omega^2}{c_L^2} - \alpha^2 \,,\;\; q^2 = \frac{\omega^2}{c_T^2} - \alpha^2 \tag{2.15}$$

with A₁, A₂, B₁, and B₂ being arbitrary constants. Those constants as well as the dispersion equations are still unknown and can be determined by applying the traction-free boundary condition,

$$\sigma_{zx} = \sigma_{zz} \equiv 0 \text{ at } z = \pm\frac{h}{2} \tag{2.16}$$

Displacements and stresses within a plate are found by using equations (2.13) and (2.14).

The solution can be split into two sets of modes, due to the symmetry of the displacement equations. These two modes are known as symmetric and antisymmetric modes. However, this separation of waves into symmetric and antisymmetric modes is not a rule but an exception due to the geometrical symmetry. In hollow cylinders, for example, the structural asymmetry does not allow this separation and all the modes are coupled and then a more complicated theory must be applied. Similarly for anisotropic plates where plate wave modes exist but because of lack of symmetry, the separation into symmetric and antisymmetric modes is not possible unless the wave propagates along a symmetry axis of the plate[31]. The details in procedure to get the dispersion equations for plate waves can be found in several texts[27,32,33] The solution for the symmetric case can be found as

$$\frac{\tan(qh/2)}{\tan(ph/2)} = -\frac{4\,\alpha_s^{\,2}\,p\,q}{(q^2 - \alpha_s^2)^2} \tag{2.17}$$

while the solution for the antisymmetric case is given by

$$\frac{\tan(qh/2)}{\tan(ph/2)} = -\frac{(q^2 - \alpha_a^2)}{4\alpha_a^2 pq}. \tag{2.18}$$

Note the subscripts on wavenumbers in equations (2.17) and (2.18) correspond to the solutions of the symmetric and antisymmetric modes (α_s and α_a respectively). Schematics of symmetric and antisymmetric modes are shown in figure 2.5.

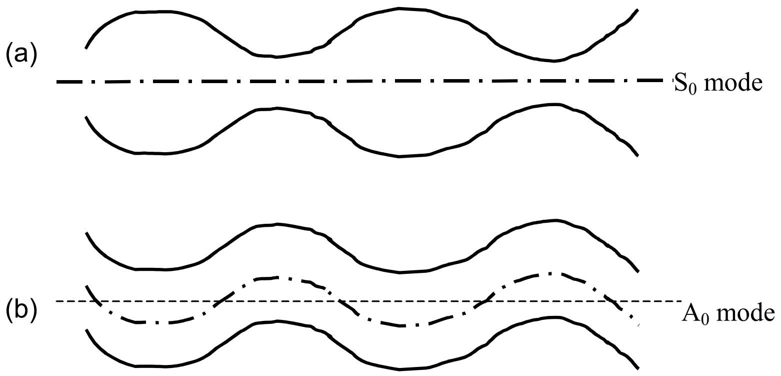

Fig. 2.5—Out of plane displacements of two surfaces of a flat plate for:(a)symmetric and (b) antisymmetric plate wave modes.

A Rayleigh wave is actually a combination of the first antisymmetric A_0 and first symmetric S_0 modes from the Lamb wave traveling at the same velocity.

2.3 Dispersion

Wave motion equations in hollow cylinders are based on the generalized wave equations for plates. However for the cylindrical case, the dispersion phenomena is present. Then a more complex study is needed. The dispersion effect can be easily visualized as a propagating pulse for which different frequencies travel at different velocities. The pulse length expands over time domain, as shown in Fig 2.6.

As the wave pulse propagates it expands in the time domain and its amplitude decreases. This later effect is not only necessarily due to dispersion but also from material damping. There are several factors, which can cause dispersion:

a. Material dispersion: There is frequency dependence of material constants (i.e. equivalent elastic module, dielectric constants),
b. Geometric Dispersion: Presence of specimen boundaries,
c. Scattering dispersion: Scattering of waves by densely distributed fine inhomogeneities in a material;
d. Dissipative dispersion: The absorption or dissipation of waves energy into heat or other forms of energy in an irreversible process; and

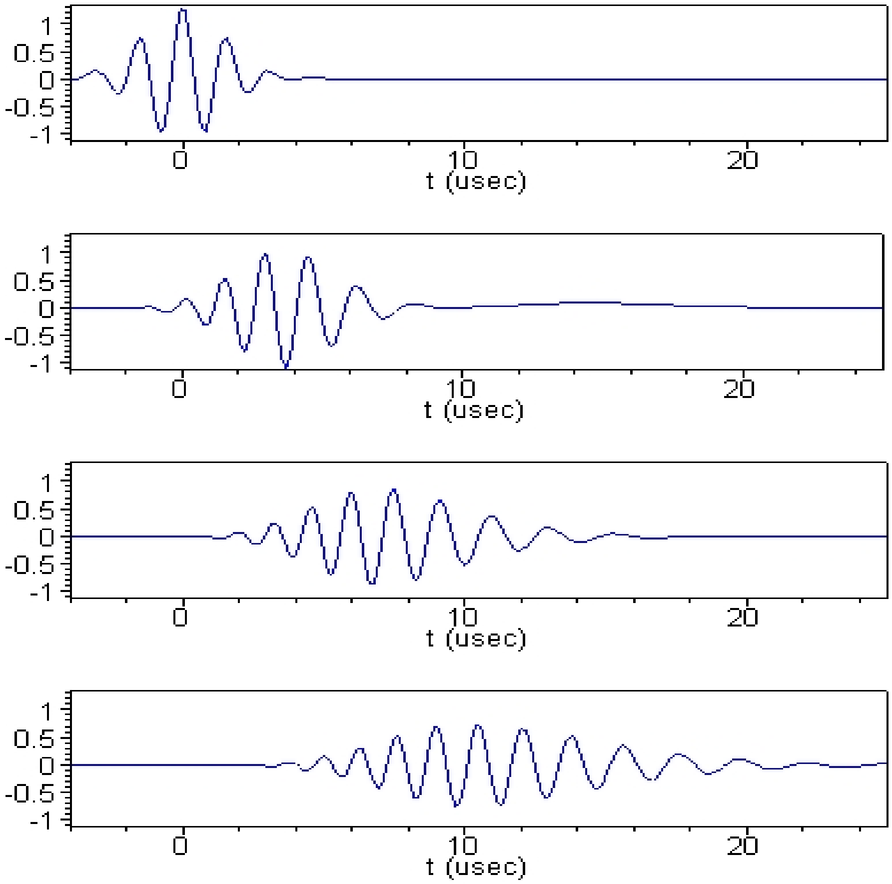

Fig. 2.6 --Dispersion effect (after Wilcox et al.[34]). Time domain out of plane displacement plots of a pulse at different times.

e. Non linear dispersion: There is a dependence of the wave speed on the wave amplitude.

For this case, it is assumed that the most significant dispersion effect in cylindrical shapes is the geometric dispersion caused by the boundaries of the internal and external cylindrical shapes.

If the midplane or neutral plane of the plate is taken as the plane of symmetry, the dispersion curves for the first two axisymmetric modes of propagation in circular cylindrical shells are shown in figure 2.7.

It can be noticed that a bar type behavior occurs at low values of wave number, characterized by the velocity c_o of infinitely long waves in a bar defined by

$$c_o = \sqrt{\frac{E}{\rho}} . \tag{2.19}$$

where E is the Young modulus and ρ is the mass density of the material.

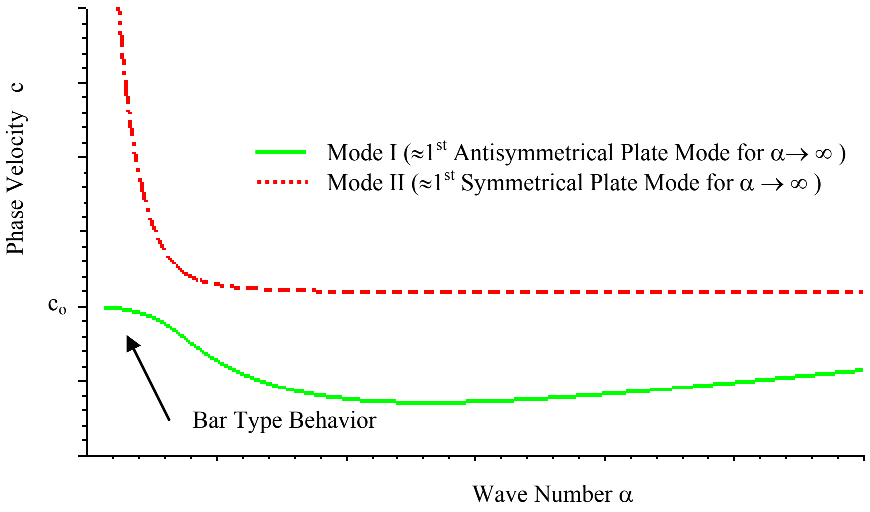

Fig 2.7--Characteristic dispersion behavior for the first two axisymmetric modes of waves in circular cylindrical shells, called mode I and mode II, respectively (after Mirsky and Herrmann[35]).

Most of the studies of wave dispersion are based on the three-dimensional equations of elasticity. Some examples of such studies are the theoretical treatment of propagating waves in solid rods and curved surfaces. These kinds of studies were restricted to plane problem (plain stress or plane strain) in cylindrical coordinates and on solid cylinders. The solution is expressed in terms of the potentials ϕ and φ of longitudinal and shear waves satisfying the compatibility equations and only the first mode (Mode I) is considered, which corresponds to the first antisymmetrical plate mode of the Rayleigh-Lamb equations in the short wavelength limit.

Mirsky[36] carried out a study of wave propagation in hollow and solid circular cylinders of transversely isotropic material. For hollow rods, however, various approximate theories studied by Herrmann and Mirsky [35,37] are applied. Heimann and Kolsky[38] have verified both theoretically and experimentally, that a mode corresponding to the symmetrical plate mode also exists for propagation in the axial direction in thin-walled tubes. In their experimental set-up they produced an axisymmetric stress pulse by longitudinal impact of a short cylindrical ring. They observed a high frequency component moving to the head of the pulse, with increasing distance from the point of impact, corresponding to the symmetrical plate mode, the maximum group velocity of which is about 4% larger than the maximum group velocity of the first mode.

The solution of the transient loading problems for wave propagation problems becomes rather difficult and time consuming, if the exact three-dimensional equations are used. Therefore, various approximate theories have been developed also for cylindrical shell problems. Love[39] derived a set of shell equations where bending effects, as well as the trapezoidal shape of the faces perpendicular to the cylinder axis is taken into account. Additionally, shear deformation and rotatory inertia effects are incorporated in a thick shell theory developed by Naghdi and Cooper[40]. In an even more complicated theory Herrmann and Mirsky[41] have also considered transverse normal stresses and obtained good agreement with the exact theory up to ratios of 1 of shell thickness to mean radius for the first mode of propagation.

To get reasonable results, the theory chosen is mainly determined by the ratios of thickness to wavelength and thickness to radius. In general, the higher these ratios, the more complex a theory must be used.

The Phase velocity of axially symmetric and non-axially symmetric waves in hollow cylinders has been determined by Mirsky and Herrmann[35]. They included a more general Timoshenko-type theory to include non-axially symmetric motions, and is able to describe a wider range of phenomena than the classical shell theories, which include only membrane and bending effects.

Gazis[42] used linear theory of elasticity to study the propagation of waves on hollow circular cylinders. By using the Helmholtz potentials for arbitrary values of the physical parameters involved, he obtained a characteristic equation appropriate to the circular hollow cylinder in addition to its numerical evaluation.

Goldsmith et al.[43] have observed the propagation of pulses on thin and medium-thick wall hollow cylinders. Steel spheres struck the specimens, yielding pulse duration of 20 to 40 microseconds, which correspond to a frequency content of up to 50 kHz. This is below the cut-off frequency of the second axisymmetric mode. The impact can therefore be described by a membrane-type shell theory, where a rod-like behavior is dominant and bending effects can be neglected. Dispersion is weak and due to radial inertia effects in this frequency domain. Reasonable agreement between theoretical results and experimental data was obtained.

The problem of axisymmetric waves in an orthotropic hollow cylinder has been solved by Shul'ga[44] by expanding the radial dependence of the displacement vector in a power series. In a later paper Shul'ga and Ramskaya[45] present a discussion of results. The analysis is limited to the case of particularly orthotropic materials, where the axes of orthotropy coincide with the coordinate lines of a cylindrical coordinate system with its axis of symmetry along the geometrical axis of the tube.

In the case of non orthotropic materials, coupling will exist between longitudinal stresses and tangential shear strains and vice versa, which in terms of waves means that the "torsional" and "axial" modes have general displacements with components in radial, axial and tangential directions.

For orthotropic materials, the principal axes of orthotropy are assumed to coincide with the axial, radial and circumferential directions of the tube.

In addition, Rulf[46] analyzed Rayleigh waves propagating on surfaces of variable curvature. However, these studies are based on contact transducers. A correlation and comparison between those results and experimental determination of dispersion of laser-generated waves will be discussed.

2.4 Mirsky-Herrmann Theory for Wave Motion on Hollow Cylinders

This theory is useful for this study because contrary to other theories that consider only axially symmetric motions, that is, wave propagating in the axial direction of the shell, this theory additionally considers non-axially symmetric waves in a cylindrical shell. This characteristic is particularly interesting because wave motion of laser generated waves is non-axially symmetric. In addition, this theory is complete in the sense that it considers shear effects in both the axial and circumferential direction and rotary inertia effects. Another benefit of using this theory is that it can be implemented easily in a computer program to obtain dispersion curves for thin or thick cylindrical shells.

Consider an infinite, cylindrical shell with mean radius *R* and thickness *h.* Let *x* be the axial coordinate, θ the polar angle, and *z* be the radial distance from the middle surface of the shell measured positively outwards. The definition of Geometrical Parameters and Coordinate System for the Cylindrical Shell are shown at Fig. 2.8. The components of the displacement in this coordinate system are designated by $\overline{u}_x, \overline{u}_\theta, \overline{u}_z$, whose dependence on the z coordinate normal to the middle surface is given by

$$\begin{aligned} \overline{u}_x(x,\theta,z,t) &= u(x,\theta,t) + z\varphi_x(x,\theta,t), \\ \overline{u}_\theta(x,\theta,z,t) &= v(x,\theta,t) + z\varphi_\theta(x,\theta,t), \\ \overline{u}_z(x,\theta,z,t) &= w(x,\theta,t) \end{aligned} \tag{2.20}$$

where *t* is time, *u,v,w* are seen to be the displacement components of a particle on the middle surface, *z=0,* φx and φθ are the angles of rotation of a normal to the middle surface in the *x-z* and $x\text{-}\theta$ planes, respectively.

In equation 2.20 the φx and φθ terms represent the axial and circumferential shear effects.

The basic steps of the theory involve, first, integration of the strain energy density expression across the shell thickness.

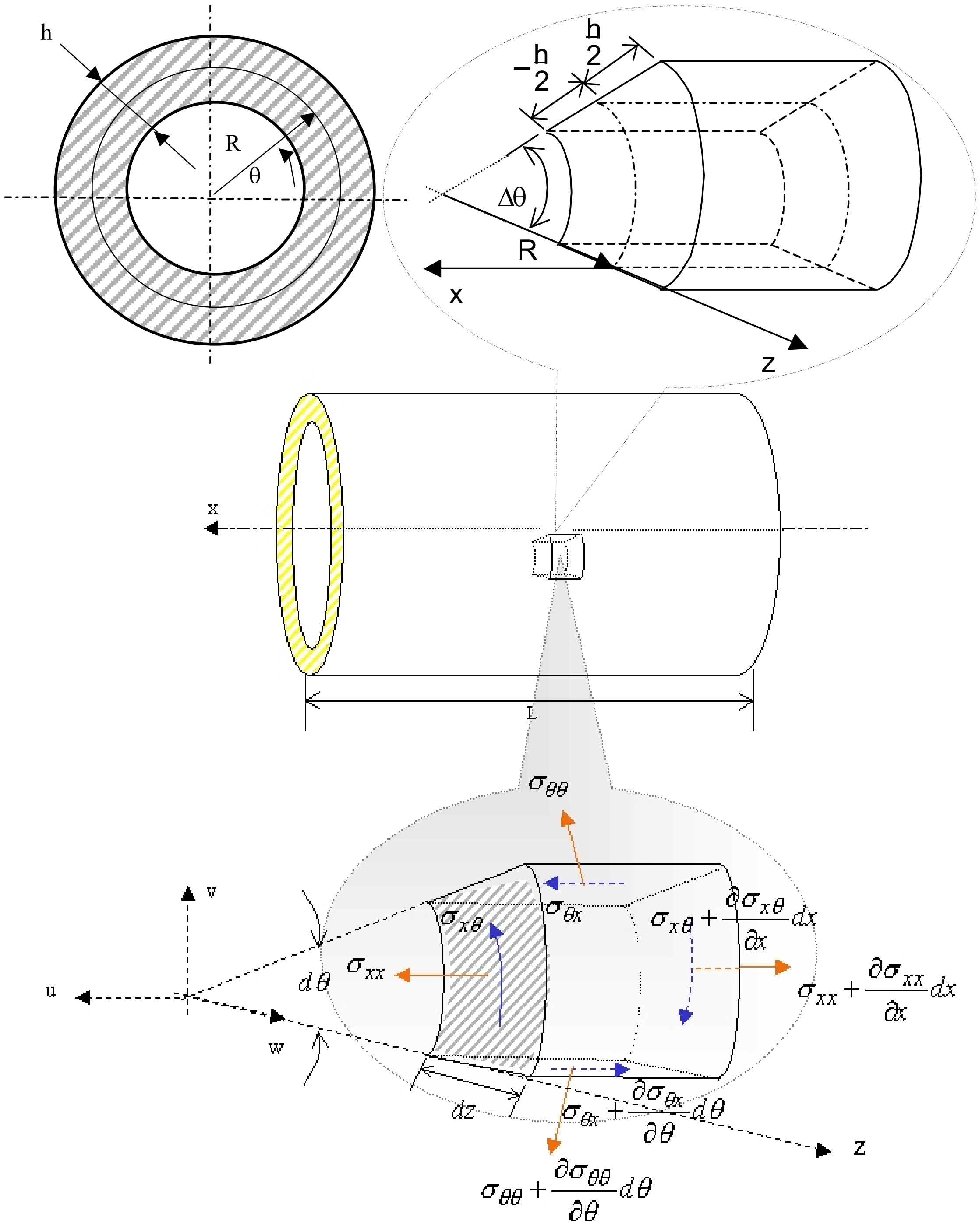

Figure 2.8—Reference system and stress element in a hollow cylinder.

This leads to the following definitions of the ten shell resultants which have been completely developed by Mirsky-Herrman[35,37,41] and will not be detailed here

$$N_{xx} = \int_{-h/2}^{h/2} \sigma_{xx}(1+z/R)dz \qquad \mathrm{M}_{x\theta} = \int_{-h/2}^{h/2} \sigma_{x\theta}(1+z/R)dz$$

$$M_{xx} = \int_{-h/2}^{h/2} \sigma_{xx}(1+z/R)zdz \qquad \mathrm{N}_{\theta x} = \int_{-h/2}^{h/2} \sigma_{x\theta}dz$$

$$N_{\theta\theta} = \int_{-h/2}^{h/2} \sigma_{\theta\theta}dz \qquad \mathrm{M}_{\theta x} = \int_{-h/2}^{h/2} \sigma_{x\theta}zdz \qquad (2.21)$$

$$M_{\theta\theta} = \int_{-h/2}^{h/2} \sigma_{\theta\theta}zdz \qquad \mathrm{Q}_{x} = \int_{-h/2}^{h/2} \sigma_{xz}(1+z/R)dz$$

$$N_{x\theta} = \int_{-h/2}^{h/2} \sigma_{x\theta}(1+z/R)dz \qquad \mathrm{Q}_{\theta} = \int_{-h/2}^{h/2} \sigma_{z\theta}dz$$

The kinetic energy is then developed. Using the two energy expressions in conjunction with Hamilton's principle, as detailed by Mirsky and Herrmann[37], leads to the shell stress equations of motion. The shell stress-strain-displacements are developed from Hooke's law. In obtaining the approximate plate theory, the effects of the stress σ_{zz} are dropped, following the process of Mindlin[47] for the flat plate theory. Even though this theory neglects the transverse normal stress still is valid for our problem of wave propagation because it includes the rotatory inertia and shear. Furthermore, the adjustment coefficients k_x, k_θ are introduced in conjunction with the strains ε_{xz}, $\varepsilon_{\theta z}$. The resulting stress-displacement equations are given by:

$$N_{xx} = E_p \frac{\partial u}{\partial x} + \frac{D}{R}\frac{\partial \varphi_x}{\partial x} + \frac{\nu\, E_p}{R}\left(w + \frac{\partial v}{\partial \theta} \right)$$

$$N_{\theta x} = Gh\frac{\partial v}{\partial x} + \frac{Gh}{R}\left(1 + \frac{Gh}{R} \right)\frac{\partial u}{\partial \theta} - \frac{GI}{R^2}\frac{\partial \varphi_x}{\partial \theta}$$

$$M_{xx} = \frac{D}{R}\left(\frac{\partial u}{\partial x} + R\frac{\partial \varphi_x}{\partial x} + \nu\frac{\partial \varphi_\theta}{\partial \theta} \right)$$

$$M_{\theta x} = GI\left(\frac{\partial \varphi_\theta}{\partial x} + \frac{1}{R^2}\frac{\partial u}{\partial \theta} + \frac{1}{R}\frac{\partial \varphi_x}{\partial \theta} \right)$$

$$N_{x\theta} = G\left(h\frac{\partial v}{\partial x} + \frac{I}{R}\frac{\partial \varphi_\theta}{\partial x} + \frac{h}{R}\frac{\partial u}{\partial \theta} \right)$$

$$N_{\theta\theta} = \left(\frac{E_p}{R} + \frac{D}{R^3} \right)\left(w + \frac{\partial v}{\partial \theta} \right) - \frac{D}{R^2}\frac{\partial \varphi_\theta}{\partial \theta} + \nu E_p \frac{\partial u}{\partial x} \tag{2.22}$$

$$M_{x\theta} = \frac{GI}{R}\left(\frac{\partial v}{\partial x} + R\frac{\partial \varphi_\theta}{\partial x} + \frac{\partial \varphi_x}{\partial \theta} \right)$$

$$M_{\theta\theta} = \frac{D}{R}\frac{\partial \varphi_\theta}{\partial \theta} - \frac{D}{R^2}\left(w + \frac{\partial v}{\partial \theta} \right) + D\nu\frac{\partial \varphi_x}{\partial x}$$

$$Q_x = k_x{}^2 Gh\left(\varphi_x + \frac{\partial w}{\partial x} \right)$$

$$Q_\theta = k_\theta{}^2 \frac{Gh}{R}\left(1 + \frac{h^2}{12R^2} \right)\left(\frac{\partial w}{\partial x} - \nu + R\varphi_\theta \right)$$

Where:

1) The ten shell resultants are:
   N_{ij} Normal Force Resultant(N)
   M_{ij} Moment Resultant (Nm)
   Qi Shear Force Resultant (N)

2) G is the shear modulus (N/m^2),

3) $E_p = Eh/(1-\nu^2)$ is the plate compressional modulus (N/m),

4) $I = h^3/12$ is the moment of inertia (m^3), and

5) $D = Eh^3/12(1-\nu^2)$ is the plate flexural modulus (Nm).

Neglecting body forces, the resulting five displacement equations of motion are:

$$\left[E_p\frac{\partial^2}{\partial x^2}+\frac{Gh}{R^2}\left(1+\frac{I}{hR^2}\right)\frac{\partial^2}{\partial\theta^2}-\rho h\frac{\partial^2}{\partial t^2}\right]u+\left[\frac{D}{R}\frac{\partial^2}{\partial x^2}-\frac{GI}{R^3}\frac{\partial^2}{\partial\theta^2}-\frac{\rho I}{R}\frac{\partial^2}{\partial t^2}\right]\varphi_x+$$

$$+\left[\frac{E_p(1+\nu)}{2R}\frac{\partial^2}{\partial x\partial\theta}\right]v+\left[\frac{\nu E_p}{R}\frac{\partial}{\partial x}\right]w=0, \tag{2.23a}$$

$$\left[\frac{D}{R}\frac{\partial^2}{\partial x^2}-\frac{GI}{R^3}\frac{\partial^2}{\partial\theta^2}-\frac{\rho I}{R}\frac{\partial^2}{\partial t^2}\right]u+\left[D\frac{\partial^2}{\partial x^2}+\frac{GI}{R^2}\frac{\partial^2}{\partial\theta^2}-k_x^2Gh-\rho I\frac{\partial^2}{\partial t^2}\right]\varphi_x+$$

$$+\left[\frac{D(1+\nu)}{2R}\frac{\partial^2}{\partial x\partial\theta}\right]\varphi_\theta+\left[-k_x{}^2Gh\frac{\partial}{\partial x}\right]w=0, \tag{2.23b}$$

$$\left[\frac{E_p(1+\nu)}{2R}\frac{\partial^2}{\partial x\partial\theta}\right]u+\left[Gh\frac{\partial^2}{\partial x^2}+\left(\frac{E_p}{R^2}+\frac{D}{R^4}\right)\frac{\partial^2}{\partial\theta^2}-k_\theta^2\frac{G}{R^2}\left(h+\frac{I}{R^2}\right)-\rho h\frac{\partial^2}{\partial t^2}\right]v+$$

$$+\left[\frac{GI}{R}\frac{\partial^2}{\partial x^2}-\frac{D}{R^3}\frac{\partial^2}{\partial\theta^2}+k_\theta^2\frac{G}{R}\left(h+\frac{I}{R^2}\right)-\frac{\rho I}{R}\frac{\partial^2}{\partial t^2}\right]\varphi_\theta$$

$$+\left[\frac{E_p}{R^2}+\frac{D}{R^4}+k_\theta^2\frac{G}{R^2}\left(h+\frac{I}{R^2}\right)\right]\frac{\partial w}{\partial\theta}=0, \tag{2.23c}$$

$$\left[\frac{D(1+\nu)}{2R}\frac{\partial^2}{\partial x\partial\theta}\right]\varphi_x+\left[\frac{GI}{R}\frac{\partial^2}{\partial x^2}-\frac{D}{R^3}\frac{\partial^2}{\partial\theta^2}+k_\theta^2\frac{G}{R}\left(h+\frac{I}{R^2}\right)-\frac{\rho I}{R}\frac{\partial^2}{\partial t^2}\right]v+$$

$$+\left[GI\frac{\partial^2}{\partial x^2}-\frac{D}{R^2}\frac{\partial^2}{\partial\theta^2}+k_\theta^2G\left(h+\frac{I}{R^2}\right)-\rho I\frac{\partial^2}{\partial t^2}\right]\varphi_\theta$$

$$+\left[-\frac{D}{R^3}-k_\theta^2\frac{G}{R}\left(h+\frac{I}{R^2}\right)\right]\frac{\partial w}{\partial\theta}=0, \tag{2.23d}$$

$$\left[-\frac{E_p\nu}{R}\frac{\partial}{\partial x}\right]u+\left[k_x^2Gh\frac{\partial}{\partial x}\right]\varphi_x+\left[-k_\theta^2\frac{G}{R^2}\left(h+\frac{I}{R^2}\right)-\left(\frac{E_p}{R^2}+\frac{D}{R^4}\right)\right]\frac{\partial v}{\partial\theta}+$$

$$\left[\frac{D}{R^3}+k_\theta^2\frac{G}{R}\left(h+\frac{I}{R^2}\right)\right]\frac{\partial\varphi_\theta}{\partial\theta}+$$

$$+\left[k_x^2Gh\frac{\partial^2}{\partial x^2}+k_\theta^2\frac{G}{R^2}\left(h+\frac{I}{R^2}\right)\frac{\partial^2}{\partial\theta^2}-\left(\frac{E_p}{R^2}+\frac{D}{R^4}\right)-\rho h\frac{\partial^2}{\partial t^2}\right]w=0. \tag{2.23e}$$

Considering solutions for wave propagation in the form:

$$\begin{aligned}
u(x,\theta,t) &= Ue^{i(\omega t-\alpha x)}\cos n\theta,\\
\varphi_x(x,\theta,t) &= \Psi e^{i(\omega t-\alpha x)}\cos n\theta,\\
v(x,\theta,t) &= Ve^{i(\omega t-\alpha x)}\cos n\theta,\\
\varphi_\theta(x,\theta,t) &= \Phi e^{i(\omega t-\alpha x)}\cos n\theta,\\
w(x,\theta,t) &= We^{i(\omega t-\alpha x)}\cos n\theta,
\end{aligned} \tag{2.24}$$

where :

n=0,1,2… is an integer indicating the number of waves traveling circumferentially , ω is the circular frequency and α is the wave number defined as:

$$\alpha = \frac{\omega}{c_p} = \frac{2\pi}{L}$$

Substituting Eq. 2.24 in the equations of motion, Eq. 2.23, a homogeneous system of linear equations is found in the form of the frequency-equation determinant:

$$\left|F\right| = 0 \tag{2.25}$$

Where the elements of the system are:

$$F_{1,1} = 4\pi^2\delta^2\left(s^2-2N\right) - m^2n^2\left(1+\frac{m^2}{12}\right)$$

$$F_{1,2} = \frac{1}{3}m\pi^2\delta^2\left(s^2-2N\right) + \frac{1}{12}m^3n^2$$

$$F_{1,3} = 2N\pi mn\delta\left(1+\nu\right)i$$

$$F_{1,4} = 0$$

$$F_{1,5} = 4N\pi\nu m\delta i$$

$$F_{2,1} = F_{1,2}$$

$$F_{2,2} = \frac{1}{3}\pi^2\delta^2\left(s^2-2N\right) + \frac{1}{12}m^2n^2 - k_x^{\,2}$$

$$F_{2,3} = 0$$

$$F_{2,4} = \frac{1}{6}\pi Nmn\delta\left(1+\nu\right)i$$

$$F_{2,5} = -2k_x^{\,2}\pi\delta\, i$$

$$F_{3,1} = F_{1,3}$$

$$F_{3,2} = 0$$

$$F_{3,3} = m^2\left(k_\theta{}^2 + 2Nn^2\right)\left(1 + \frac{m^2}{12}\right) - 4\pi^2\delta^2\left(s^2 - 1\right)$$

$$F_{3,4} = \frac{1}{3}m\pi^2\delta^2\left(s^2 - 1\right) - k_\theta{}^2 m\left(1 + \frac{m^2}{12}\right) - \frac{Nm^3n^2}{6}$$

$$F_{3,5} = m^2 n\left(1 + \frac{m^2}{12}\right)(k_\theta{}^2 + 2N)$$

$$F_{4,1} = 0$$

$$F_{4,2} = \frac{1}{6}\pi Nmn\delta(1+\nu)\,i$$

$$F_{4,3} = F_{3,4}$$

$$F_{4,4} = k_\theta{}^2\left(1 + \frac{m^2}{12}\right) + \frac{Nm^2n^2}{6} - \pi^2\delta^2\left(s^2 - 1\right)$$

$$F_{4,5} = -k_\theta{}^2 mn\left(1 + \frac{m^2}{12}\right) + \frac{Nm^3n}{6}$$

$$F_{5,1} = F_{1,5}$$

$$F_{5,2} = F_{2,5}$$

$$F_{5,3} = F_{3,5}$$

$$F_{5,4} = F_{4,5}$$

$$F_{5,5} = -4\pi^2\delta^2\left(s^2 - k_x{}^2\right) + m^2\left(1 + \frac{m^2}{12}\right)\left(k_\theta{}^2 n^2 + 2N\right) \tag{2.26}$$

The Characteristic Equation (2.25) is obtained by calculating the determinant of the frequency equations obtained from Eq. 2.23 and Eq. 2.24 where:

$$m=\frac{h}{R}, \qquad \mathrm{N}=\frac{1}{(1-\nu)}, \quad s=\frac{c_p}{c_t} \ \ \delta=\frac{h}{L};$$

and L; is the wavelength given by $L=\frac{2\pi}{\alpha}$, being $\alpha=\frac{\omega}{c_p}$; the wave number. Then, the phase velocity c_p is related to the natural frequency by $\omega=\frac{2\pi c_p}{L}$. There are thus five roots for s^2; and then five possible modes exist for each case. Also for axisymmetrical motion, assuming no waves propagating circumferentially, n = 0; and for flexural motion, assuming one wave propagating circumferentially n = 1. The determination of the thickness-shear adjustment coefficients, k_x and k_θ in axial and circumferential directions respectively is discussed in Mirsky and Herrmann[35]; and can be calculated for any material. Both coefficients are obtained as done by Mindlin[47] for flat plates, but in this case, in the axial and circumferential directions of the cylinder. The procedure to obtain those coefficients consisting of comparison of the cutoff frequencies, i.e. the frequencies for $\delta=0$, of the thickness shear modes to those of the so-called exact theory, which refers to the complete three-dimensional theory. Greenspon[48] made a detailed comparison of the exact theory with approximate theories. An hybrid method that is based in two theories: 1. Mirsky-Herrman theory and 2. Gazis' three dimensional theory is reported in a book by Armenakas, et al.[49]. The book summarizes a self-contained treatment of the problem of propagation of plane harmonic waves on circular cylinder, within the framework of the three-dimensional theory of elasticity as well as tables of frequencies of free vibration for cylinders, dispersion curves and mode shapes.

One of the abilities of M-H theory is that it can be applied to any hollow cylinder, thin ($m \le 1/10$), thick ($m \ge 7/10$) and anything between those values as considered by Mirsky and Herrmann[35,37,41]. Additionally, the Mirsky-Herrmann theory can include the special limit cases when m=0, and when m→∞. The first case corresponding to a flat plate, in which the theory reduces to the classical plate theory discussed by Mindlin[47]. The second limit case when m→∞, in which the theory reduces to that for vibrations in a solid cylindrical bar.

Results are presented for the axial phase velocity versus wave number for a number of situations, of which only two are shown: for a relatively thin-walled (m=1/30) cylindrical shell and for a relatively thick-walled (m=1/3) cylindrical shell. The phase velocity is non-dimensionalized by the transverse wave (shear) velocity c_t, while the wave number parameters is that defined by $\delta = \frac{h}{L}$. Poisson's ratio is $\nu = 0.3$ in all cases.

Three different classes of modes can be recognized in infinitely long pipes. The number of modes for a circular cylinder includes an infinite number of torsional modes, an infinite number of longitudinal modes, and a doubly infinite number of flexural modes. They are designated as follows

- longitudinal modes: (axisymmetric modes, n=0)
- torsional modes: (axisymmetric modes, n=0)
- flexural modes: (non-axisymmetric modes, n≥1)

At the dispersion plots, each curve corresponds to a specific mode S_j with mode number j=1,2,3,… and circumferential order n=1,2,3… for the flexural modes. The longitudinal and torsional modes for which n=0 are axisymmetric. For the other circumferential orders the displacements are no longer axisymmetric and the occurring modes are the non-axisymmetric flexural modes.

Note that the axisymmetric modes are characterized by a circumferential order of n=0 meaning that the motion is purely axisymmetric along the pipe and no circumferential wave motion exists.

In Fig. 2.9(a), the axisymmetric case or longitudinal-radial vibration *(n* = 0) is shown for a rather thin shell *(m=h/R* = 1/30*)*.

Each of the five resultant modes is associated with a particular kind of motion. The mode S_l is the lowest flexural mode. The non-dispersive S_2 mode is associated with purely torsional motion, known as lower torsional mode or first Lobar mode. S_3 corresponds to the second flexural mode, S4 is the second or higher torsional mode and S_5 is the third flexural mode.

A loss of information occurs from delta=0 to approx. 0.02. An amplified view in Fig. 2.9(b) shows the detail. I am attributing this loss to the lack of resolution for plotting with a two dimensional implicit plotting in Maple®[50] program. Another error inherent to the maple program for implicit plotting is that it does not detect discontinuities and then interpolates between the closer points. The reason could also be the lack of resolution when plotting closer lines (points).

The flexural motion *(n* = 1) is described by figure 2.10 for a relatively thick cylindrical shell *(m=h/R* = 1/3*)*. All of the modes, torsional and flexural, are now coupled.

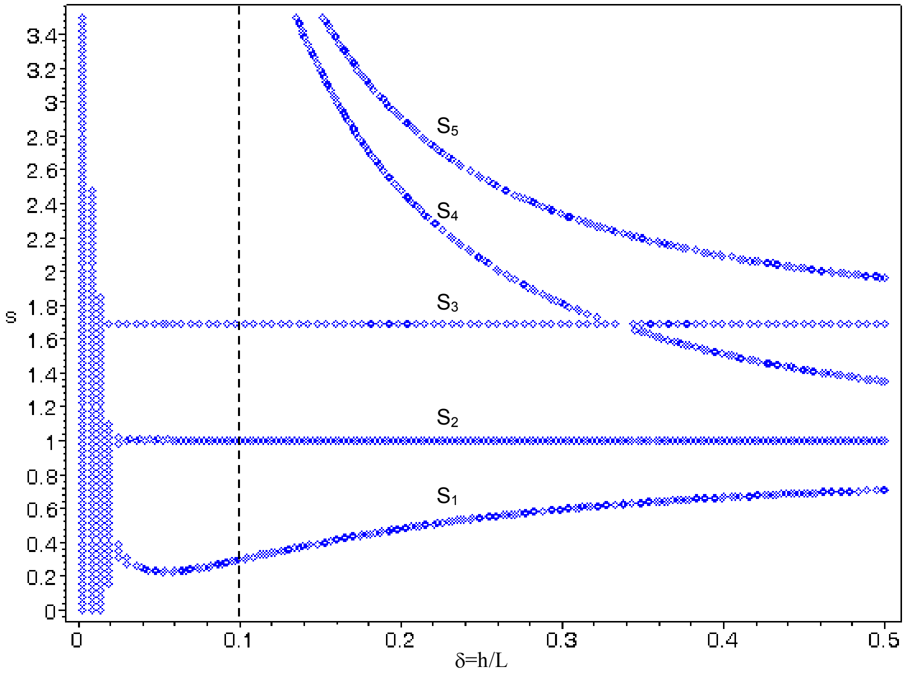

Fig. 2.9a Theoretical M-H dispersion curves for a thin cylindrical shell, m=h/R=1/30, ν=0.3, and n=0 (axisymmetric motion). S_1,S_2, S_3, S_4 and S_5 are the corresponding modes for each root of the frequency equation solution. The vertical line at 0.1 indicates the amplification zone at next figure.

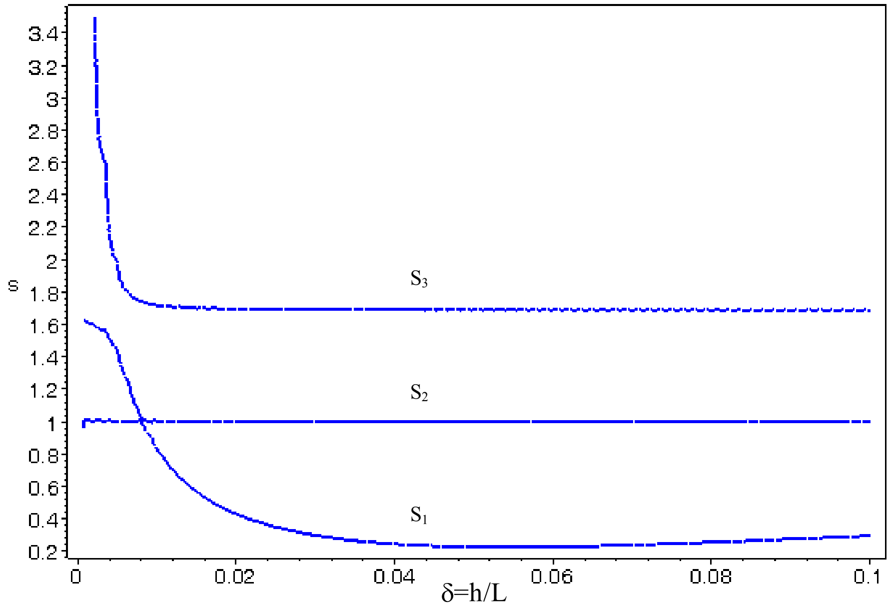

Fig. 2.9b--Theoretical M-H dispersion curves for a thin cylindrical shell, m=h/R=1/30, ν=0.3, and n=0 (axisymmetric motion). Amplified view from 2.9a showing the first three modes.S_1,S_2 and S_3.

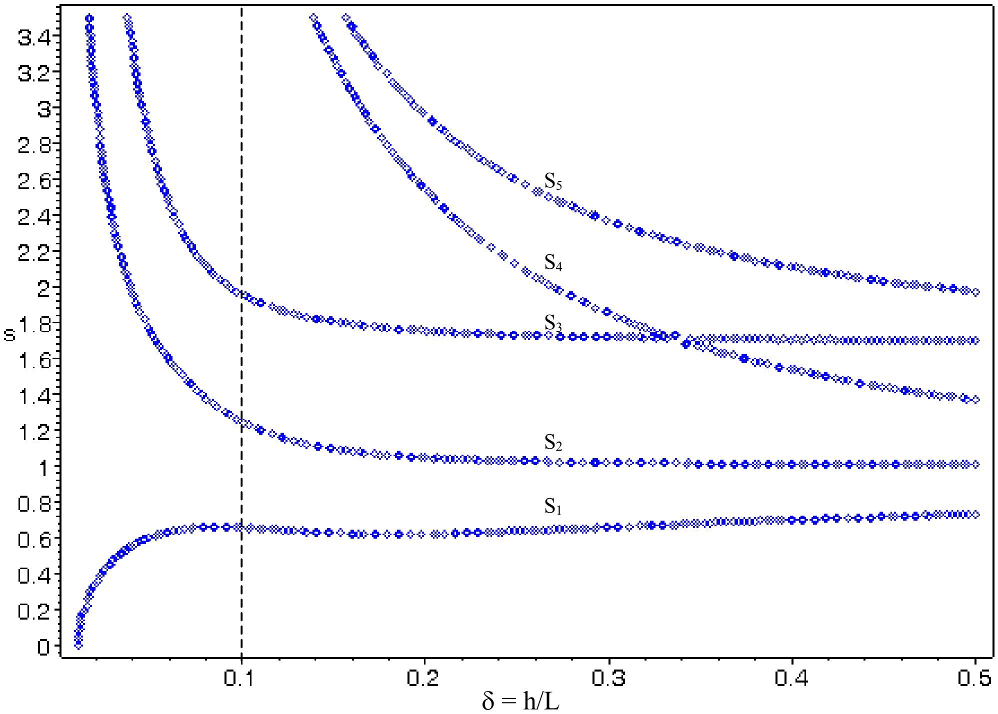

Fig. 2.10a-- Theoretical M-H dispersion curves for a thick cylindrical shell, m=h/R=1/3, ν=0.3, and n=1 (flexural motion). The vertical line at 0.1 indicates the amplification zone at next figure.

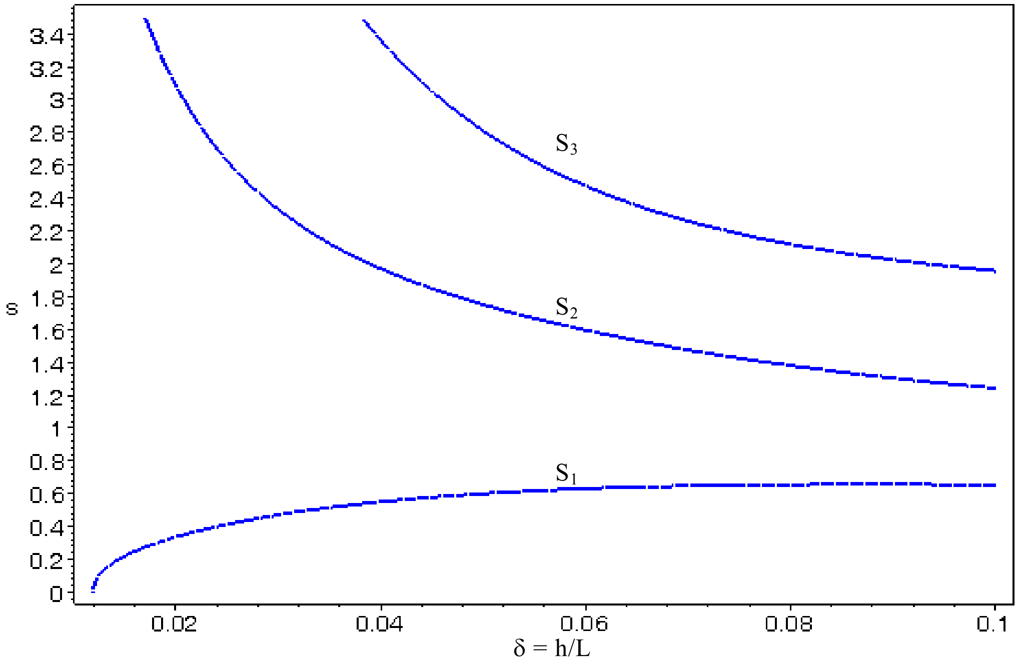

Fig. 2.10b-- Theoretical M-H dispersion curves for a thick cylindrical shell, m=h/R=1/3, ν=0.3, and n=1 (flexural motion). Amplified view from 2.10a showing the first three modes.S_1,S_2 and S_3.

According to Mirsky and Herrmann[35], the adjustment coefficient k_x is given by

$$k_x = \sqrt{\pi^2/12} = 0.9069 \tag{2.27}$$

A program for plotting these curves and the calculation of the second adjustment coefficient $k_\theta=0.9277$ for $\nu=0.3$, are included at Appendix C.

2.5 Transformation of Theoretical results from non-dimensional velocity (s) vs. non-dimensional wave number (δ) to time vs. frequency

The Original M-H Dispersion curves Fig. 2.9 and 2.10, are expressed in terms of non-dimensional velocity (s) vs. non-dimensional wave number (δ). As will be addressed later, the experimental dispersion curves are in terms of time vs. frequency at a single detection point. Then a transformation is needed for one of the parts. Because the experimental dispersion curves are obtained directly, it was chosen to make the transformation on the theoretical curves. The transformation consists of changes of variables before calculating the roots of the characteristic equation 2.25. Those changes are:

$$s = \frac{\omega h}{2\pi\delta}\sqrt{\frac{2\rho(1+\nu)}{E}} \qquad \text{and} \qquad \delta = \frac{\omega t h}{2\pi\ell} \tag{2.28}$$

with ℓ being the travel distance of the propagating wave from the excitation point to the detection point.

After the transformation, the dispersion curve is now in terms of time and frequency domains.

Figure 2.11a, shows the lower frequencies portion (0 to 200 KHz) of the transformed dispersion curves and the first three modes corresponding to the thin cylindrical shell (m=1/30), axisymmetric motion (n=0) of figure 2.9b. Figure 2.11b shows the higher frequencies (1 MHz to 3.5 MHz) portion of the transformed dispersion curves for this case (m=1/30, n=0), here the five modes corresponding to Fig. 2.9a are present.

In figure 2.12 it is presented the same thin cylindrical shell (m=1/30) but now, considering the flexural mode where the number of circumferential waves is one (n=1). Figure 2.12a shows the lower frequencies portion (0 to 200 kHz) of the transformed dispersion curves and the first three modes corresponding to the thin cylindrical shell (m=1/30), flexural mode (n=1). Figure 2.12b shows the higher frequencies (1 MHz to 3.5 MHz) portion of the transformed dispersion curves for this case (m=1/30, n=1), here the five modes are uncoupled. Note that apparently modes S_3 and S_4 are coupled, However when looking into the amplified view, it is noticed that those modes are really uncoupled, and that apparent coupling is known as “weak coupling”. The amplified view in figure 2.12b shows the weak coupling between modes S_3 and S_4.

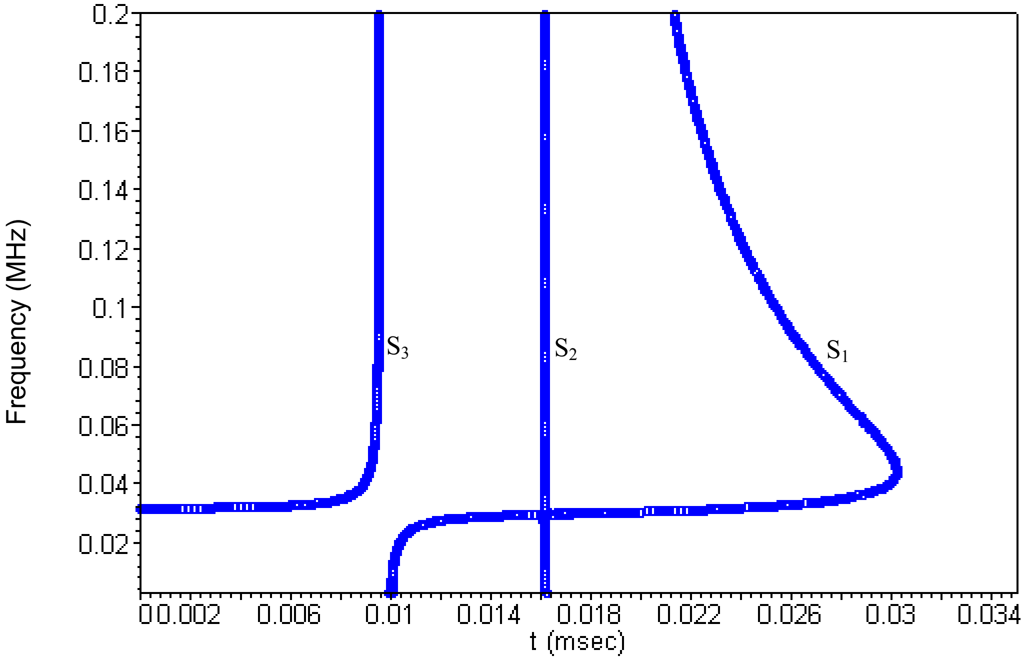

Fig. 2.11a-- Transformed M-H dispersion plot into time vs. frequency, thin cylindrical shell, m=1/30, axisymmetric mode, n=0. Lower frequencies. S_1=first (lowest) flexural mode, S_2=first (lowest) torsional mode, S_3= second flexural mode.

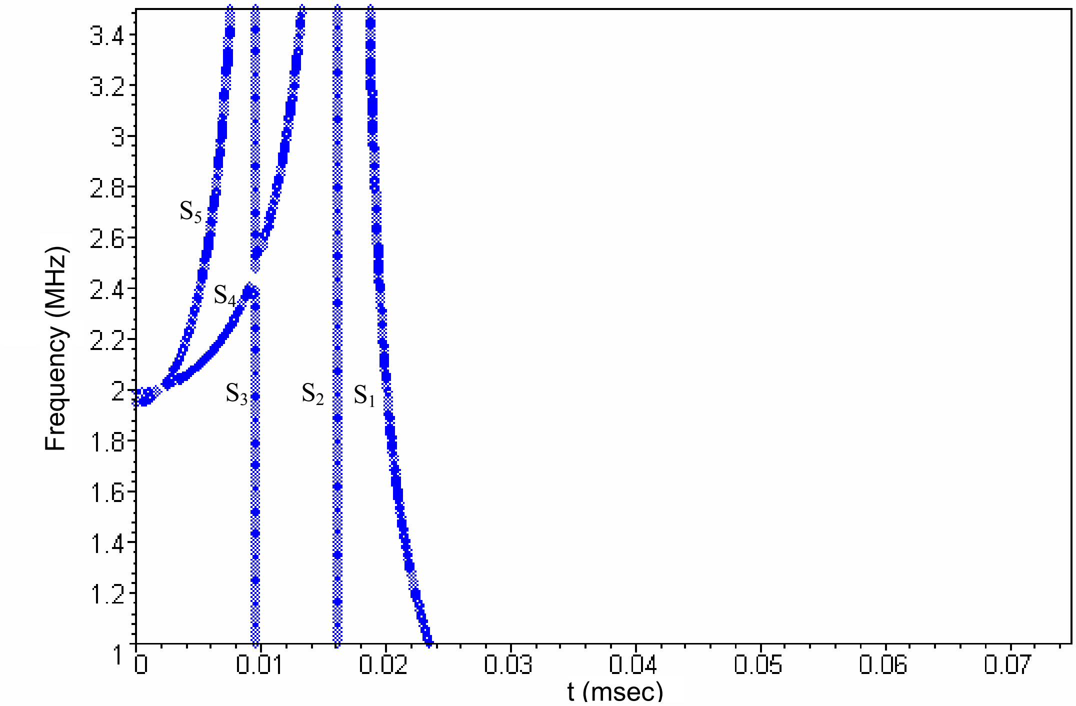

Fig. 2.11b-- Transformed M-H dispersion plot into time vs. frequency, thin cylindrical shell, m=1/30, axisymmetric mode, n=0. Higher frequencies. S_1=first (lowest) flexural mode, S_2=first (lowest) torsional mode, S_3= second flexural mode, S_4=higher torsional mode, S_5= third flexural mode.

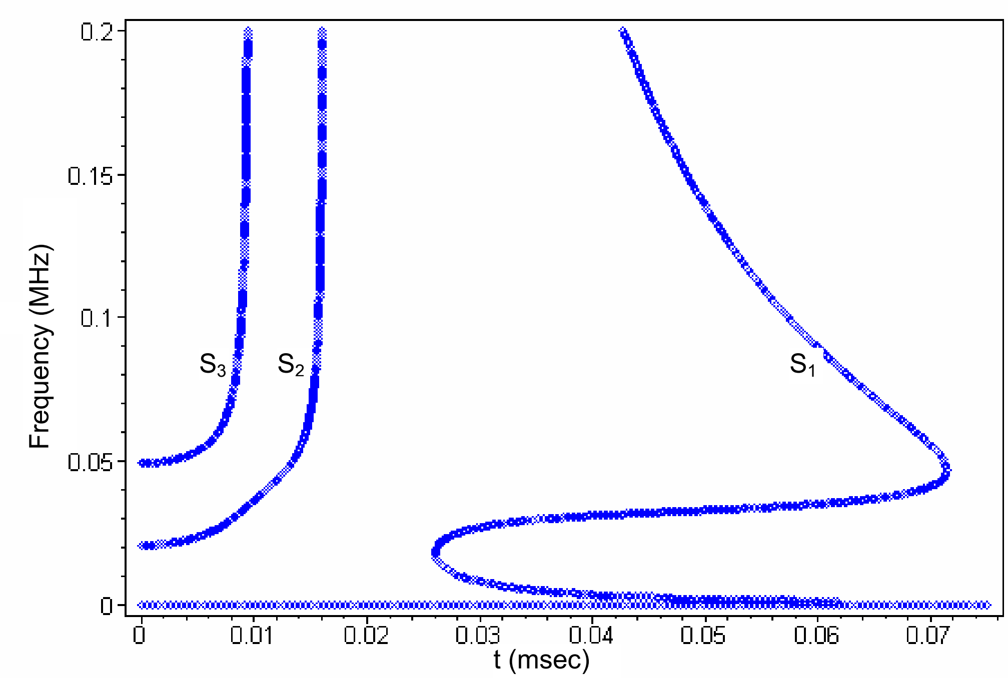

Fig. 2.12a-- Transformed M-H dispersion plot into time vs. frequency. Thin cylindrical shell, m=1/30, Flexural mode, n=1. Lower frequencies. S_1=first (lowest) flexural mode, S_2=first (lowest) torsional mode, S_3= second flexural mode.

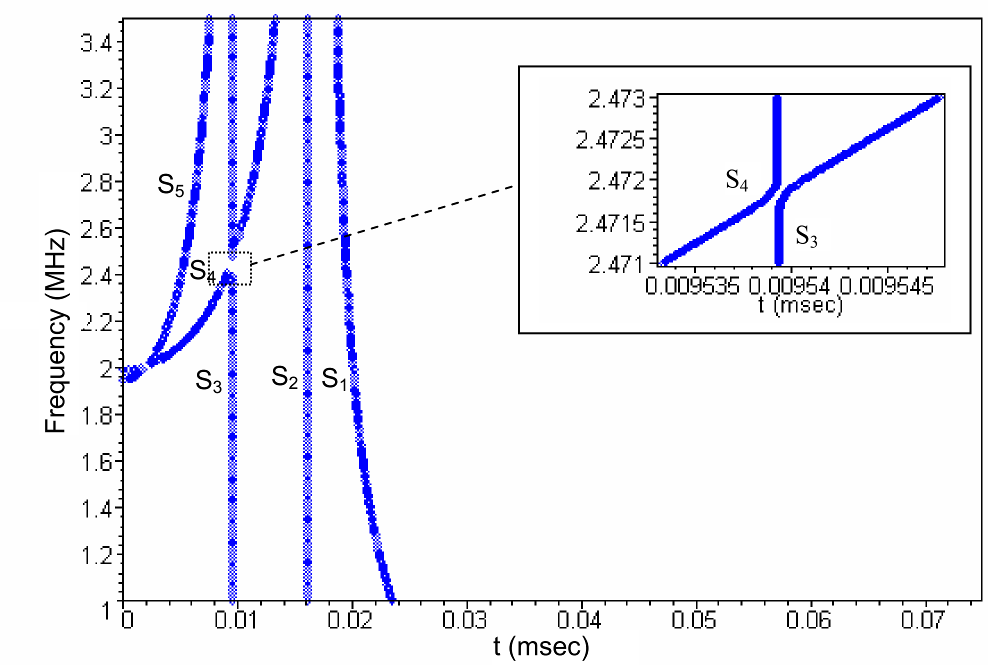

Fig. 2.12b---Transformed M-H dispersion plot into time vs. frequency. Thin cylindrical shell, m=1/30, flexural mode, n=1. Higher frequencies. S_1=first (lowest) flexural mode, S_2=first (lowest) torsional mode, S_3= second flexural mode, S_4=higher torsional mode, S_5= third flexural mode. The amplified view shows the “weak coupling” between modes S_3 and S_4.

Figure 2.13 shows the full range of frequencies, from 0 to 3.5MHz, of the Transformed Mirsky-Herrmann dispersion curves for a thick cylindrical shell (m=1/3) , and axisymmetric case (n=0). Note that as in the case for thin shell, there is one nondispersive mode corresponding to the second root of the solution of the frequency equation, S_2. Which is characteristic of the axisymmetric mode n=0. Figure 2.14 shows the transformed Mirsky-Herrmann dispersion curves, for the same thick cylinder (m=1/3) but now for the flexural case (n=1), corresponding to the original M-H dispersion curves from figure 2.10a. Note in this case that now all the modes are coupled as in the case for thin cylindrical shell. On figure 2.14a it is shown the full range of frequencies, from 0 to 3.5MHz and apparently there is coupling between modes S_3 and S_4, however when seeing this into an amplification, as in figure 2.14b, it is clear that those modes are uncoupled and they show a typical "weak coupling" behavior.

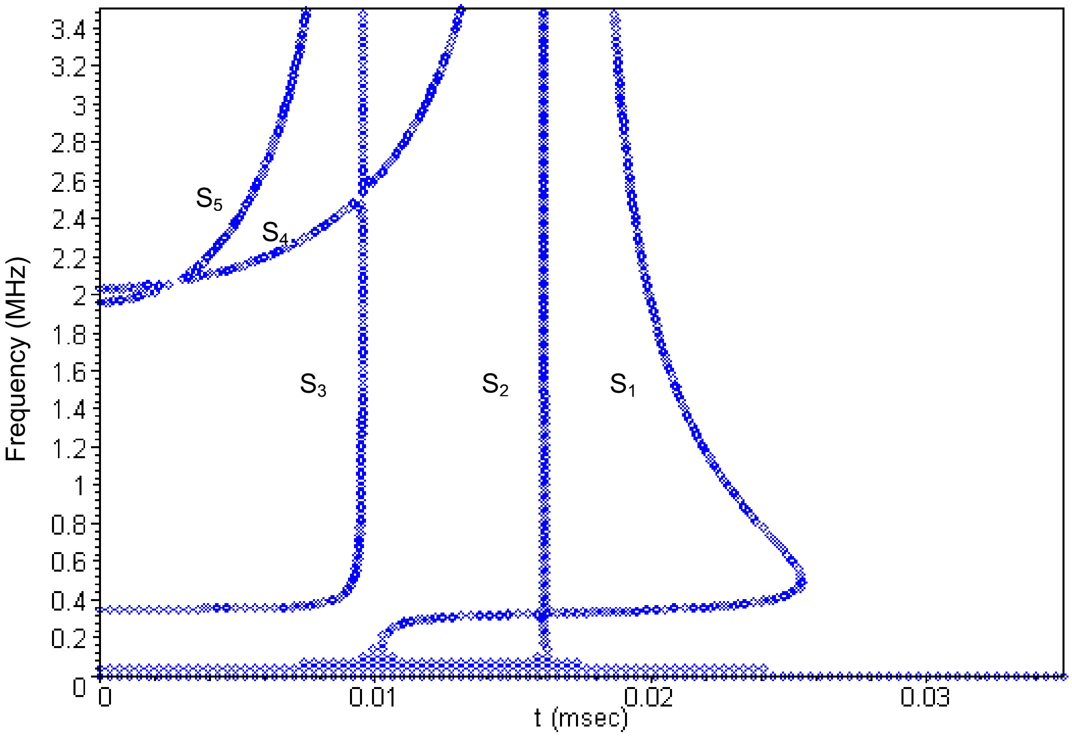

Fig. 2.13-- Transformed M-H dispersion plot into time vs. frequency. Thick cylindrical shell, m=1/3, axisymmetric mode, n=0. S_1=first (lowest) flexural mode, S_2=first (lowest, nondispersive) torsional mode, S_3= second flexural mode, , S_4=higher torsional mode, S_5= third flexural mode.

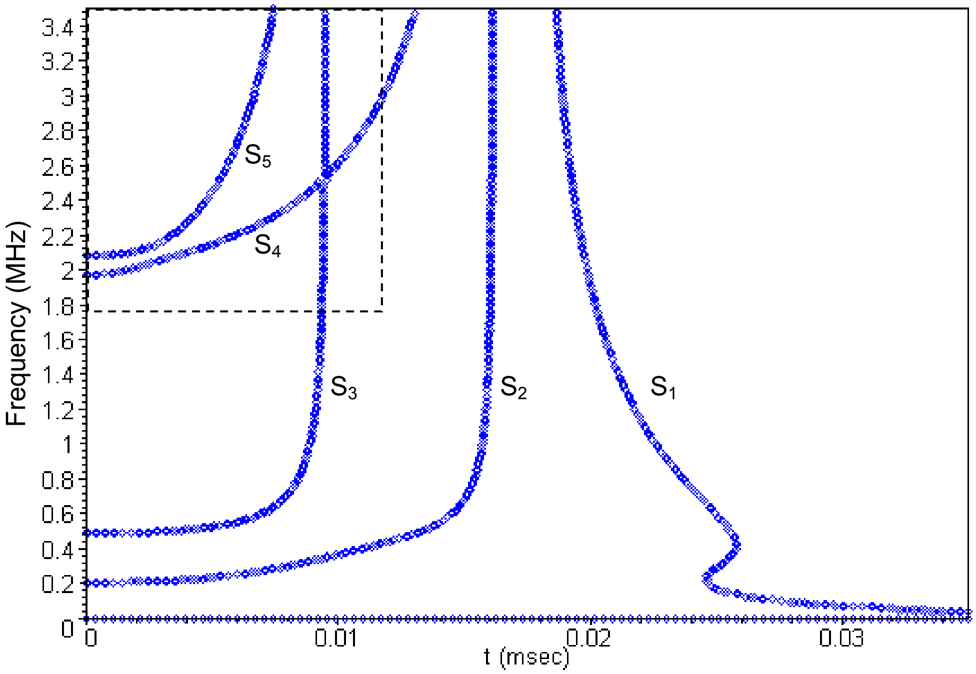

Fig. 2.14a-- Transformed M-H dispersion plot into time vs. frequency. Thick cylindrical shell, m=1/3, n=1. S_1=first (lowest) flexural mode, S_2=first (lowest) torsional mode, S_3= second flexural mode, S_4=higher torsional mode, S_5= third flexural mode. The rectangle on the upper left shows the area to be amplified in next figure.

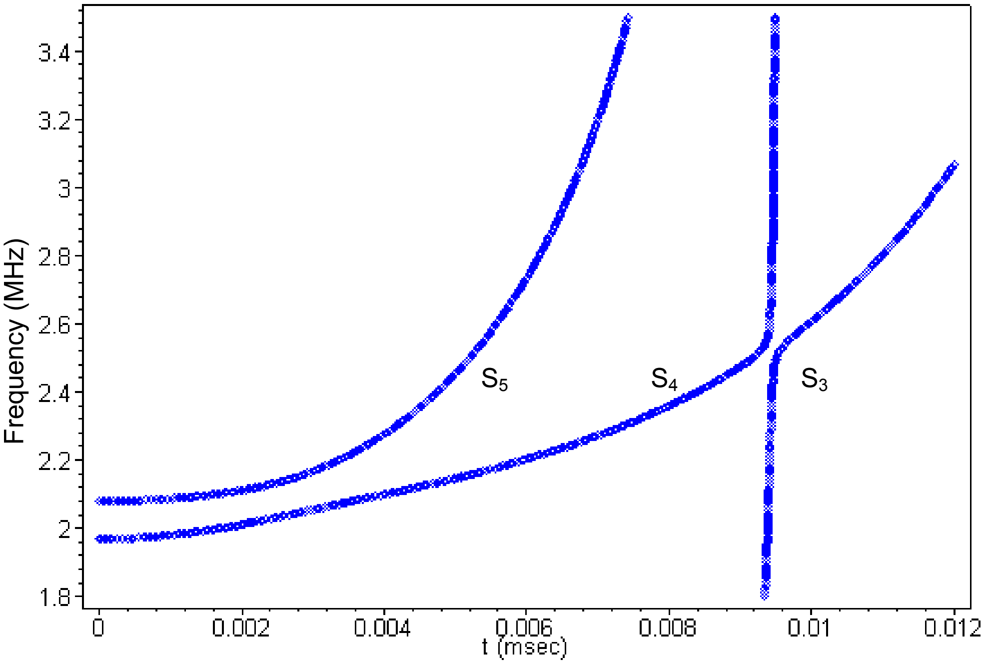

Fig. 2.14b—Amplified view of previous figure showing the uncoupling (weak coupling) of modes S_3 and S_4.

CHAPTER III

WAVELET ANALYSIS

3.1 Introduction

The analysis of data in this research, was performed with the wavelet analysis. This method uses localized waveforms rather than infinite sinusoids, and for this application it is more efficient. Wavelet analysis has been proved to be advantageous over other methods[51] for time-frequency analysis of signals obtained from wave propagation phenomena in structures[19]. In addition, the use of wavelet analysis technique can be useful for the enhancement of signal-to-noise ratio, as studied by Chen, et al. [52]. Other uses of the Wavelet Transform include analysis of transient vibrations[53], analysis of Moiré patterns[54], and image and sound compression and transmission[55]. Like sines and cosines in Fourier analysis, e.g. Ramirez[56], wavelets are used as basis functions to represent other functions, this comparison is depicted in figure 3.1. Here the signal, originally in time domain is transformed first into the frequency domain by using a series of sines or cosines of different frequencies. Thus, Fourier basis functions are localized in frequency but not in time. Small frequency changes in the Fourier transform will produce changes all over in the time domain. On the other hand, Wavelets are local in both frequency (via dilations) and in time (via translations) as shown in figure 3.1(b). The Wavelet Analysis is a multiresolution technique; which as implied by its name, analyzes the signal at different frequencies with multiple resolutions through wavelets of different scales and positions. Not every spectral component is resolved equally, as for example, in the Short Time Fourier Transform STFT, introduced by Gabor[57] where the exact time-frequency representation of a signal cannot be known. What can be known are the time intervals in which certain band of frequencies exists, which is a resolution problem. This is directly related to the width of the window function that is used within the STFT. If a window of infinite length is used, the FT is obtained, which gives perfect frequency resolution, but no time information. On the other hand, the narrower the window (short enough for the portion of the signal to be considered stationary, that is not time dependent), the better the time resolution, and the better the assumption of stationarity but frequency resolution is poor.

Fourier analysis has a serious drawback. In transforming to the frequency domain, time information is lost. When looking at a Fourier transform of a signal, it is impossible to tell when a particular event took place. If a signal doesn't change much over time, that is, if it is what is called a stationary signal this drawback isn't very important. However, most interesting signals contain numerous non-stationary or transitory characteristics: drift, trends, abrupt changes, and beginnings and ends of events. Since these characteristics are often the most significant part of the signal, detecting them is very important.

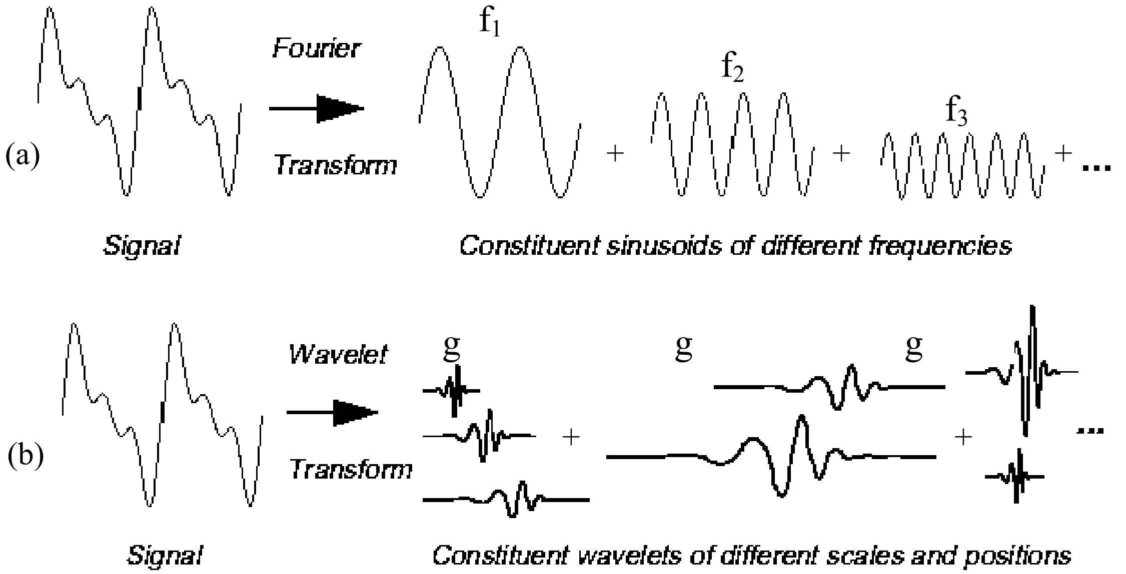

Fig. 3.1—Basic differences between Fourier basis (a) and wavelet basis (b).

The Short-Time Fourier Transform (STFT), maps a signal into a two-dimensional function of time and frequency by analyzing only a small section of the signal at a time, a technique called windowing the signal. The STFT represents a sort of compromise between the time- and frequency-based views of a signal. It provides some information about both when and at what frequencies a signal event occurs. However, this information can be obtained with limited precision, and that precision is determined by the size of the window. While the STFT's compromise between time and frequency information can be useful, as shown by Shin and Song[58]. The drawback is that once you choose a particular size for the time window, that window is the same for all frequencies. Many signals require a more flexible approach, one where we can vary the window size to determine more accurately either time or frequency.

In order to demonstrate the usefulness the Wavelet-based analysis in contrast to the Fourier-based analysis, lets consider two completely different signals with same frequency contents as shown in figure 3.2. The signal shown in figure 3.2(a) is constituted by three frequencies, 50KHz, 100KHz and 150KHz, in a time-span of 300μs, whereas figure 3.2(b) is a signal with three intervals: a frequency of 50 KHz from 0-100μs, a frequency of 100 KHz from 100-200 μs, and a frequency of 150 KHz from 200-300μs. When the signals are analyzed by Fourier Transform, as it can be seen on figure 3.3, both signals, fig.3.2(a) and fig. 3.2(b) produce the same information, because they have the same frequency content, however time information is unknown and it is not possible locate in time each of those frequencies. This is critical for signals, which are non-stationary (change with time), because Fourier transform will not reveal time information. When the two signals considered in this example are processed through the Wavelet transform, as it is shown on figures 3.4 and 3.5, now it is possible to locate the signal into a frequency-time map, whose third dimension is the relative magnitude of the wavelet coefficients. Fig. 3.4 shows the Wavelet transform that corresponds to the signal from figure 3.2(a), with a sum of three frequencies: 50KHz, 100KHz and 150KHz . Figure 3.5 shows the Wavelet transform that corresponds to the signal from figure 3.2(b) with 50KHz from 0 to 100μs, 100KHz from 100 to 200μs and 150KHz from 200 to 300μs. As it can be observed, both time-frequency maps are different and represent in a more precise way the two signals from figure 3.2.

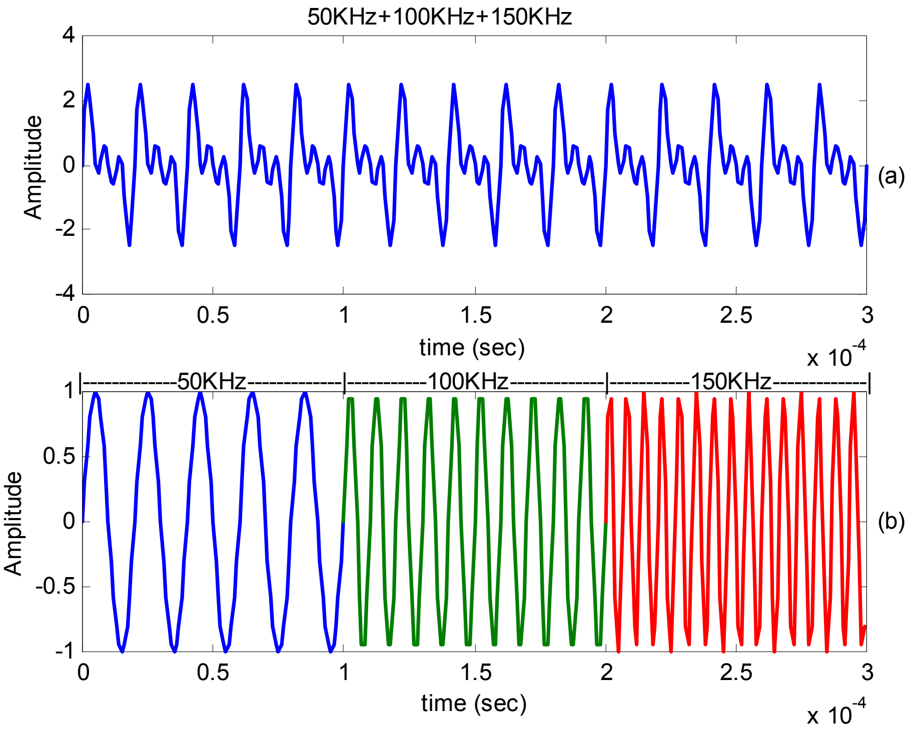

Fig.3.2--- Two different signals with same frequency contents, a) Signal with a sum of three frequencies: 50KHz, 100KHz and 150KHz. b) Signal with 50KHz from 0 to 100μs (blue), 100KHz from 100 to 200μs (green) and 150KHz from 200 to 300μs (red).

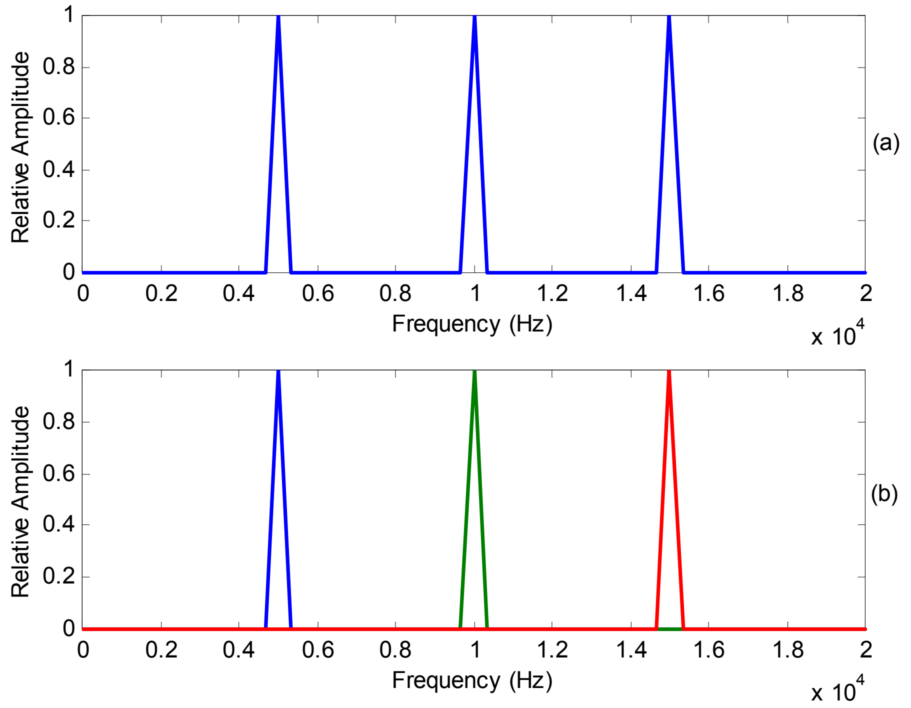

Fig.3.3--- Corresponding Fourier transforms of the two different signals with same frequency contents, (a) FFT of signal from fig.3.2(a) and (b) FFT of signal from figure 3.2(b).

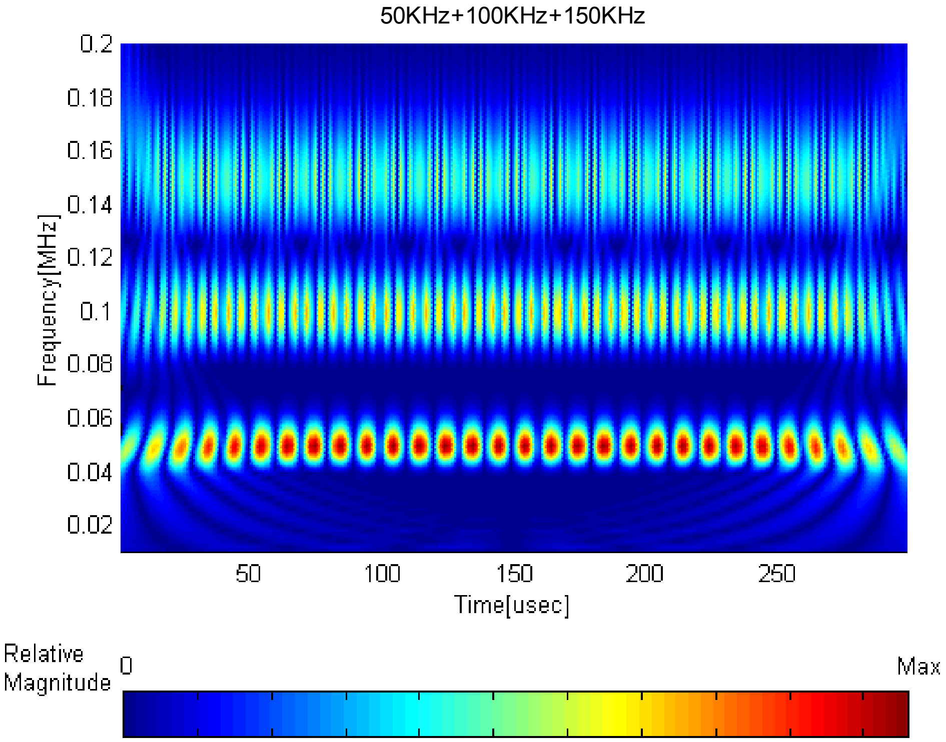

Fig.3.4--- Corresponding wavelet transform of signal from figure 3.2(a), with a sum of three frequencies: 50KHz, 100KHz and 150KHz. The third dimension is the relative magnitude going from zero in dark blue to a maximum in red.

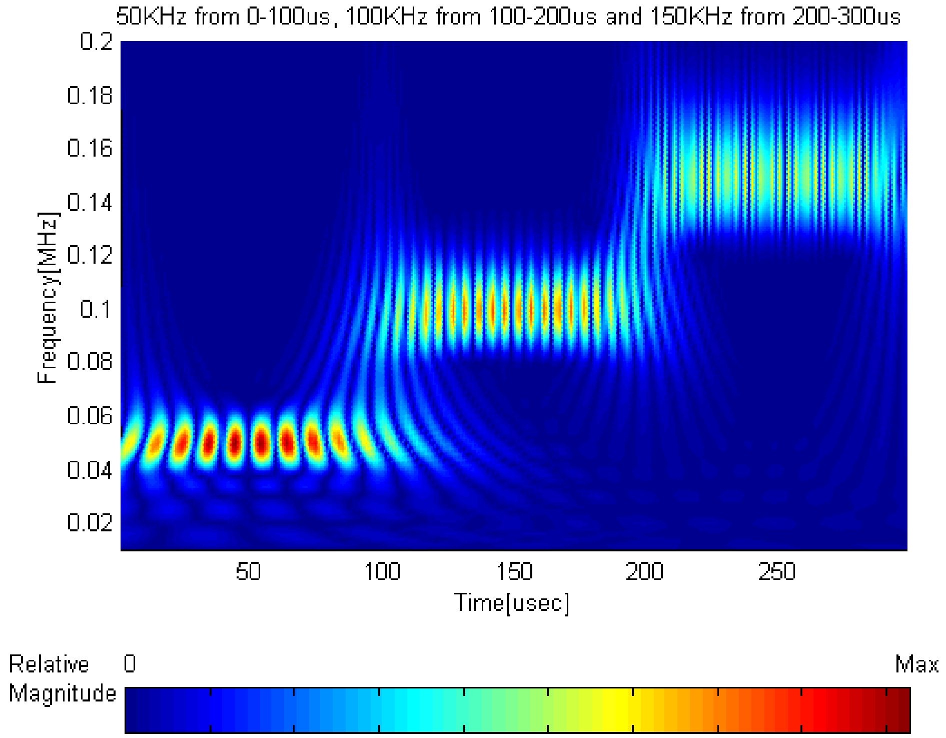

Fig.3.5--- Corresponding wavelet transform of signal from figure 3.2(b), with 50KHz from 0 to 100μs, 100KHz from 100 to 200μs and 150KHz from 200 to 300μs.

All the scale magnitudes of the plots of Wavelet transform considered in this dissertation are as shown in figures 3.4 and 3.5: the relative magnitude going from zero in dark blue to a maximum in red.

As we can see after the example, Wavelet transforms are very useful to process transient signals. Since thermoacoustic generated guided waves in cylinders are transient they are natural candidates for the Wavelet Transform.

3.2 Wavelet Transform

Wavelet analysis represents the next logical step: a windowing technique with variable-sized regions instead of a fixed window function. Wavelet analysis allows the use of long time intervals where we want more precise low frequency information, and shorter regions where we want high frequency information.

Figure 3.6 shows what this looks like in contrast with the time-based, 3.6(a), frequency-based, 3.6(b) and STFT, 3.6(c) views of a signal with respect to the wavelet basis, 3.6(d). Each of the blocks or cells on these graphs represent resolution in time or in frequency or in both domains.

The continuous wavelet transform (CWT) was developed as an alternative approach to the short time Fourier transform to overcome the resolution problem. The Wavelet analysis is done in a similar way to the STFT analysis, in the sense that the signal is multiplied with a function, known as the wavelet. This wavelet function is similar to the window function in the STFT, and the transform is computed separately for different segments of the time-domain signal.

However, there are two main differences between the STFT and the CWT:

1. The Fourier transforms of the windowed signals are not taken, and therefore a single peak will be seen corresponding to a sinusoid.
2. The width of the window is changed as the transform is computed for every single spectral component, which is probably the most significant characteristic of the wavelet transform.

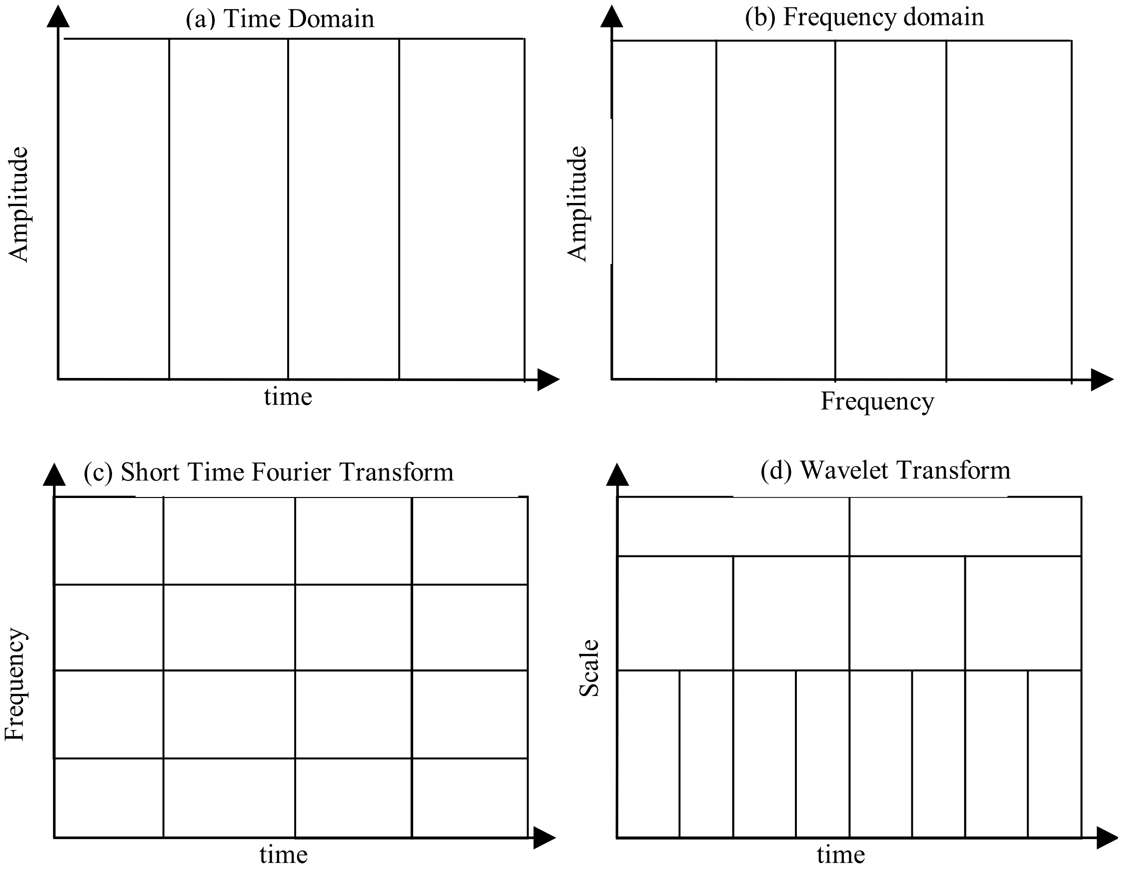

Fig. 3.6—Comparison of different basis for data analysis. (a) Time domain, the vertical bars represent time resolution; (b) Frequency domain, the vertical bars represent frequency resolution; (c) Short time Fourier transform, each of the cells represent a fixed area of time-frequency resolution; (d) Wavelet transform, here the scale is inverse-related to frequency and each of the cells represent a varying size of time-scale resolution, such that the higher scales represent lower frequencies and lower scales represent higher frequencies. The time resolution varies in such a form that the lower scales (higher frequencies) have better time resolution and higher scales (lower frequencies) have worst time resolution.

The continuous Wavelet transform is defined as follows[59]

$$\Psi(a,b) = \frac{1}{\sqrt{|a|}} \int x(t)\psi^{*}\left(\frac{t-b}{a}\right)dt \tag{3.1}$$

where:

a is the scale (defined as the inverse of the frequency) ,
b is the translation in time,
x(t) is the time-domain signal to be transformed,
ψ(t) is the analyzing function (or wavelet function), where * denotes the complex conjugate.

Even though the definition of the continuous Wavelet transform includes a complex conjugate, most wavelets are real valued.

It can be seen in the above equation that the transformed signal is a function of two variables, b and a, the translation and scale parameters, respectively. ψ(t) is the transforming function, and it is also called the mother wavelet .

The term mother wavelet gets its name due to two important properties of the wavelet analysis. The term wavelet means a small wave. This is because of the condition that this (window) function is of finite length (compactly supported).Once the wavelet function is chosen, one can make a basis of translations and dilatations of the mother wavelet. The term mother implies that the functions with different regions of support that are used in the transformation process are derived from one main function, or the mother wavelet. In other words, the mother wavelet is a prototype for generating the other window functions. Thus, the wavelets used in Wavelet transform are derived from the mother wavelet ψ(t) by dilation a and translation b.

In Figure 3.7 a mother wavelet corresponding to a centered (b=0) Gabor function is shown. The Gabor function is composed by a sinusoidal function evolved by a Gaussian.

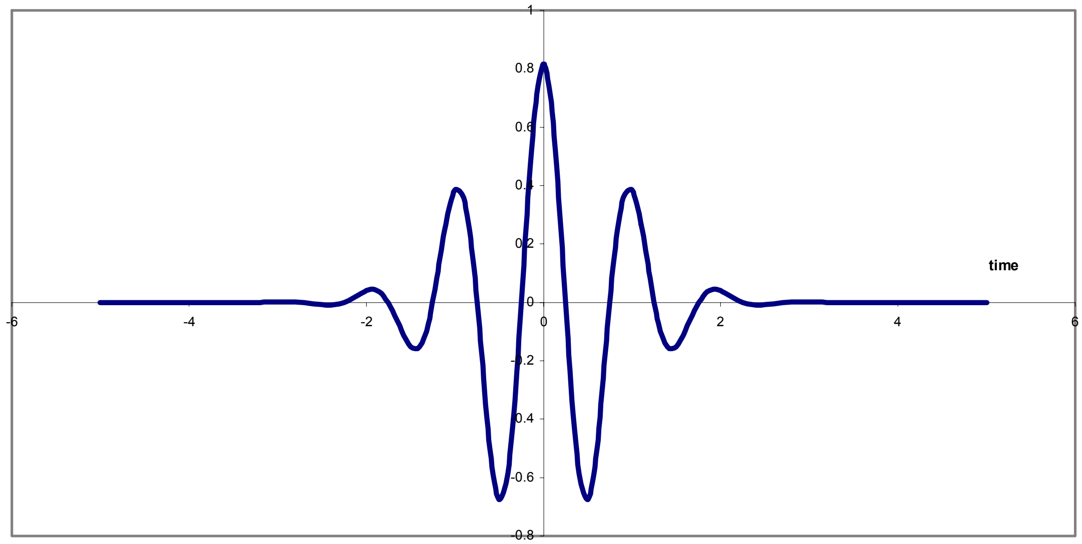

Fig. 3.7--Oscillatory Gabor function used for wavelet transformation, scale ɑ=1, translation b=0.

The term translation is used in the same sense as it was used in the STFT; it is related to the location of the window, as the window is shifted through the signal. Figure 3.8, shows the same wavelet from Fig. 3.7, but with a forward translation, that is, it is now affected by the translation parameter, in this case b=-1. This term corresponds to the time information in the transform domain. However, we do not have a frequency parameter, as we had before for the STFT. Instead, we have scale parameter that is defined as “frequency”. The term frequency is reserved for the STFT, however in Wavelet analysis, a more common term is used: scale. The parameter scale used in the Wavelet analysis is similar to the scale used in maps. As in the case of maps, high scales correspond to a non-detailed global view (of the signal), and low scales correspond to a detailed view. Similarly, in terms of frequency, low frequencies (high scales) correspond to a global information of a signal, usually spanning the entire signal. Whereas high frequencies (low scales) correspond to detailed information of a hidden pattern in the signal, usually lasting a relatively short time.

Scaling, as a mathematical operation, either dilates or compresses a signal. Larger scales correspond to dilated (or stretched out) signals, and small scales correspond to compressed signals.

In the definition of the wavelet transform, the scaling term is used in the denominator, and then scales $a > 1$ dilates the signal whereas scales $a<1$, compresses the signal. As it can be seen in figure 3.9, the particular scale parameter used ($a=1/2$) makes the wavelet compress.

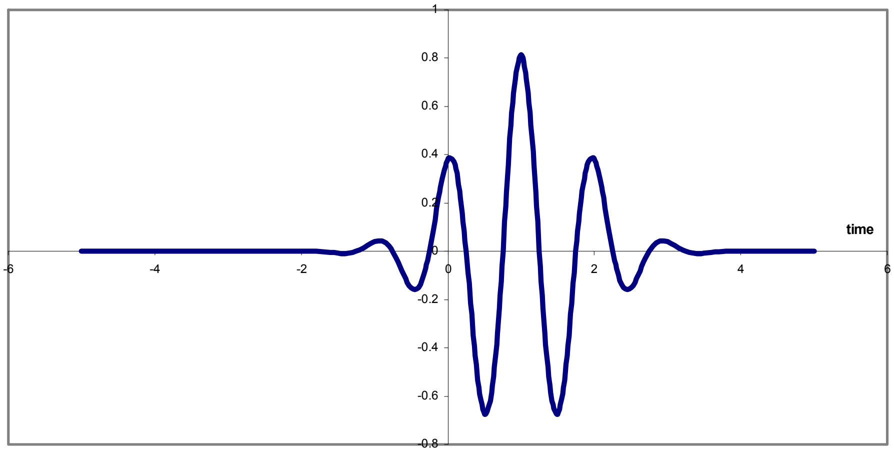

Fig. 3.8--Gabor function translated forward $\psi(t-1)$.

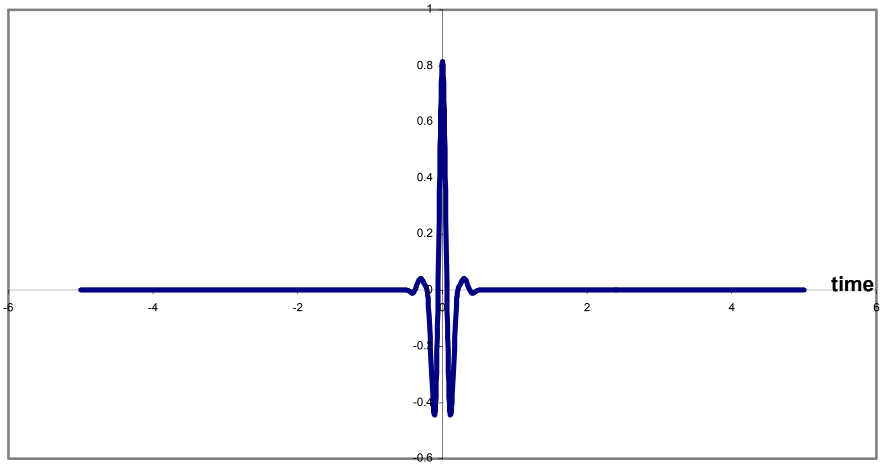

Fig. 3.9--Compressed Gabor function by scale $a=1/2$.

In the equation (3.1), let x(t) be the signal to be analyzed. The mother wavelet is chosen to serve as a prototype for all windows in the process. All the windows that are used are the dilated (or compressed) and shifted versions of the mother wavelet. Several functions are used as mother wavelet.

In order to qualify as a wavelet function, the mother wavelet must have certain characteristics[59]:

1) It has to be normalized

$$\|\psi\| = \left(\int_{-\infty}^{\infty} |\psi(t)|^2 \, dt \right)^{\frac{1}{2}} = 1, \tag{3.2}$$

2) Must have zero average

$$\int_{-\infty}^{\infty} \psi(t) dt = 0, \tag{3.3}$$

3) It must be admissible, i. e.

$$\int_{-\infty}^{\infty} \frac{|\Psi(\omega)|^2}{|\omega|} \, d\omega < \infty \tag{3.4}$$

where $\Psi(\omega)$ is the Fourier transform of the analyzing function $\psi(t)$ and ω is the angular frequency. It can be shown[60] that square integrable functions $\psi(t)$ satisfying the admissibility condition (3.4) can be used to first analyze and then reconstruct a signal without loss of information. The admissibility condition implies that the Fourier transform of $\psi(t)$ vanishes at the zero frequency, i. e.

$$\left. |\psi|^2 \right|_{\omega=0} = 0 \tag{3.5}$$

A considerable number of functions fulfill these conditions. This research work is not intended to be an explanatory text of wavelets and thus, only some of them will be mentioned here: Mexican hat function, Morlet wavelet, and Gabor function.

The Mexican Hat wavelet is defined as the second derivative of the Gaussian function, which is[61]:

$$\psi(t) = \frac{2\pi^{-1/4}}{\sqrt{3}}\left(e^{\frac{-t^2}{2}} \cdot \left(1-t^2\right)\right) \tag{3.6}$$

The Morlet wavelet is defined as[61]:

$$\psi(t) = C(\cos 5t) \cdot e^{\frac{-t^2}{2}} \tag{3.7}$$

And the Gabor Wavelet

$$\psi(t) = \frac{1}{\sqrt[4]{\pi}}\sqrt{\frac{\omega_0}{\gamma}}\, e^{-\frac{\left(\frac{\omega_0}{\gamma}\right)^2}{2}t^2 + i\omega_0 t} \tag{3.8}$$

where:

$\psi(t)$ is the wavelet function,

t is time

C is a constant used for normalization in view of reconstruction.

γ is the number of oscillations in the Gabor wavelet, which controls the sharpness of the Gaussian envelope in the time domain.

The function $\psi(t)$ is also the analyzing wavelet and satisfies the admissibility condition (3.4).

Once the mother wavelet is chosen, the computation starts with a scale $a=1$ and the process will continue starting from high frequencies and proceed towards low frequencies, in other words, for the increasing values of a. The wavelet at scale $a=1$ is then shifted towards the right by the amount b to the location $t=b$, and the above equation is computed to get the transformation value at $t=b$, $a=1$ in the time-frequency plane. The procedure is repeated until the wavelet reaches the end of the signal. One row of points on the time-scale plane for the scale $a=1$ is completed. Both parameters a and b must be increased by a sufficiently small step size. The procedure is repeated for every value of a. When the process is completed for all desired values of a, the CWT of the signal has been calculated.

Note that the lowest scale value must correspond to the highest frequency. It should be as narrow as the highest frequency component that exists in the signal, which is determined inherently by the Wavelet transform.

If the signal has a spectral component that corresponds to the current value of a, the product of the wavelet with the signal at the location where this spectral component exists gives a relatively large value. If contrarily the spectral component that corresponds to the current value of a is not present in the signal, the product value will be relatively small or zero.

When the CWT is plotted, the axes are normalized, the translation axis corresponds to time and the scale axis corresponds to frequency (the numbers on the translation and scale axis are just the number of samples in the computation).

3.3 Gabor Wavelet

In our case we use the Gabor Wavelet, Eq. (3.8) because it provides a smaller area of time-frequency window than any other functions, this also represents a better time-frequency resolution, in other words, the Gaussian window has the minimum time-bandwidth product determined by the uncertainty principle[62].

A direct approach for the analysis of dispersive waves using the Gabor Wavelet is used in this work and summarized below.

The analyzing wavelet is chosen such that $\psi(t)$ satisfy normalization (3.2) and zero mean condition (3.3) and its Fourier transform $\hat{\psi}(\omega)$ the admissibility condition (3.4) respectively. Then the analyzing wavelet may be considered as a window function both in the time and frequency domain. Let us assume that the time window $\psi(t)$ is centered at t = 0 and the frequency window $\hat{\psi}(\omega)$ at $\omega=\omega_0$. The function $\psi\left(\frac{t-b}{a}\right)$ is then localized around t = b and its Fourier transform [$ae^{(ib\omega)}\hat{\psi}(a\omega)$] around $\omega = \omega_0/a$. It is understood from Eq. (3.1) that the Wavelet transform $\Psi(a, b)$ corresponds to the time-frequency component of f(t) in the vicinity of t = b and $\omega = \omega_0/a$. If the parameters a and b are changed independently, the distribution of each time-frequency component is obtained on the b-a-plane, that is, on the time-frequency plane. Thus the Wavelet transform enables the time-frequency analysis.

According to the sampling theorem, a sufficiently wide time window is required to appropriately characterize low frequency signals. Conversely, to successfully detect the position of high frequency components on the time axis, a sufficiently narrow time window is required. The Wavelet transform automatically satisfies these requirements since the width of the time window $\psi\left(\frac{t-b}{a}\right)$ is proportional to the parameter a, that is, inversely proportional to the frequency. This character of the wavelet transform is beneficial to the analysis of structural waves usually composed of a wide range of frequency components.

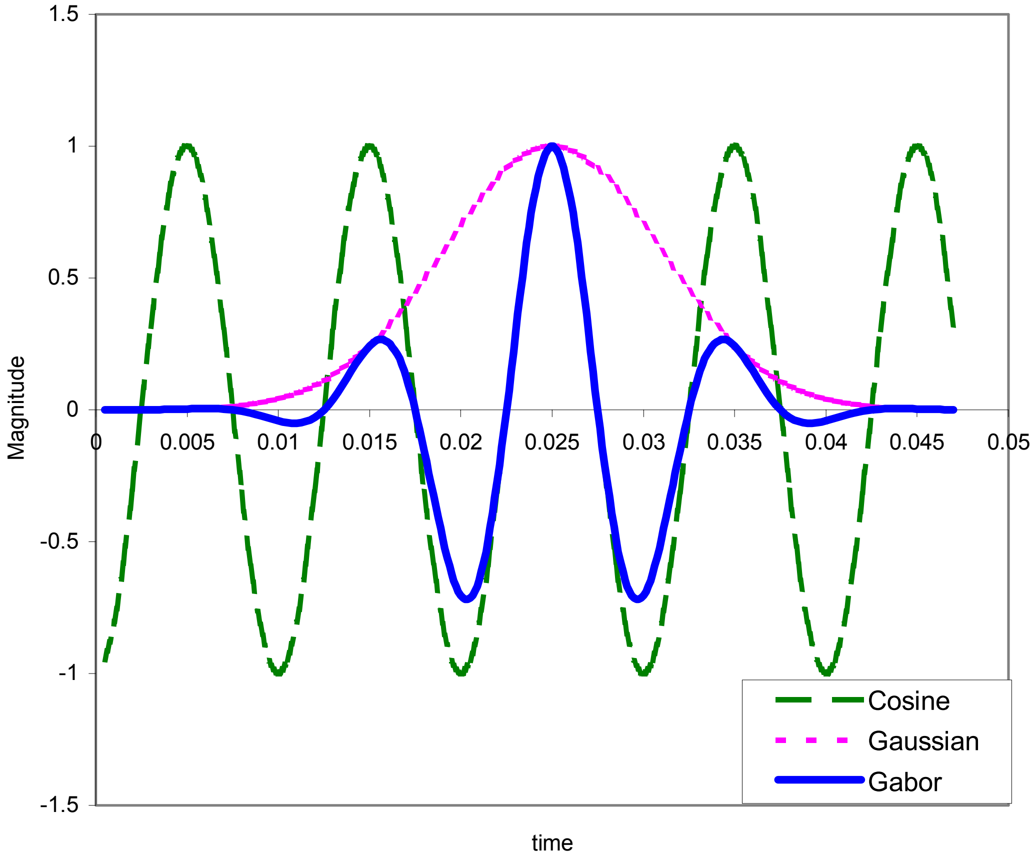

Figure 3.10—Components of the Gabor wavelet function.

In the Gabor function as expressed in Eq.(3.8), ω_0 and γ are positive constants. The Gabor function is shown in Fig. 3.10 is a complex-valued sinusoidal function windowed by a Gaussian function centered at the origin. Its Fourier transform is a Gaussian function centered at $\omega = \omega_0$. Although the Gabor function approximately satisfies the zero mean condition (3.3) if γ is sufficiently large. For the case being analyzed the constant gamma is set $\gamma = \pi\sqrt{2/\ln 2} \approx 5.336$ and $\omega_0 = 2\pi$ such that the value of a is equal to the period of vibration in order to have a time-Frequency relation (spectrogram) instead of a time-scale relation (scalogram). In addition, the wavelet transform using the Gabor wavelet is equivalent to the Fourier transform with a Gaussian window. Therefore, the squared magnitude of the Wavelet transform using the Gabor wavelet corresponds to the energy spectrum.

Then, the Wavelet analysis of laser-generated waves is similar to Fast Fourier Transform and conventional spectral analysis in the sense that frequency information is obtained.

On the other hand, it is more powerful because it maps the waveform, which is a one-dimensional time information into two-dimensional function of time and frequency.

The peaks of the time-frequency distribution indicate the arrival times of waves. Thus, by using the wavelet transform method, once the distance between laser source point and detection point is known, the group velocity dispersion can be obtained by analyzing the wave disturbance from one location. Then by using Wavelet transform, only one point is necessary for data extraction.

In the spectral analysis technique, it is necessary, however, to have at least two detection points in order to map time domain Vs. frequency.

Phase analysis is used to get Phase velocity dispersion Eq. (1.1) of surface wave while the wavelet transform method is employed to accurately identify the group velocity dispersion , Eq. (1.2), for a wide range of frequencies. In our case we use the Gabor Wavelet because it provides a smaller area of time-frequency window than any other functions. This also represents a better time-frequency resolution[61] according to the uncertainty principle, which establishes that it is not possible to locate precisely both time and frequency.

In general, wavelet analysis does not use a time-frequency region or spectrogram , but rather a time-scale region or scalogram. However, by using specific scaling constant as in the Gabor Wavelet it is possible to have a frequency-time domain. This is another important advantage of using Gabor wavelet as the analyzing function.

Between other advantageous characteristics of wavelets, one, which is very useful in this research, is the fact that noisy signals can be treated easily by using wavelet transform without affecting the useful information contained in the signal. This will be detailed later in Chapter V.

3.4 Algorithm for Gabor Wavelet Transform

Figure 3.11 shows the flow diagram of the algorithm used for programming the Gabor Wavelet Transform. Note that this algorithm is for a general Wavelet Transform and may be used for any analyzing function. In this case the analyzing function ψ corresponds to the Gabor function. The algorithm starts with initialization of variables, following readout of data pairs (t,x), which can be obtained from experimentation through a data acquisition system. Sampling rate and maximum frequency are calculated, then the user is required to input the number of divisions for the time domain and the frequency domain which are used to calculate time window (translation) and frequency (scale) which are then used for the main process at the double loop where data are processed for time and frequency at the Gabor Wavelet. As implied by equation (3.1), t is replaced by $(t-b)/a$. Once the matrix of Gabor Wavelet coefficients is obtained, the real part of the magnitude (absolute value) is plotted against time and frequency, ending up into a three dimensional representation as in figures 3.4 and 3.5 of section 3.1.

A Matlab®[63] program for Gabor Wavelet Analysis was developed to use in this research. It is listed in Appendix D. Between other characteristics, the program can analyze single or dual data sets, that is, it can be used for a one or a two channel Fiber Tip Interferometer (FTI) set-up, as explained later in Chapter IV. Other functions implemented in the program are, Discrete Fourier Transform (DFT) and Dispersion Spectrum. In addition, it has the option of de-noising of waveforms by using wavelets.

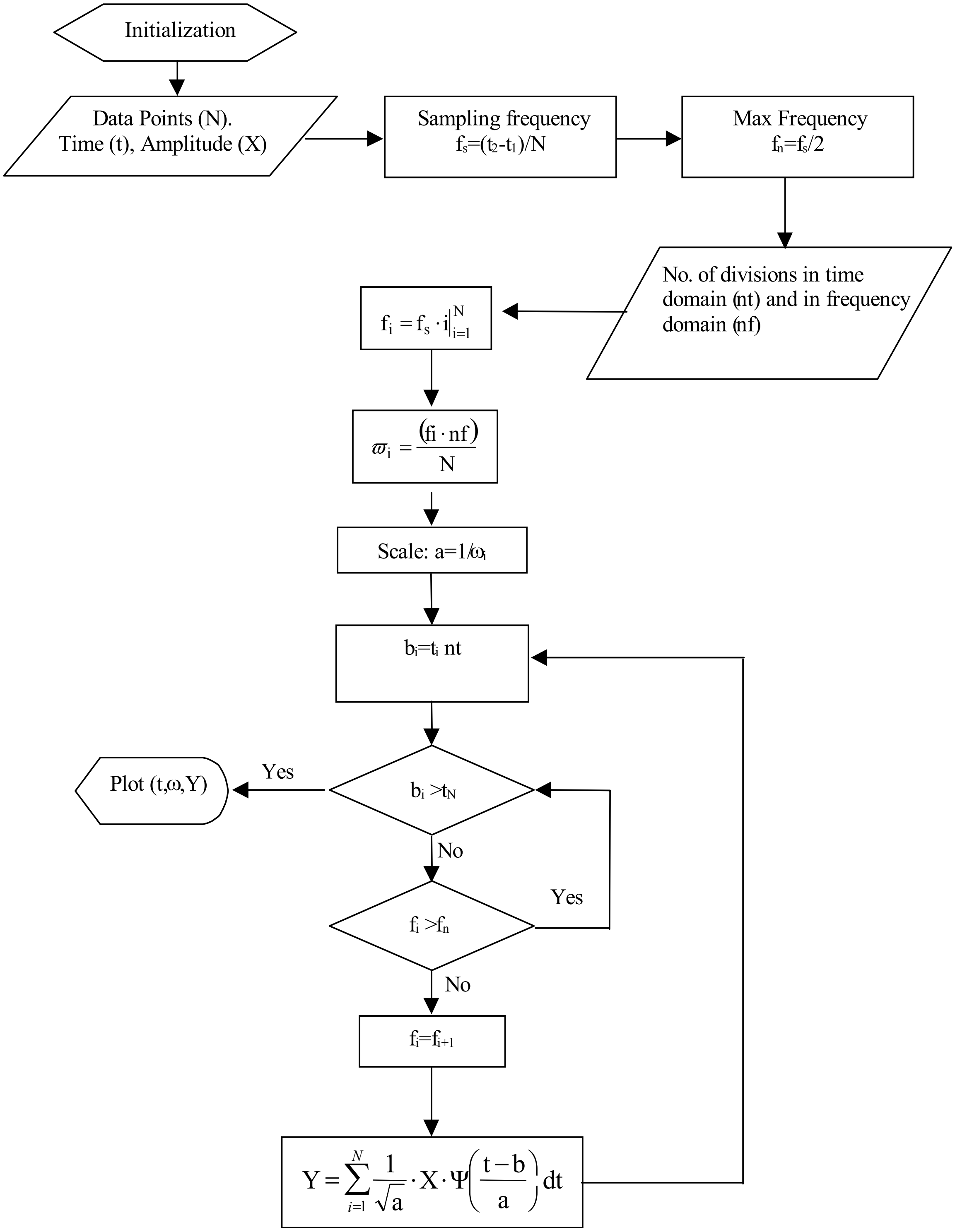

Fig. 3.11--Wavelet transform algorithm. In the case of the Gabor wavelet, the γ is implicit in the function ψ [(t-b)/a] when calculating the coefficients Y.

3.5 Computer Program Validation

In order to validate the Gabor Wavelet Program, several data sets, consisting of known signals were used as inputs, and the program successfully computed Gabor wavelet transforms for Sinusoidal functions, Rayleigh waveform and Lamb waveform. However when trying to analyze data from ultrasonic waves in pipes, some doubts arose in relationship to the "gamma" value in the program because changing that value produces different time-frequency maps. In an attempt to verify that the change of gamma value does not alter the resulting group velocities, and, in order to be sure that it does not make a non-dispersive situation look like a dispersive one, the program was subjected to more testing as follows:

A study of how the sharpness of the envelope in the time domain or the number of oscillations of the analyzing Gabor function, known as "gamma value" affects the Gabor wavelet transform was carried out and the results are presented next. Based on this information, it would be possible to select an appropriate gamma value to be used on the analysis of ultrasonic waves on pipes.

The choice of the analyzing Gabor function cannot be completely arbitrary and should be chosen such that it must satisfy the conditions of equations (3.2), (3.3) and (3.4). For the Gabor wavelet, the zero mean condition (3.3) is only approximately fulfilled for large values of gamma. According to Goupillaud et al.[64], by increasing the gamma value it is possible to reduce the number of terms in the analyzing function, and then making it admissible for Gabor wavelet. However they do not mention how large it should be in order to sufficiently satisfy the admissibility condition and also it is not possible to get arbitrarily sharp localized Gabor wavelets in time, without violating the zero mean condition. Increasing the value arbitrarily could result in loss of information.

A study of the effect of changing the gamma value is presented here by analyzing a Chirp function and then a Rayleigh waveform for values of gamma = 2, 5.366, 10, 20, 30, 50, 70 and 100. Note that the second value of 5.3364 is the value used by Jeong et al.[9], Kishimoto et al.[19], and Goupillaud et al.[64]. Such an odd value is in reality : $\gamma = \pi\sqrt{2/\ln 2}$ which results after calculating the mean value of the Gabor function and approximated to zero. This is in order to comply to the zero mean condition Eq. (3.3), of the wavelets.

Consider the next Chirp function:

$$f(x) = \sin\left(\frac{\omega t_i^2}{t_{\max}}\right) \qquad (3.9),$$

which is shown in figure 3.12, and its Fourier transform in figure 3.13.

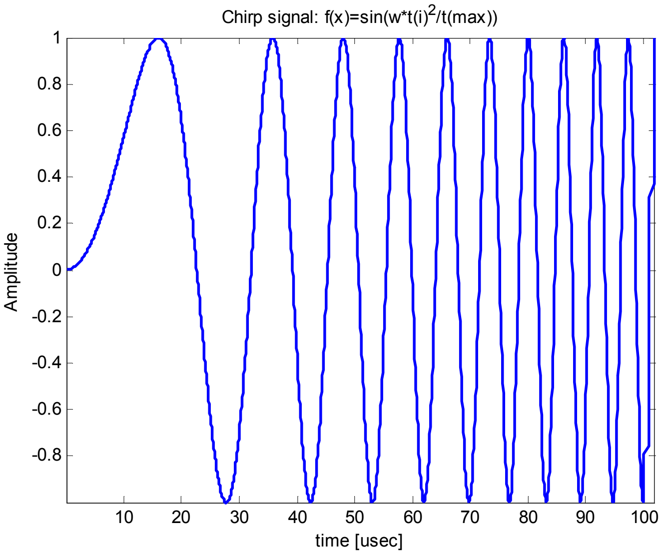

Fig. 3.12—Chirp function used to verify the program.

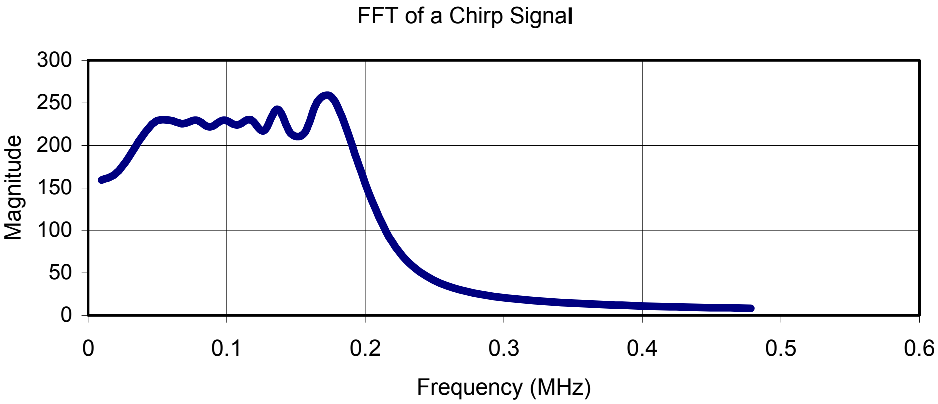

Fig. 3.13—Fast Fourier transform of chirp function. The oscillations are due to the number of points considered for calculating the FFT.

Several values of gamma will be used to analyze the Chirp and then compared in order to see how it affects the wave velocity determination.

As it was mentioned in Chapter II, the dispersion curves can be represented as a two-dimensional plots of velocity Vs. frequency. In this case, because velocity is directly related to arrival times, by a known propagation distance, it is possible to represent the dispersion curves as a time-frequency representation, which in turn corresponds to the Gabor wavelet representation. Additionally to have a more clear idea of how disperse a signal could be, the maxima of the wavelet coefficients corresponding to arrival times of each frequency content is plot as blue crosses and a curve-fitting fifth order polynomial is employed to average those points and represented at the same graph as a continuous red line. A fifth order fitting polynomial is used because the frequency equation according to the Mirsky-Herrmann theory, has five roots and thus produces dispersion curves for five modes.

The next sequenced plots, from figure 3.14 to figure 3.21 show dispersion curves for the chirp of figure 3.12 showing actual arrival times (cross points), with curve fitting (solid line) and the corresponding Gabor Wavelet transforms, whose amplitude goes increasingly from dark blue to red, for each gamma value (γ) represented on the graph as G.

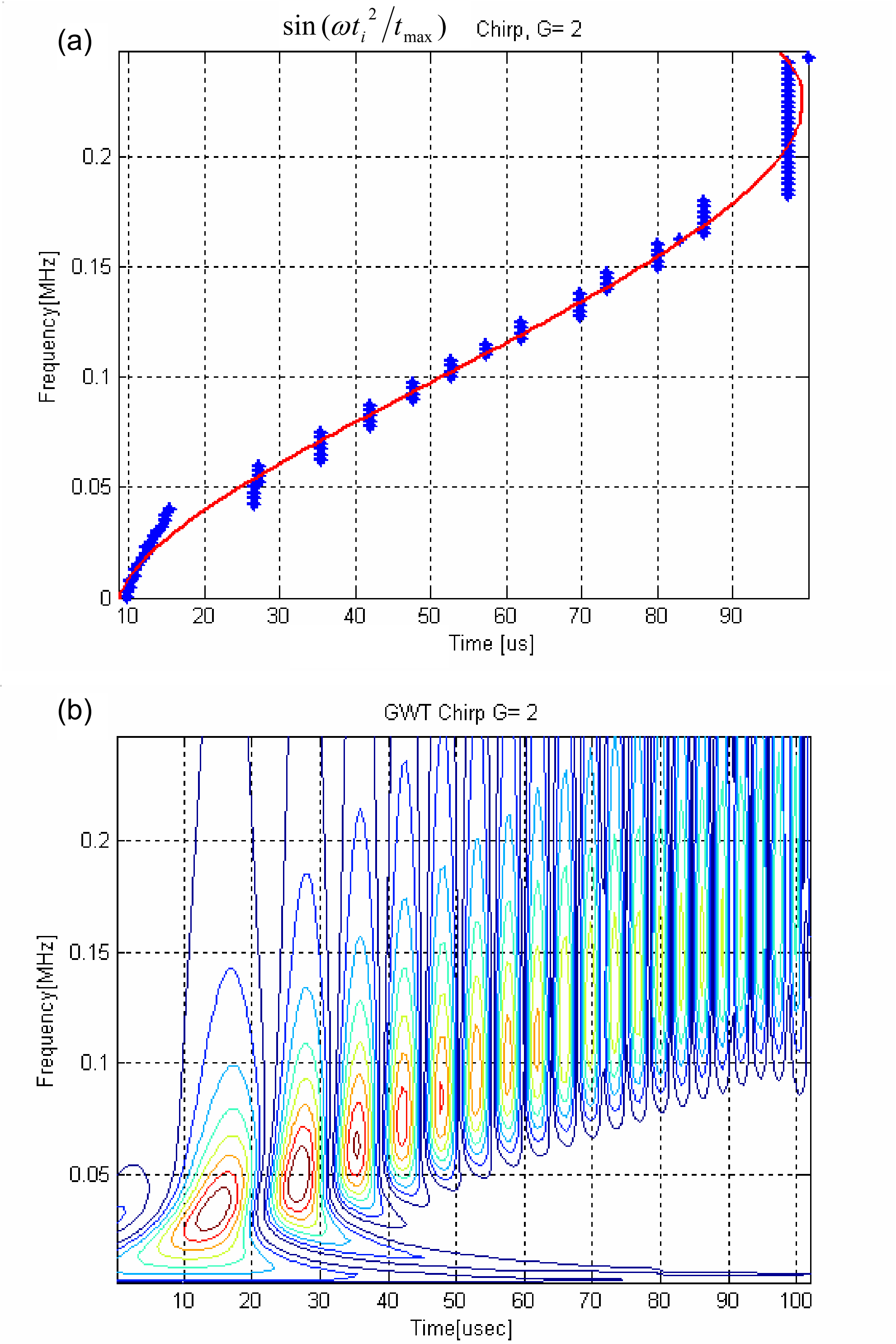

Fig. 3.14—(a) Dispersion curve for a chirp, showing actual arrival times (blue crosses) and fitted time–frequency map (solid red line). (b) Corresponding Gabor wavelet with γ =2.

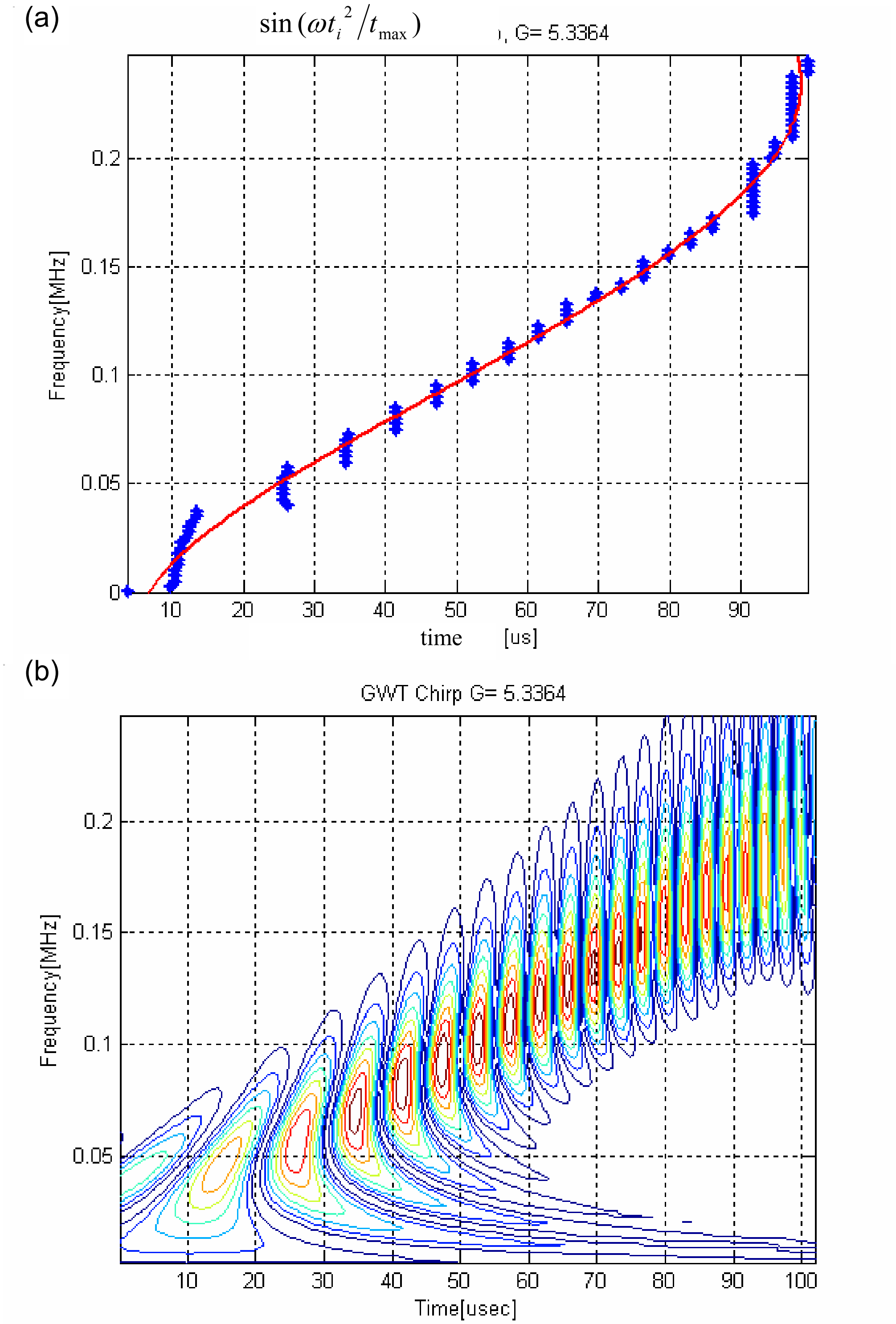

Fig. 3.15—(a) Dispersion curve for a chirp, showing actual arrival times (blue crosses) and fitted time–frequency map (solid red line). (b) Corresponding Gabor wavelet with γ = 5.3364.

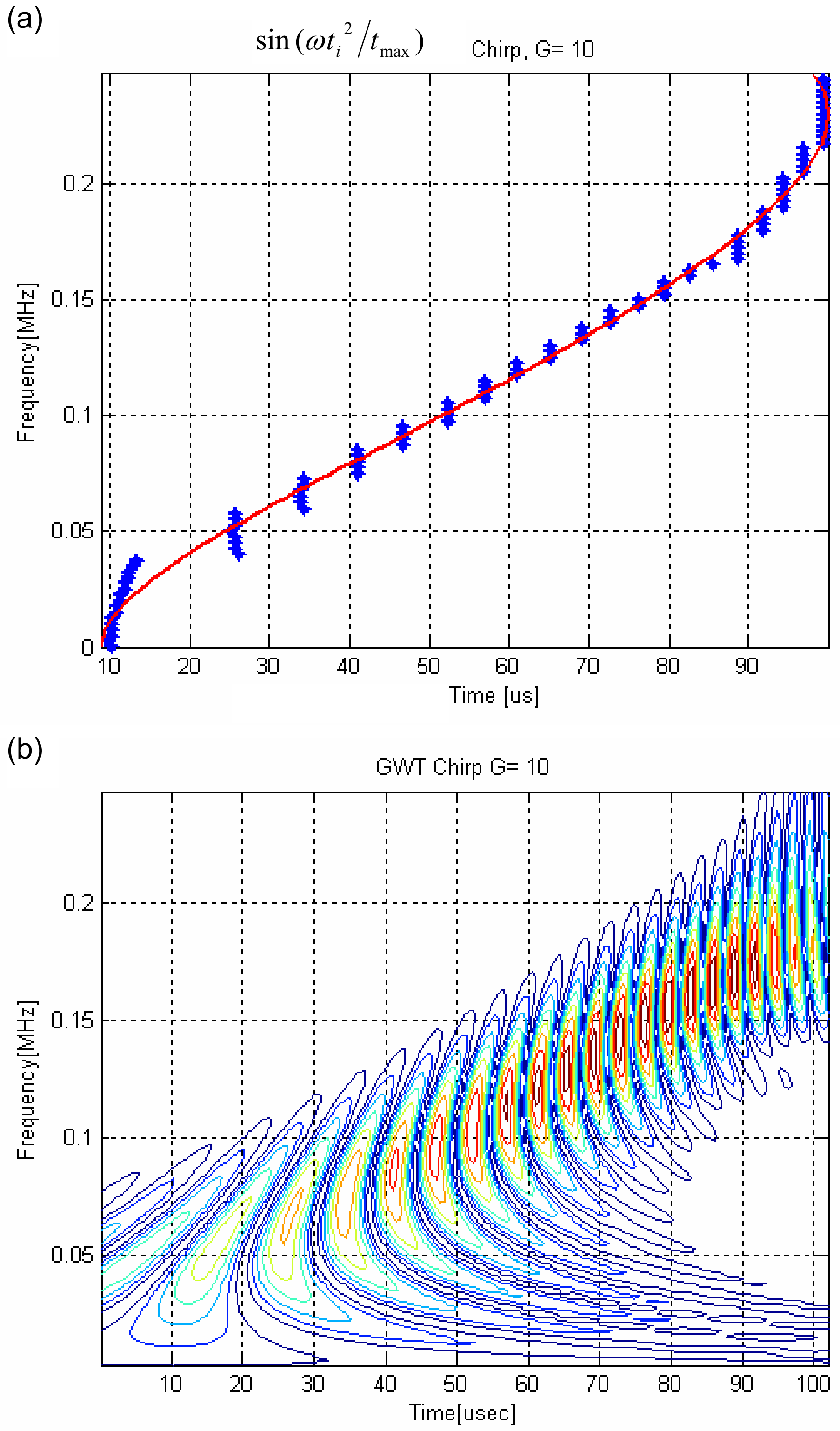

Fig. 3.16—(a) Dispersion curve for a chirp, showing actual arrival times (blue crosses) and fitted time–frequency map (solid red line). (b) Corresponding Gabor wavelet with γ = 10.

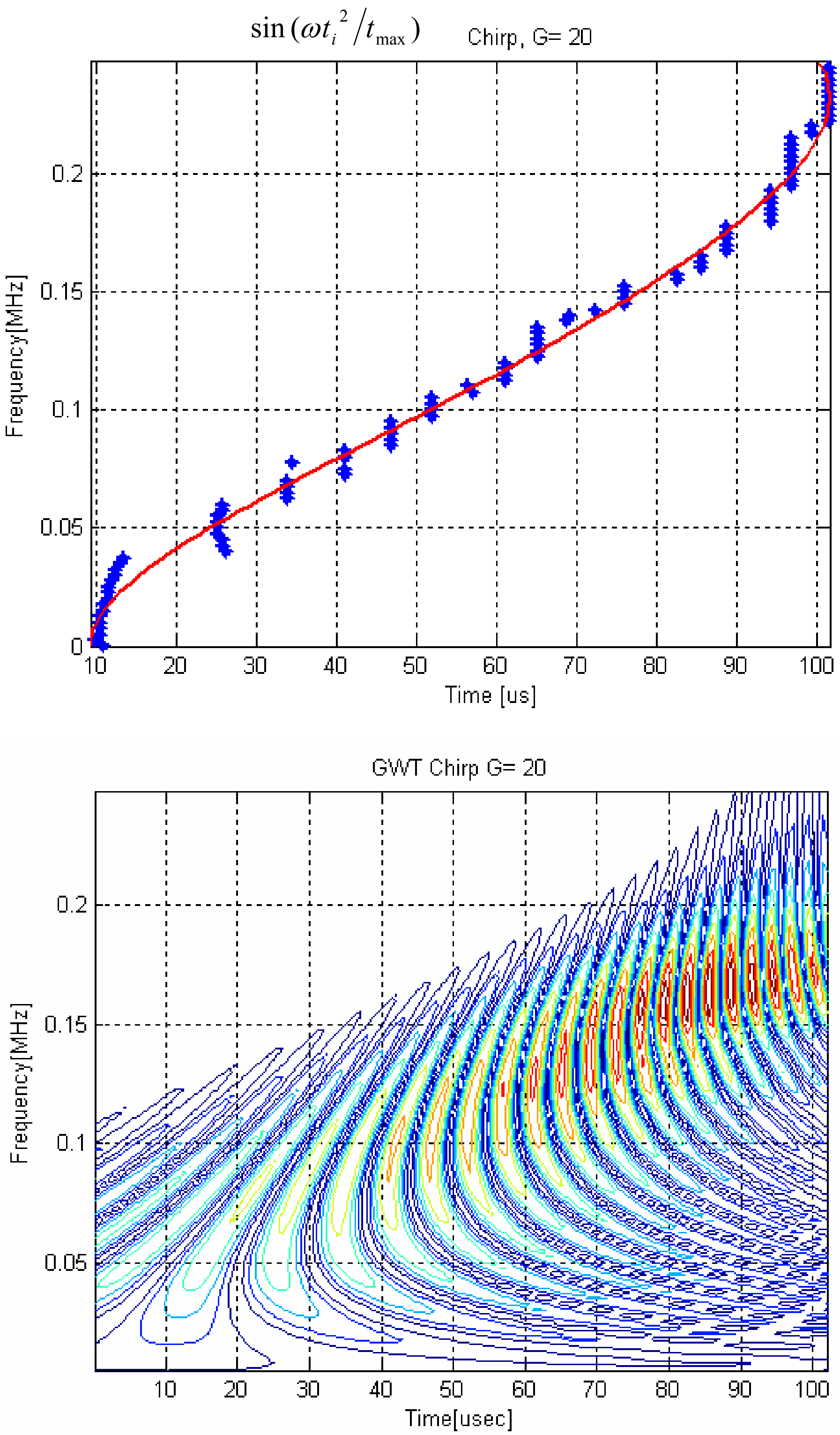

Fig. 3.17——(a) Dispersion curve for a chirp, showing actual arrival times (blue crosses) and fitted time–frequency map (solid red line). (b) Corresponding Gabor wavelet with γ = 20.

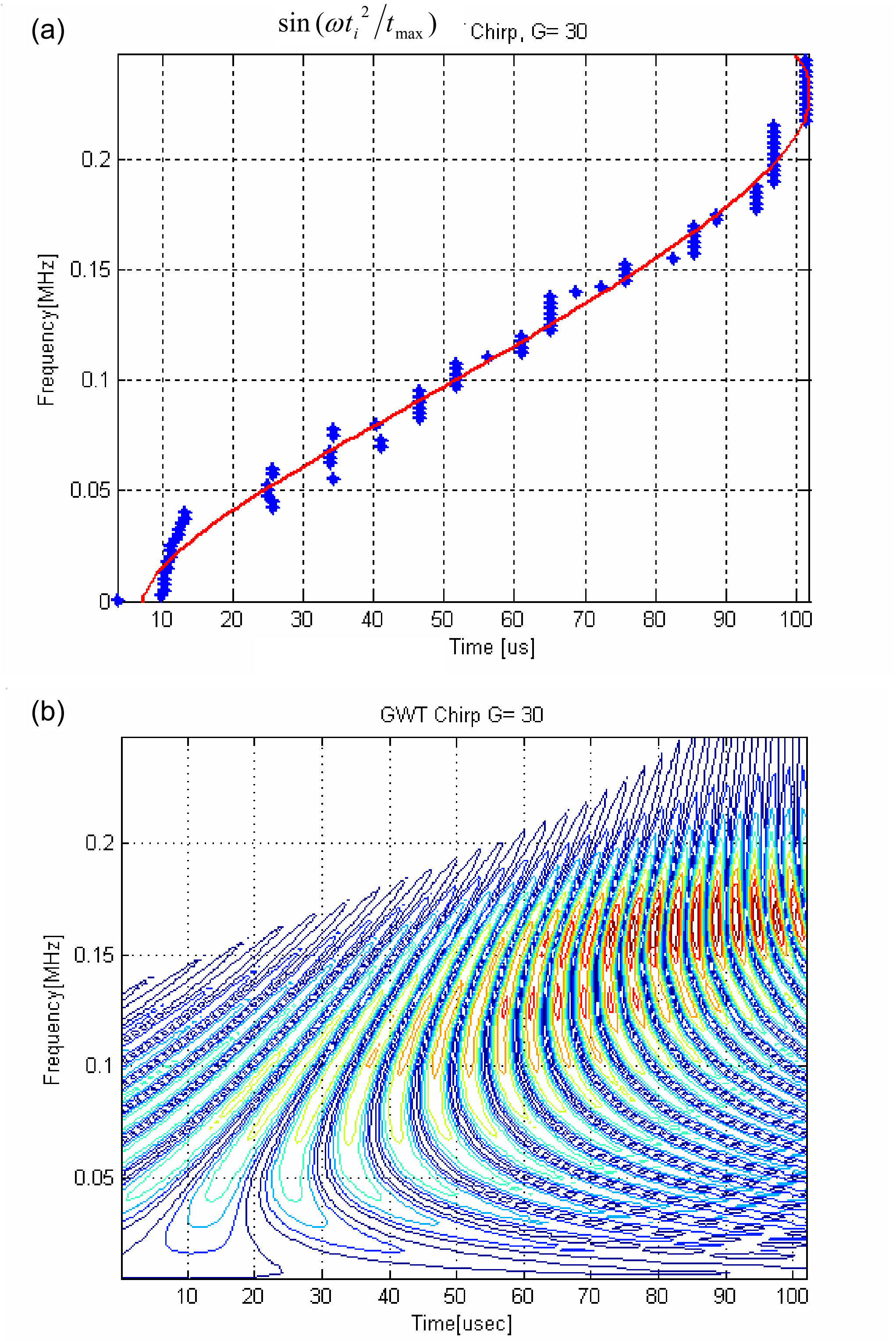

Fig. 3.18—(a) Dispersion curve for a chirp, showing actual arrival times (blue crosses) and fitted time–frequency map (solid red line). (b) Corresponding Gabor wavelet with γ = 30.

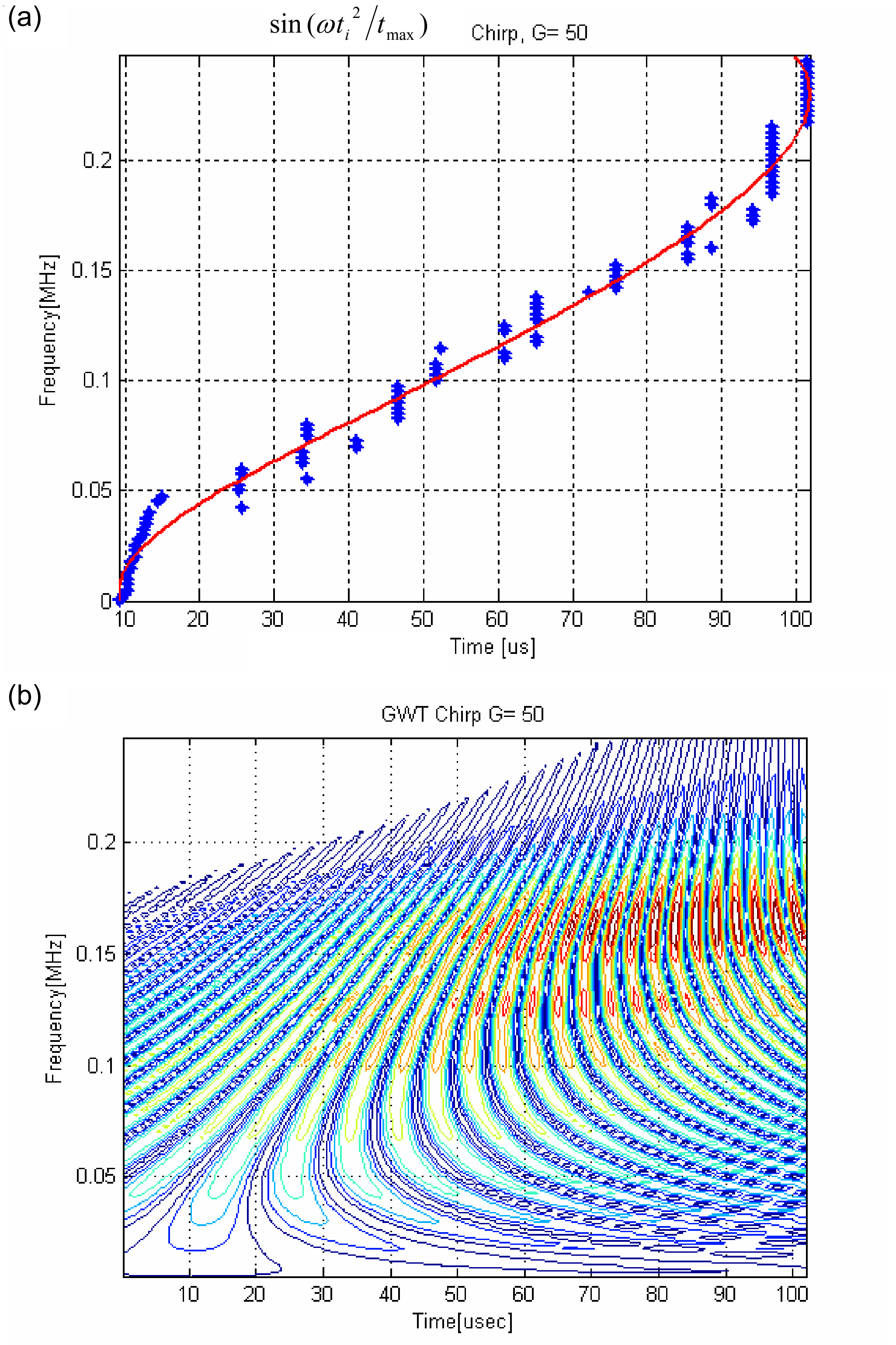

Fig. 3.19—(a) Dispersion curve for a chirp, showing actual arrival times (blue crosses) and fitted time–frequency map (solid red line). (b) Corresponding Gabor wavelet with γ = 50.

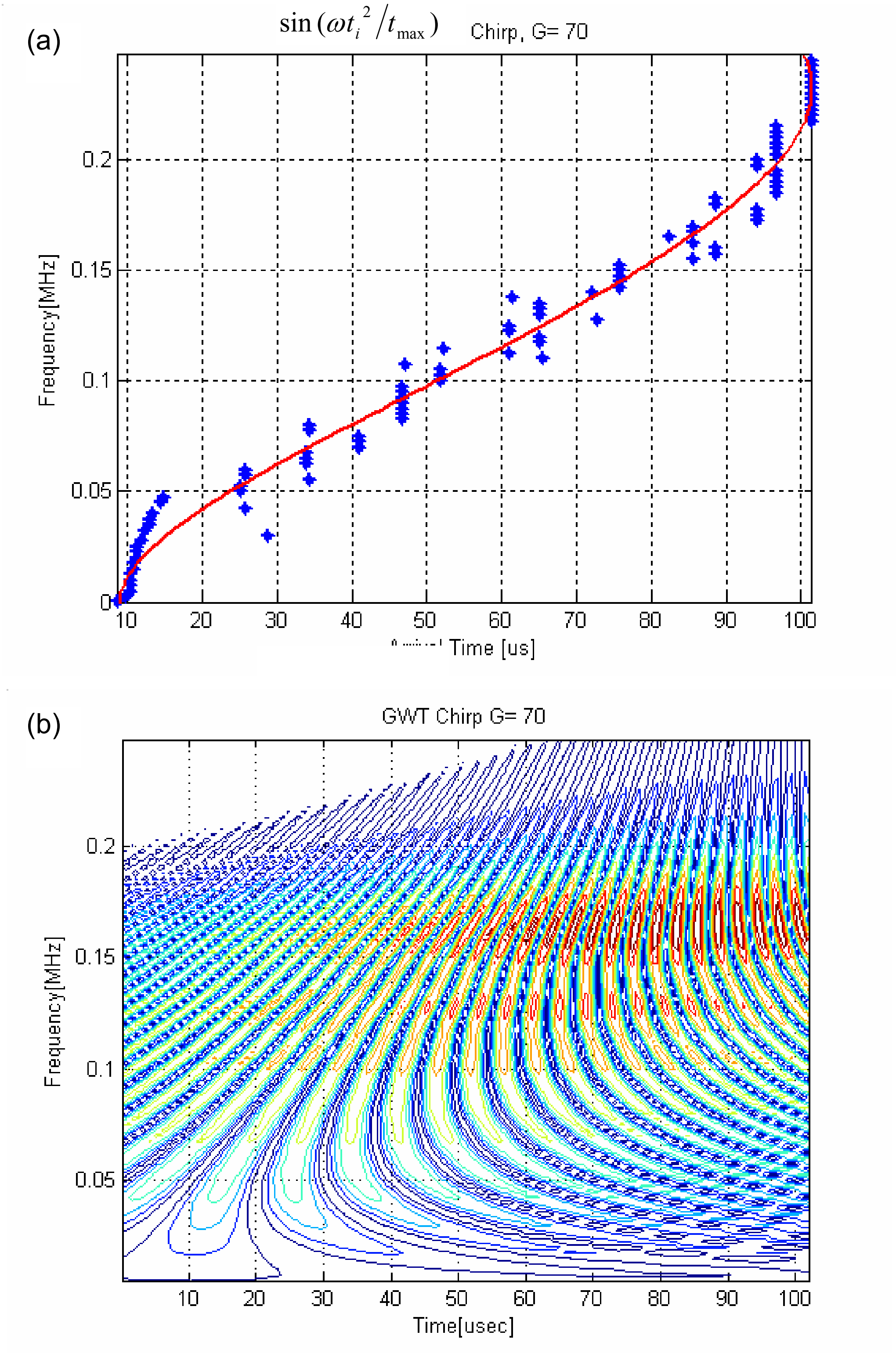

Fig. 3.20—(a) Dispersion curve for a chirp, showing actual arrival times (blue crosses) and fitted time–frequency map (solid red line). (b) Corresponding Gabor wavelet with $\gamma = 70$.

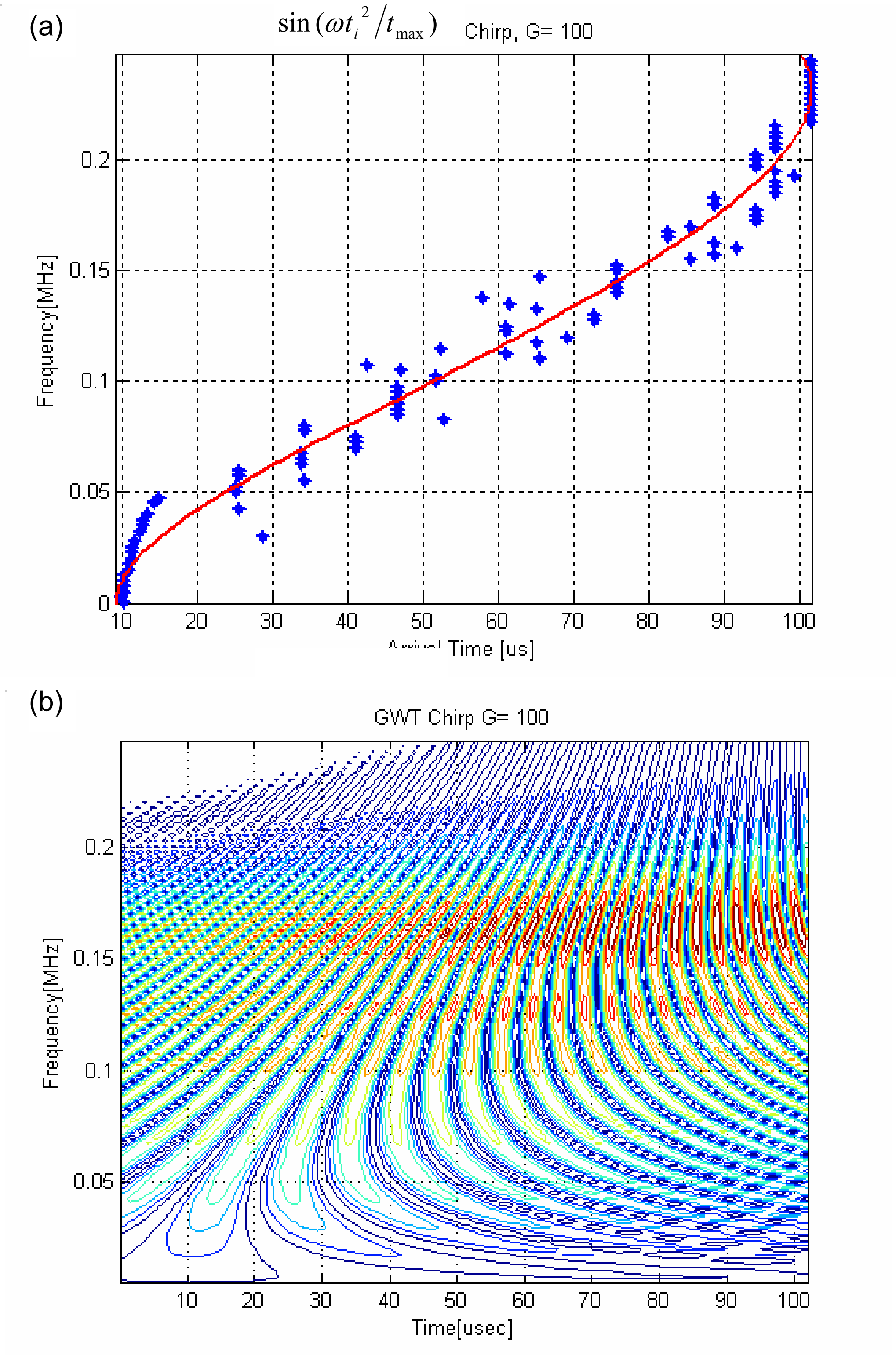

Fig. 3.21—(a) Dispersion curve for a chirp, showing actual arrival times (blue crosses) and fitted time–frequency map (solid red line). (b) Corresponding Gabor wavelet with γ = 100.

It can be seen on figures 3.14(a)-3.21(a) that there is some data spread above and below the trend line (solid red line). This pattern of "spreading out" data is more noticeable as the gamma value increases. Although it can be observed also that the overall trend is the same regardless of the gamma value, for this particular example, some major differences were found at high and low level frequencies. This can be shown by taking all the sets for each gamma and Fitting the actual dispersion points from the Chirp function, Eq. (3.9) into a 5^{th} order polynomial as shown on figure 3.22. As mentioned before, a fifth order polynomial was chosen in order to correspond to the frequency equation (2.25) of the dispersion relation for cylinders, which will be applied to the actual test specimen, and it is a fifth order system.

All the curves are very consistent in about 80% along the time span and 60% along frequency span. The remaining 20% and 40% of time and frequency spans correspond to the ends, where the points show a spreading effect.

The dispersion plots were obtained directly from the calculated wavelet coefficients, by getting the maxima of the wavelet coefficients corresponding to the arrival time for each frequency component., in a discrete approach.

Classically the discrete Wavelet transform is defined for sequences with length of some power of two, and different ways of extending samples of other sizes are needed. The algorithm used here for the Wavelet transform is not limited to dyadic length and is based on a convolution scheme. And, when a convolution is performed on finite-length signals, border distortions arise.

There is a possibility that those differences at the ends of the dispersion curves could be also the result of the "edge effects" also known as border distortion, inherent of the wavelet transform algorithm. These edge effects usually make the data appear as if they were spread at the beginning and the end of the time-frequency plot.

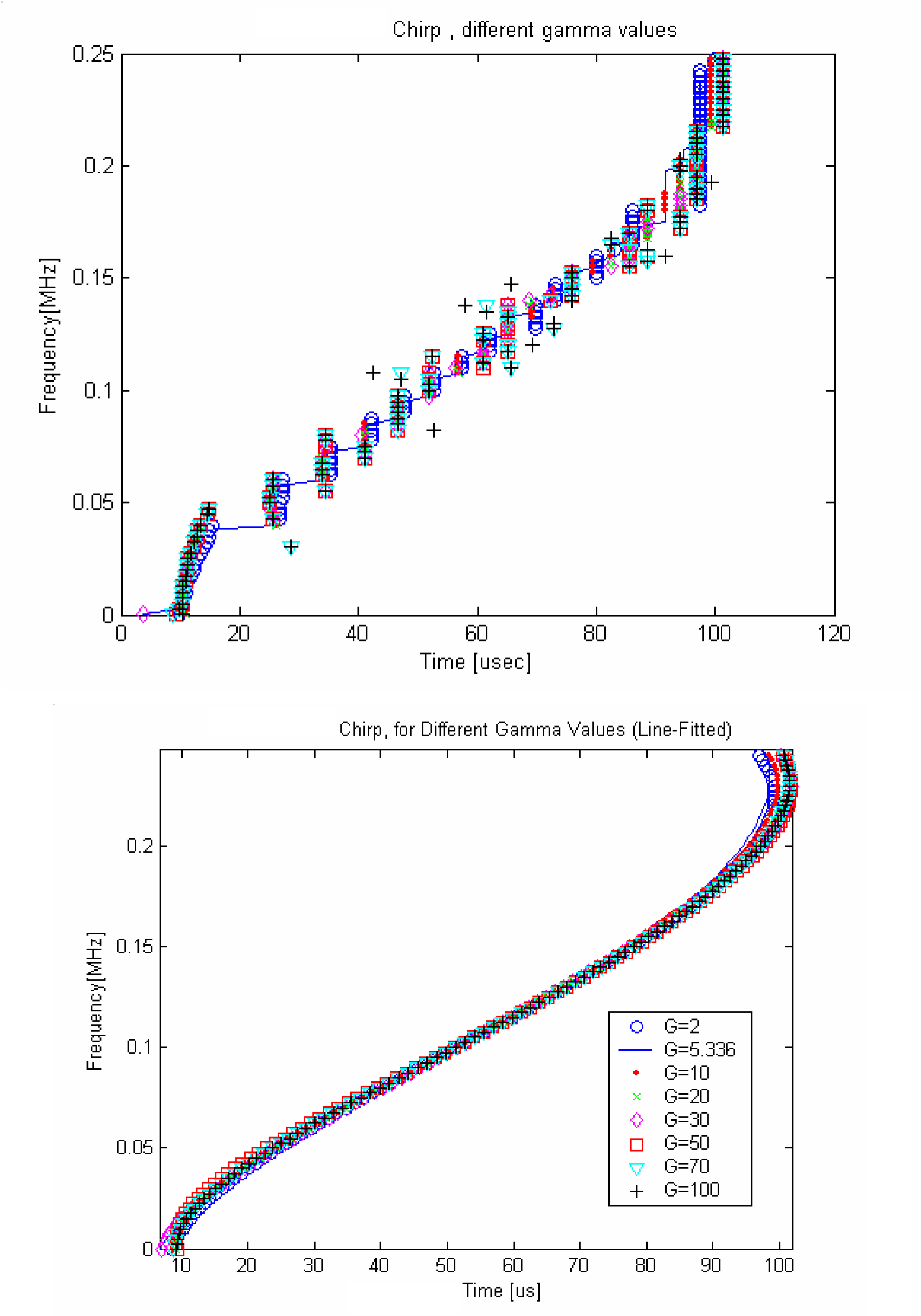

Fig. 3.22—Dispersion curves for different gamma values, raw data (above) and 5th degree polynomial fitted (below).

Two zoomed views from dispersion curves on figure 3.22 are shown on figures 3.23 and 3.24 to clearly notice the spreading effect of data at low and high frequencies. The value of gamma=5.3364 is taken as the reference and it is shown as a solid line on the plots. Also, from the Gabor wavelet plots from figures 3.14(b) to 3.21(b) it is easier to recognize a trend pattern on dispersion curves when using gamma values of γ=2, 5.336

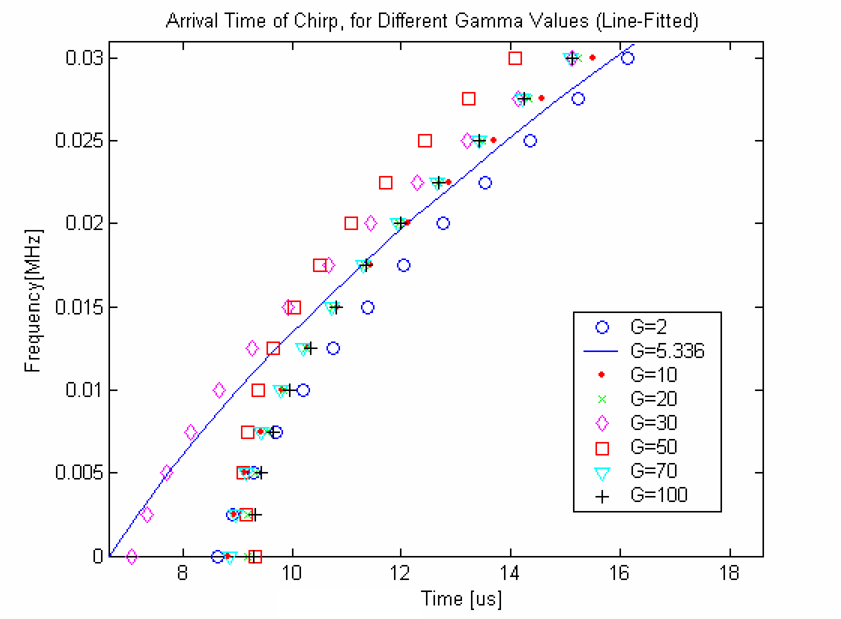

Fig. 3.23—Dispersion of Chirp. Amplification at lower end.

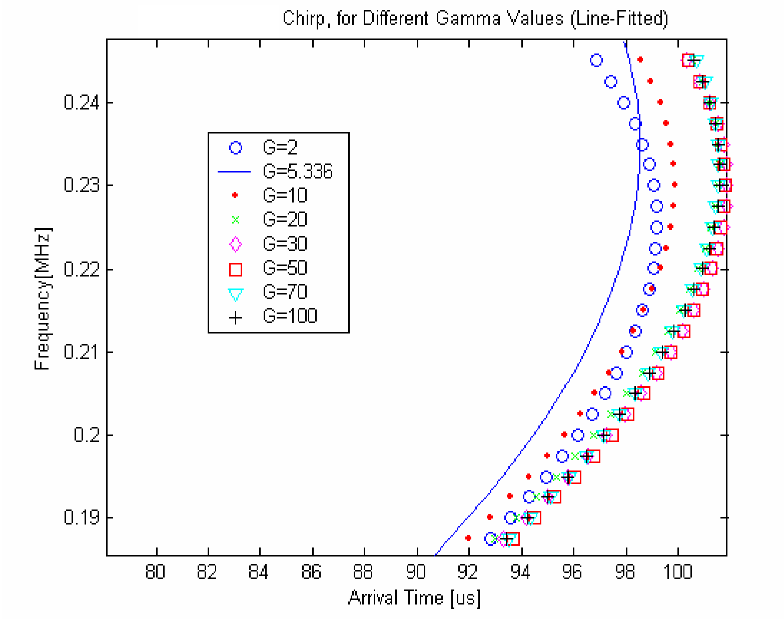

Fig. 3.24—Dispersion of Chirp. Amplification at upper end.

and $\gamma=10$. If a greater value of γ is used, then the data points scatters on the frequency-time map. Also it can be observed that extra frequency bands appear. This is because there is an increase in frequency resolution, but time localization is being compromised. However, when averaging the arrival times by curve fitting, the data are still between certain trend limits. At this point, it can be said that for a Chirp signal as defined by Eq. (3.9) , a change on γ does not represent a significant change on dispersion curves

The next step was to validate the program with a "real" Rayleigh waveform obtained from experimentation, like the one shown in figure 3.25, and its Fourier transform shown in figure 3.26.

A thick flat steel plate was used to generate the Rayleigh waveform, and the parameters used on the experiment were as follows:

Input energy = 350mJ,
spot diameter d_s=1mm,
travel distance ℓ = 40mm,
thickness h=38mm.

As it can be seen on figure 3.25, the arrival time of the propagating wave was 14μs, which for a travel distance of 40mm, corresponds to a wave velocity of 2.9mm/μs, which is the Rayleigh wave velocity in steel. Note that the waveform is noisy, and as is has been mentioned before, there are several sources of noise, one of those can be due to the unclean generating beam profile. As it can be seen on the FFT plot on figure 3.26, the useable frequency, is below 4MHz. Then a frequency range of 0-4MHz is considered.

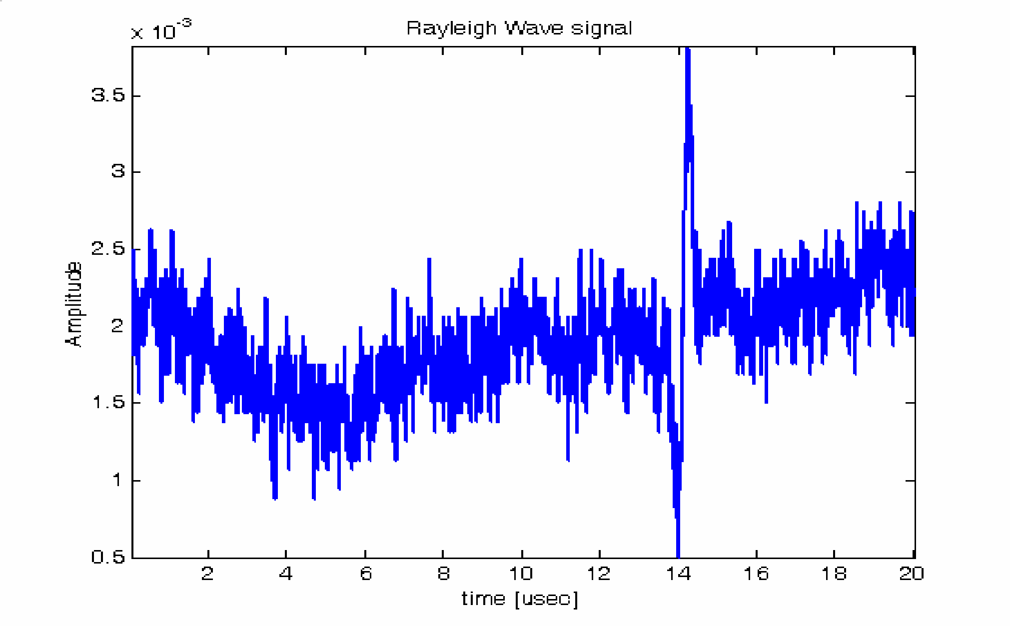

Fig. 3.25—Rayleigh Waveform obtained from experimentation.

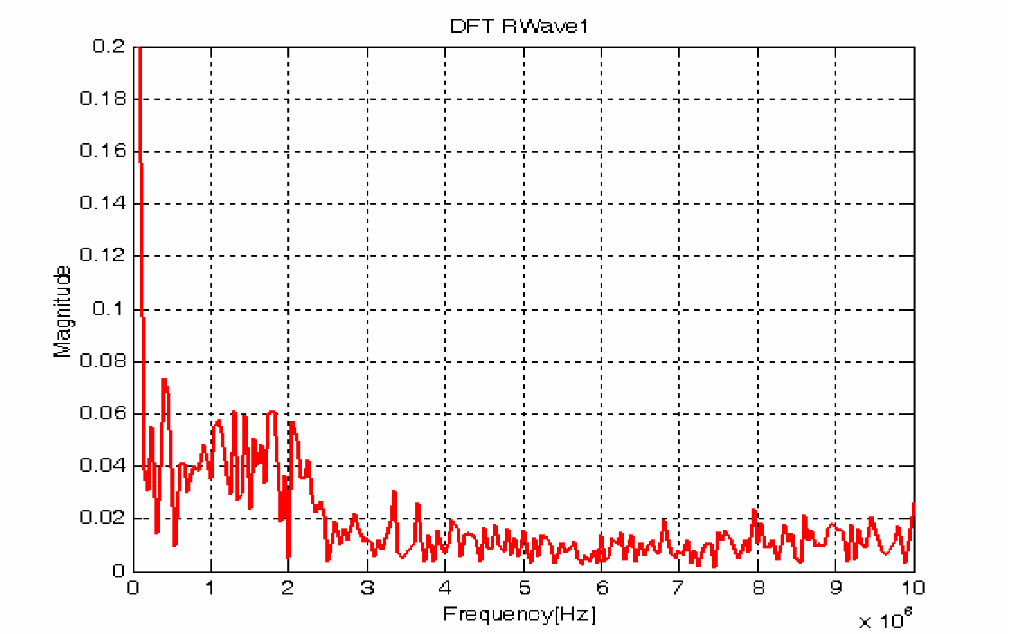

Fig. 3.26—Discrete Fourier Transform of Rayleigh Waveform from figure 3.22.

Several values of gamma will be considered to analyze the Rayleigh waveform and then compared in order to see how it affects the wave velocity determination.

Again, as in the case of the chirp function, the dispersion curves can be represented as two-dimensional plots of time-frequency maps, which in turn correspond to the Gabor wavelet representations, because the velocity is directly related to arrival times, by a known propagation distance. Additionally to have a more clear idea of how disperse a signal could be, the maxima of the wavelet coefficients corresponding to arrival times of each frequency content are plot as blue crosses and a curve-fitting fifth order polynomial is employed to average those points and represented at the same graph as red points. A fifth order fitting polynomial is used because the frequency equation according to the Mirsky-Herrmann theory, has five roots and thus produces dispersion curves for five modes.

The next sequenced plots in figures 3.27 to 3.34, show dispersion curves for the Rayleigh waveform of figure 3.25. Showing in the upper plot the blue cross points corresponding to the actual arrival times for each frequency content, and the red dotted points correspond to the average by curve fitting. Whereas in the lower plot shows the corresponding Gabor wavelet transforms, whose amplitude goes increasingly from dark blue to red, for each gamma value (γ) represented on the graph as G.

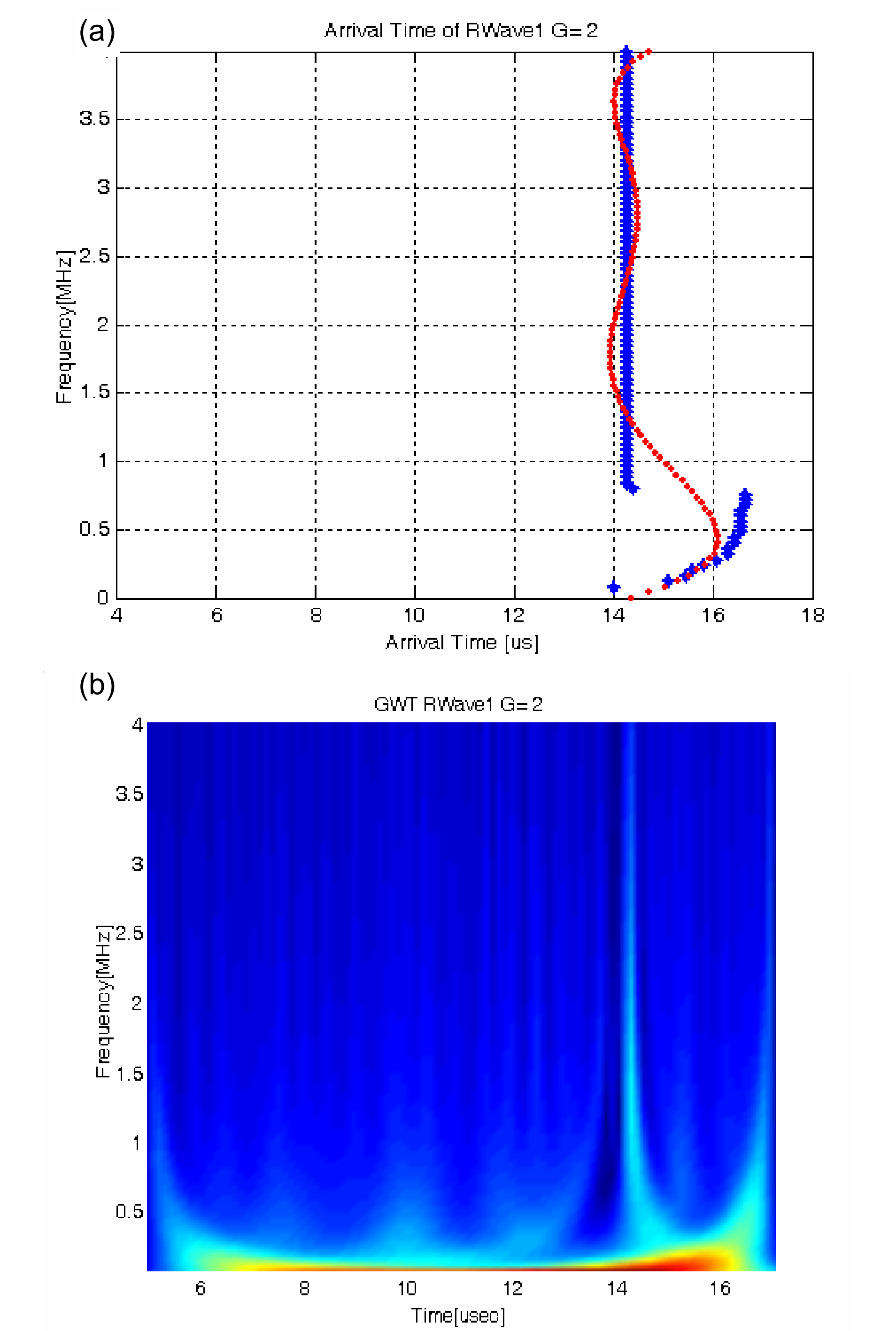

Fig. 3.27— (a) Dispersion curve for a Rayleigh waveform, showing actual arrival times (blue crosses) and fitted time–frequency map (red dots). (b) Corresponding Gabor wavelet with $\gamma = 2$.

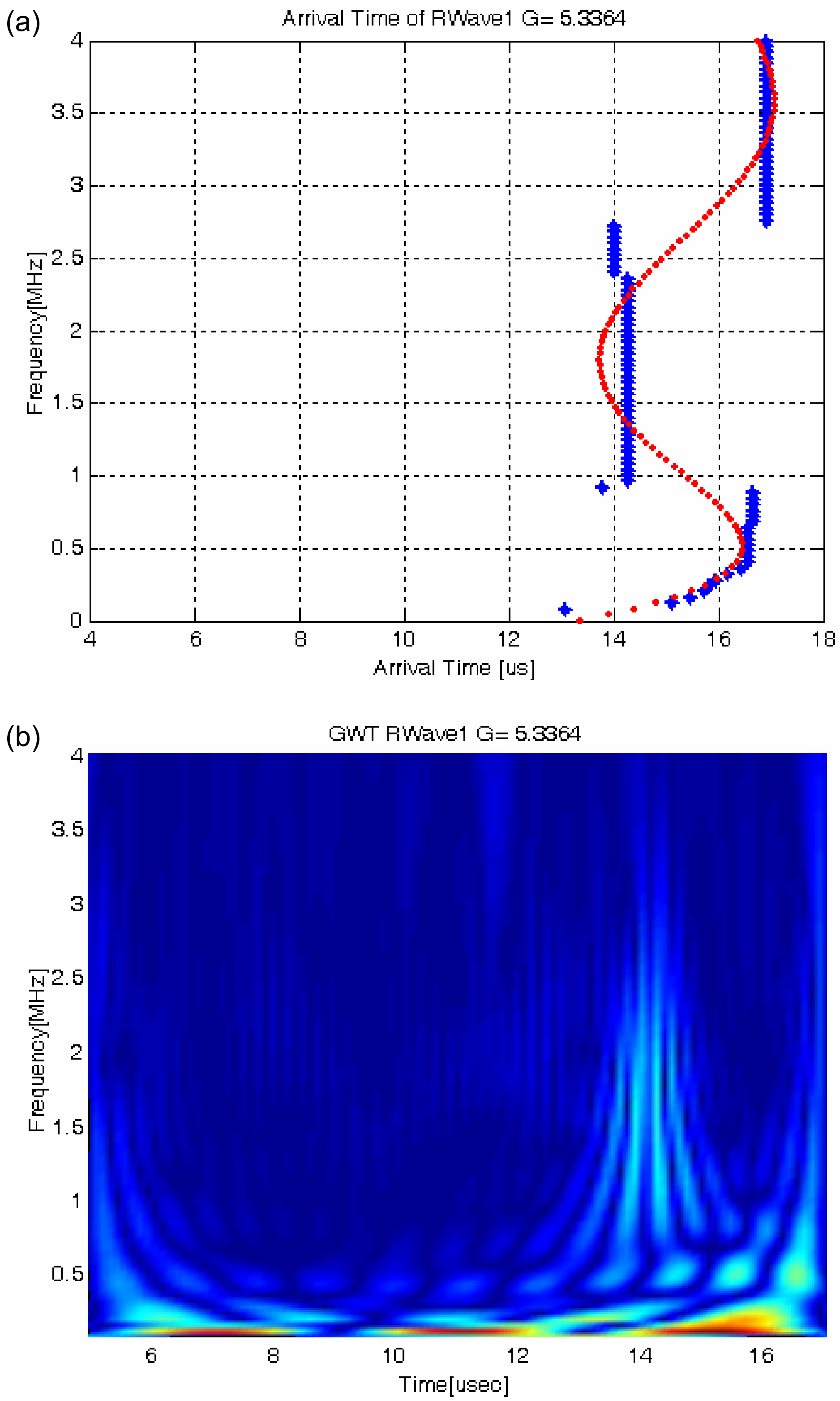

Fig. 3.28 —(a) Dispersion curve for a Rayleigh waveform, showing actual arrival times (blue crosses) and fitted time–frequency map (red dots). (b) Corresponding Gabor wavelet with γ =5.3364.

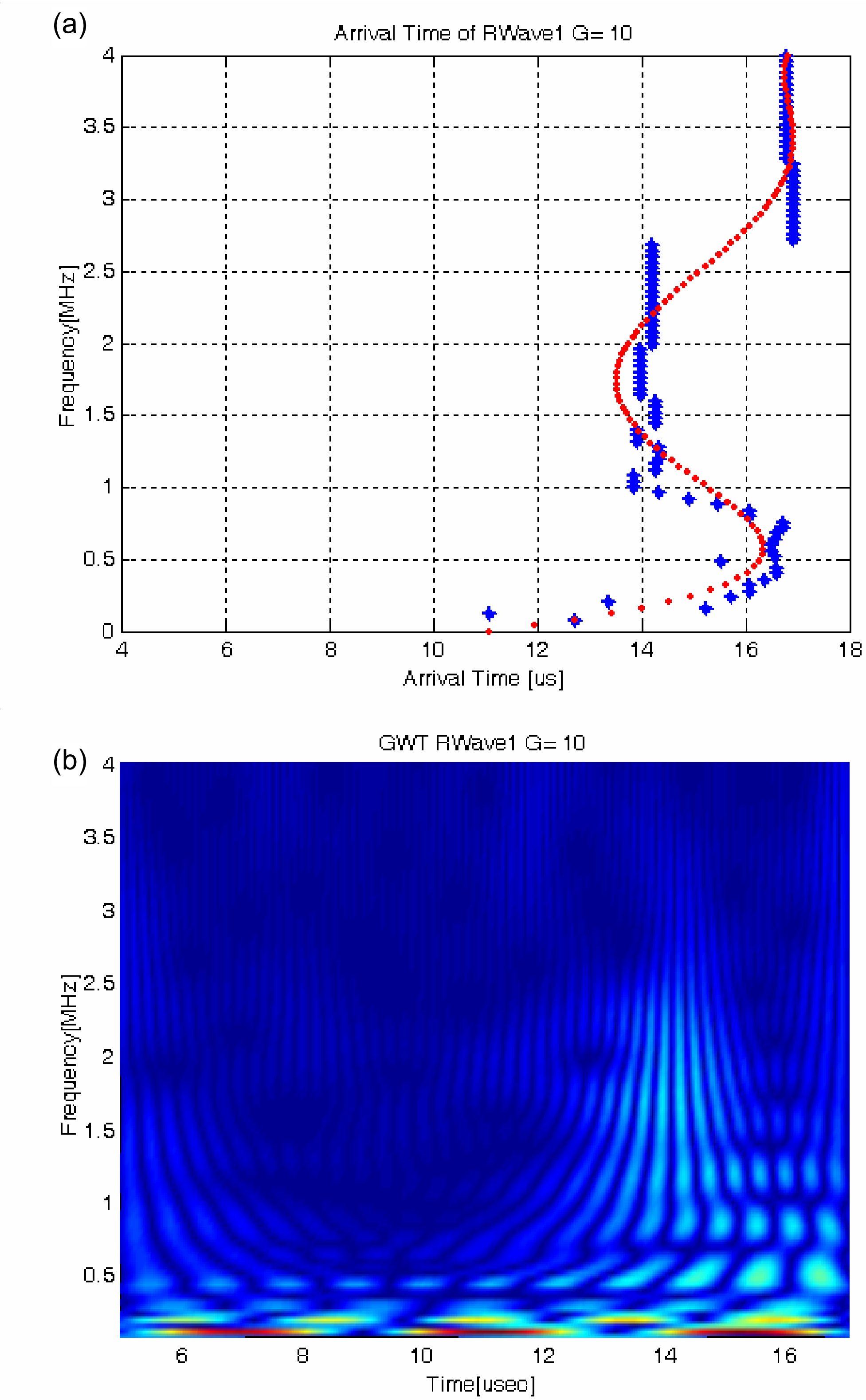

Fig. 3.29—(a) Dispersion curve for a Rayleigh waveform, showing actual arrival times (blue crosses) and fitted time–frequency map (red dots). (b) Corresponding Gabor wavelet with γ =10.

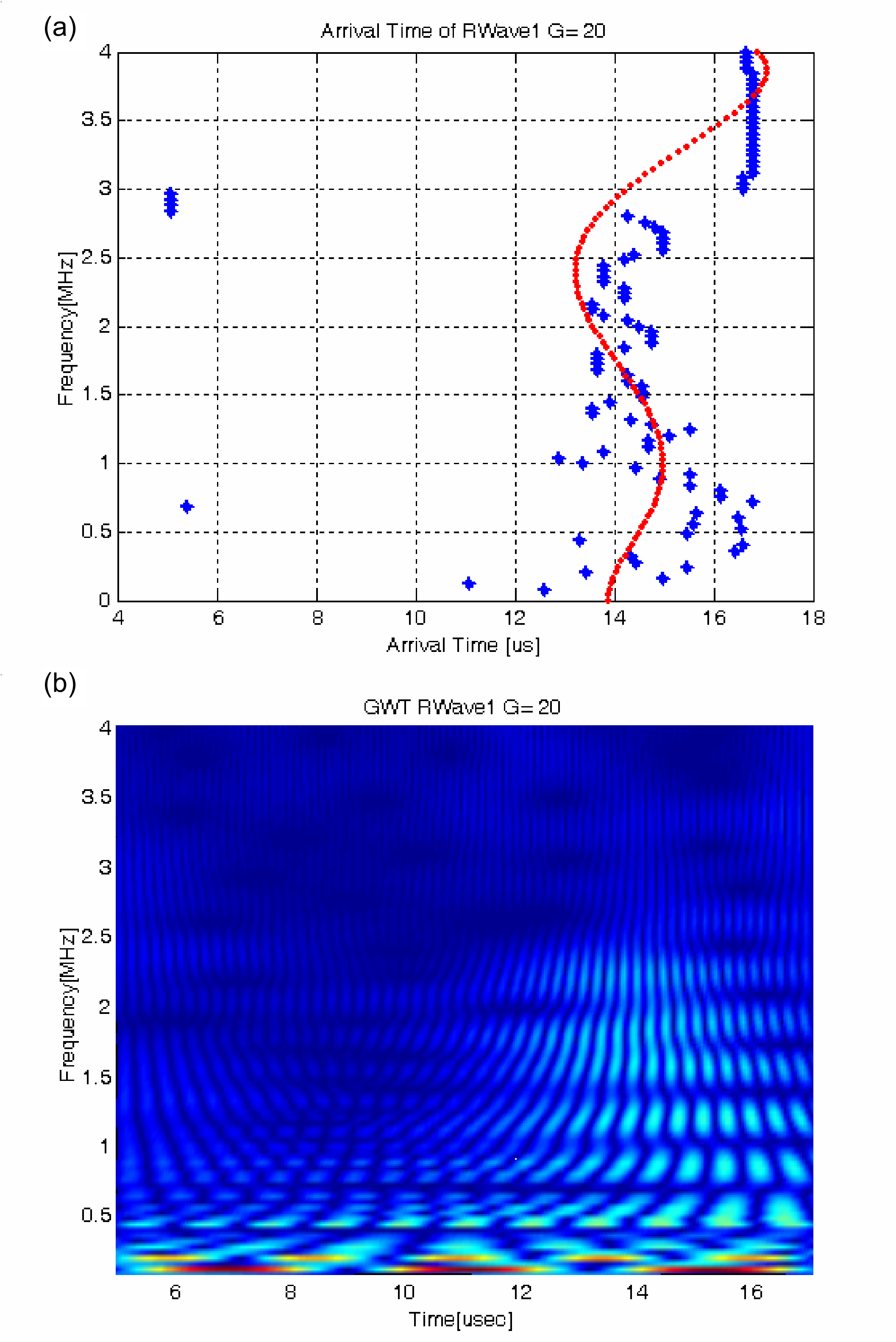

Fig. 3.30—(a) Dispersion curve for a Rayleigh waveform, showing actual arrival times (blue crosses) and fitted time–frequency map (red dots). (b) Corresponding Gabor wavelet with γ =20.

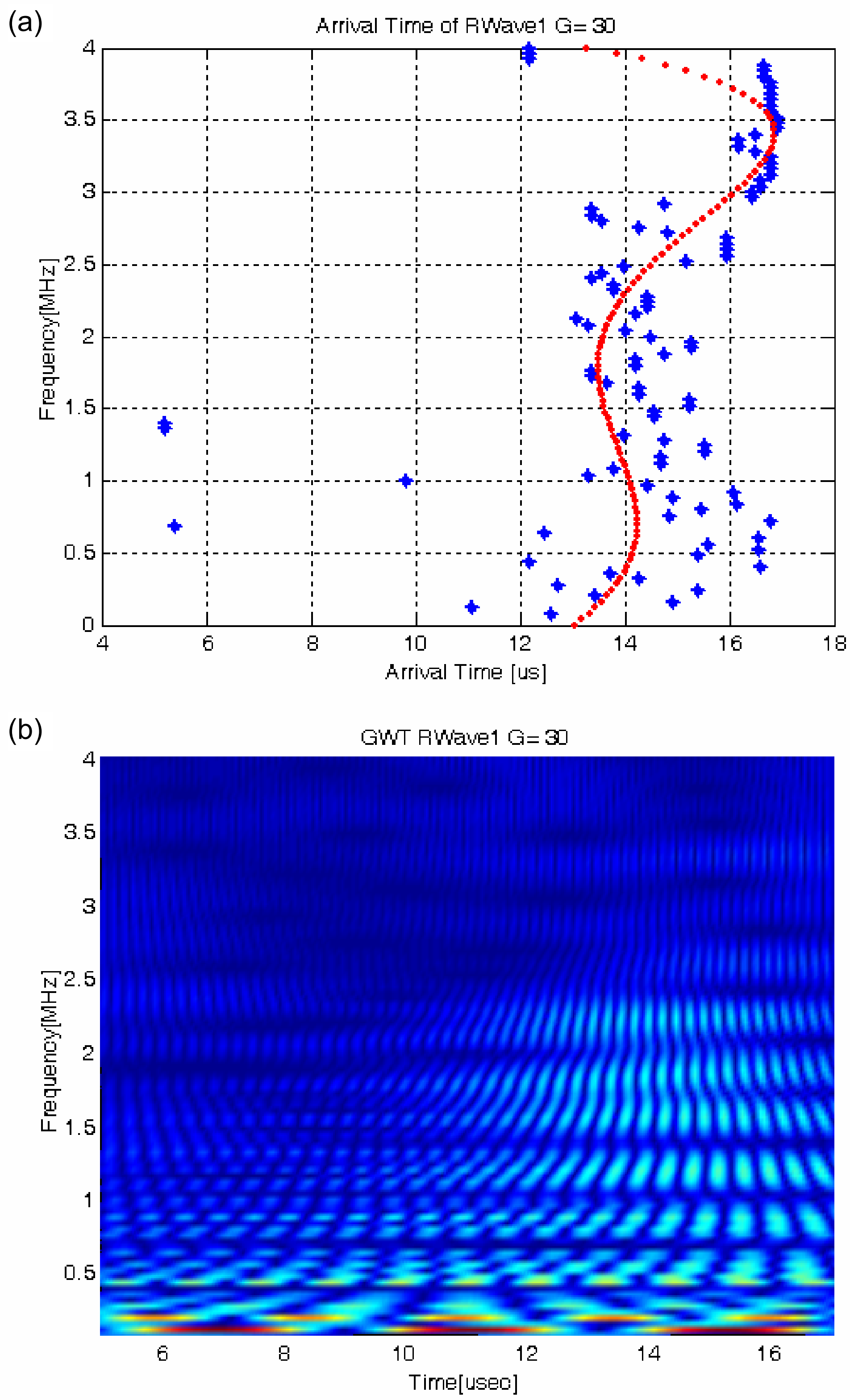

Fig. 3.31—(a) Dispersion curve for a Rayleigh waveform, showing actual arrival times (blue crosses) and fitted time–frequency map (red dots). (b) Corresponding Gabor wavelet with γ =30.

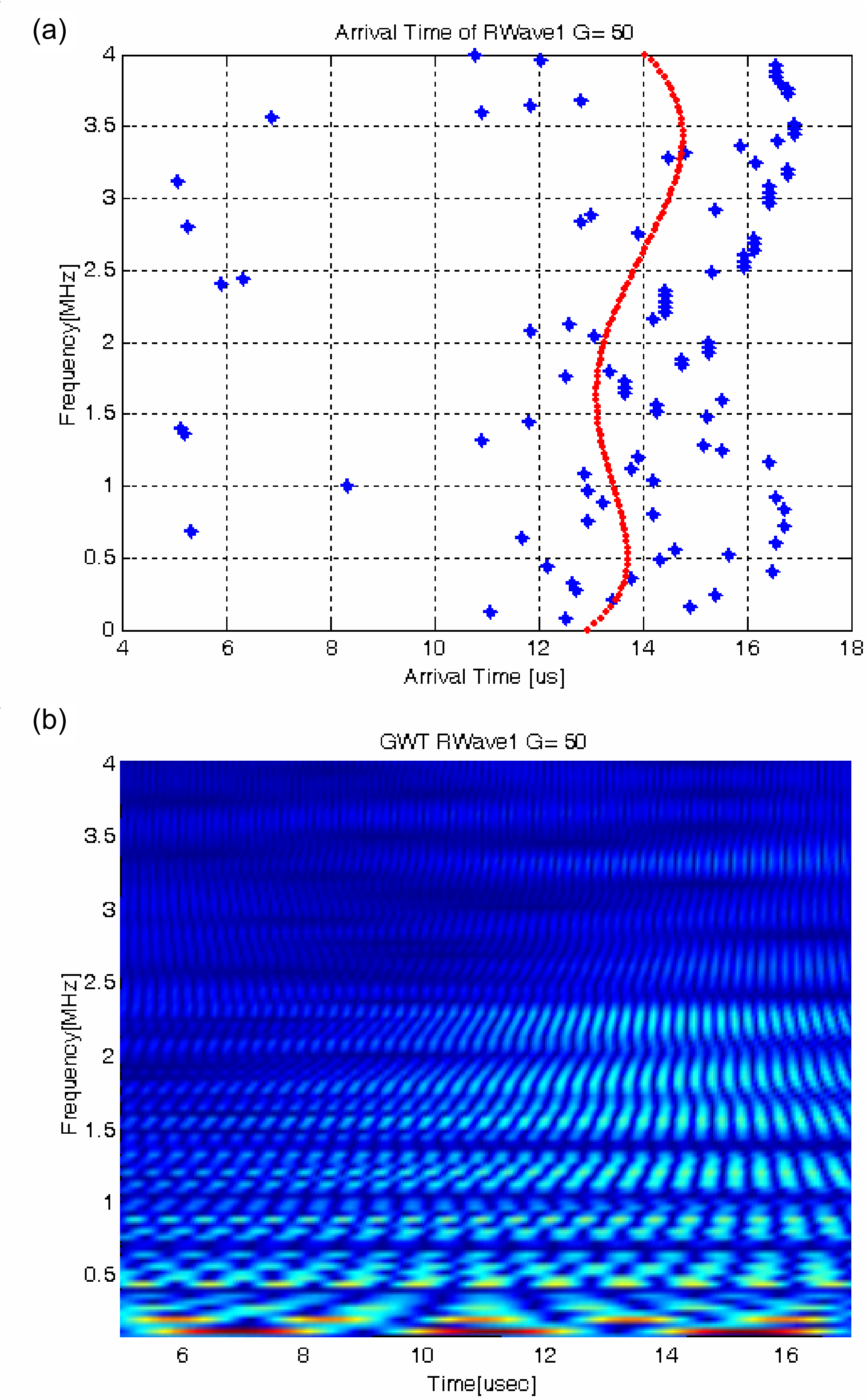

Fig. 3.32—(a) Dispersion curve for a Rayleigh waveform, showing actual arrival times (blue crosses) and fitted time–frequency map (red dots). (b) Corresponding Gabor wavelet with γ =50.

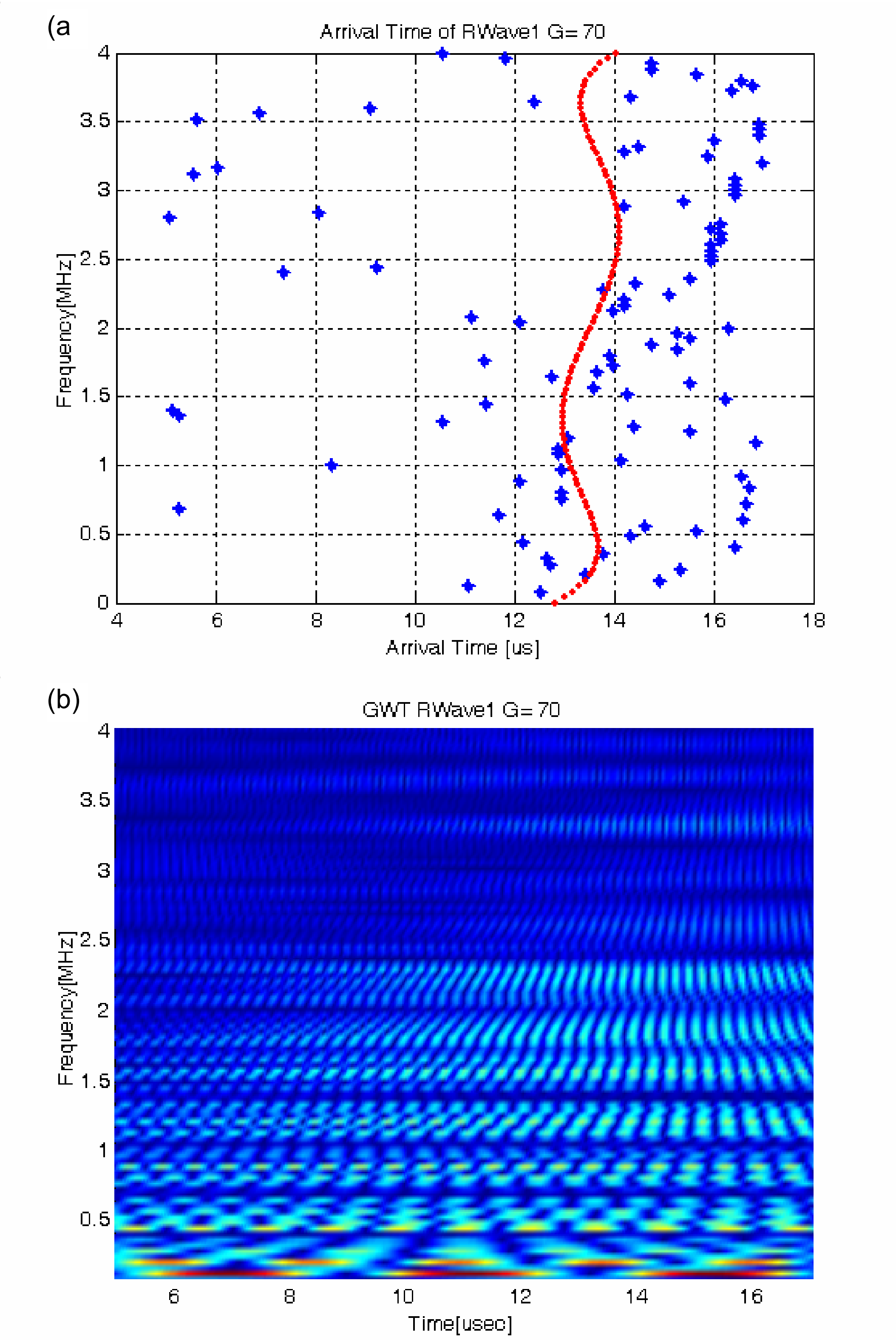

Fig. 3.33—(a) Dispersion curve for a Rayleigh waveform, showing actual arrival times (blue crosses) and fitted time–frequency map (red dots). (b) Corresponding Gabor wavelet with γ =70.

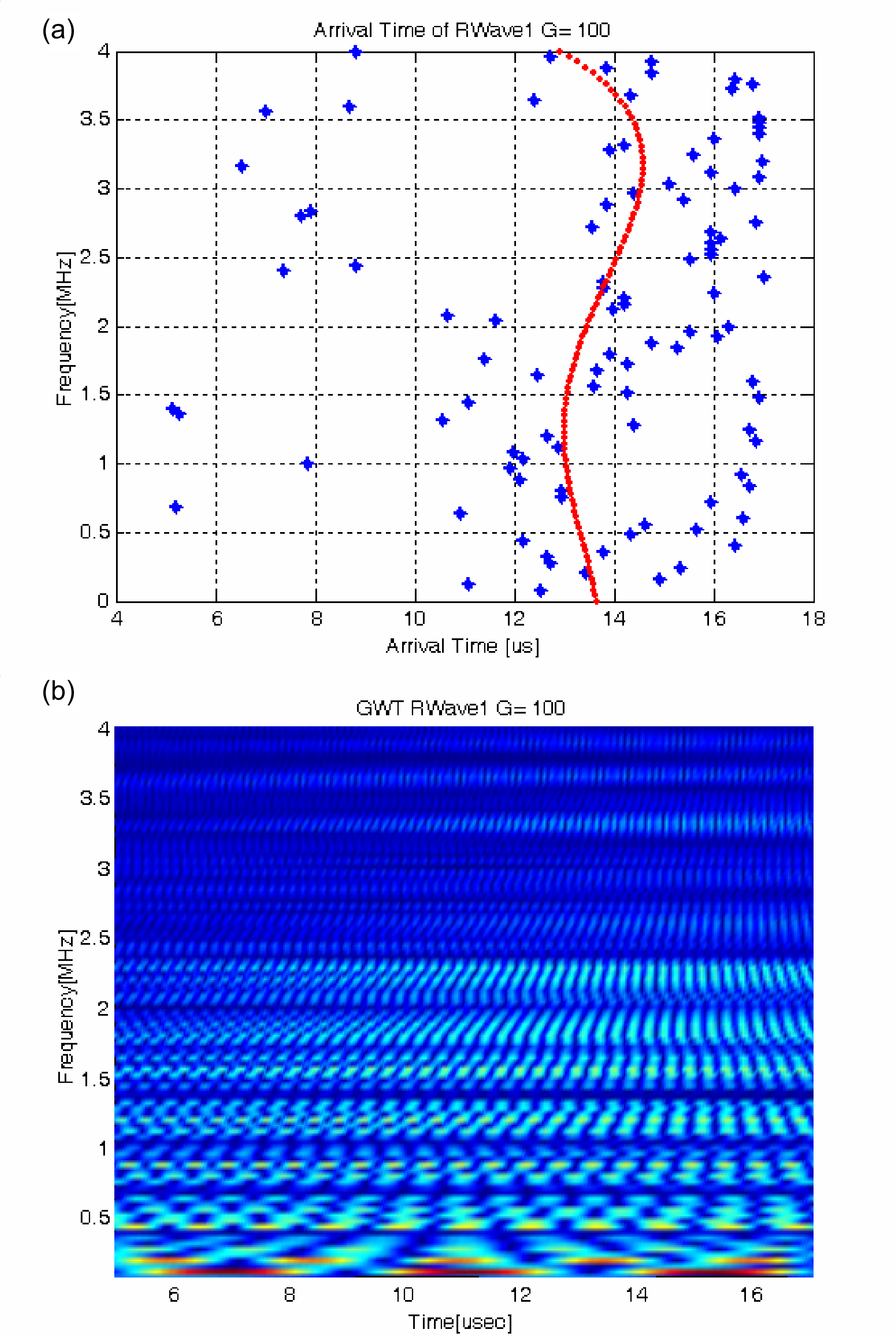

Fig. 3.34—(a) Dispersion curve for a Rayleigh waveform, showing actual arrival times (blue crosses) and fitted time–frequency map (red dots). (b) Corresponding Gabor wavelet with γ =100.

For this case of the actual Rayleigh waveform and in contrast to the Chirp case, when looking at the arrival times of the propagating wave, for different gamma values, figure 3.35, the pattern of "spreading out" data is higher and apparently there is no trend line.

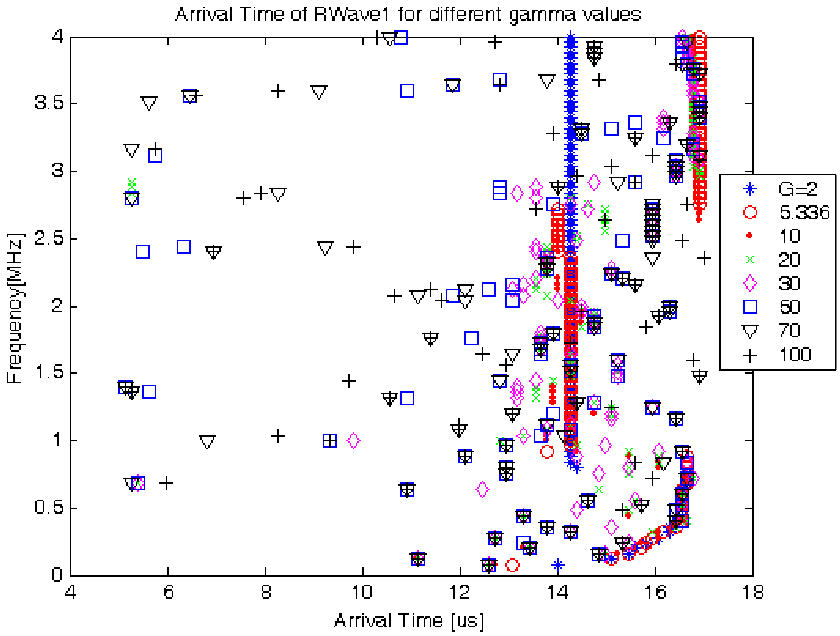

Fig. 3.35--Rayleigh wave arrival times for different gamma values.

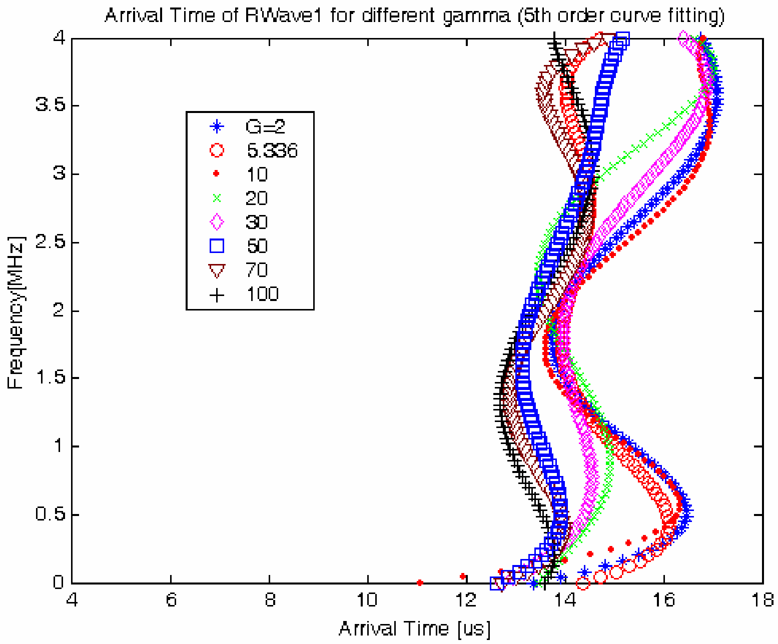

Fig. 3.36—Fitted curves of arrival times for Rayleigh waveform.

However when fitting the data into a 5th order polynomial as shown on figure 3.36, the curves are confined to a more restricted time span between 12 and 17μs, and good convergence around 2 MHz. Again as in the first case, the higher the gamma, the more the data spread and only the curve fitting of data could be useable for estimating the arrival times of the propagating wave on the steel specimen for those higher gamma values, from $\gamma = 30$ and above. This proves that the gamma cannot be arbitrarily increased, because it can decrease considerably the time resolution.

Remembering that Rayleigh waves are non-dispersive, then, in this case, for all the frequency range (0-4MHz), the arrival time should be localized at 14μs according to the given experimental parameters.

It can be shown, also from the plots in figures 2.27-3.34, that is required more time localization (resolution) for low frequencies. This translates into a lower gamma value. Additionally, the plots of Wavelet coefficients in figures 3.27 to 3.34, show that the high frequency contributions are normally weaker than the low frequency contribution in the actual case of the Rayleigh wave. Then it is possible to adapt the gamma value of the Gabor wavelet to get a better time resolution at lower frequencies but compromising frequency resolution, mainly at higher frequencies. For example on figure 3.27,for γ=2, the time localization is excellent for all the frequency range, shown as the vertical line localized at 14μs, but poor frequency resolution is observed. Another example, in figure 3.29 with γ=10 only frequencies between 1 and 2.8MHz are in accordance of the arrival time at around 14μs. Frequencies outside that range (1-2.8MHz) look as if they were arriving later. On the other hand at figure 3.34, with γ=100, there is no clear trend in time domain, and most of the arrival times are off the 14μs vertical line, however there are several frequency bands along the time span. Thus, according to these results, it can be concluded that there is no a prescribed value or datum for γ. That γ value should be chosen according to the specific resolution needed. The γ=5.336 has been usually used in non-stationary dispersive wave situations because it has a good time resolution over a broadband frequency. Lower values of γ can be used if it is required good time resolution at lower frequencies, however a high γ will produce a better frequency resolution, with the corresponding loss in time resolution. For the processing of data in this research there were used two values: $\gamma=5.336$ and $\gamma=10$.

3.6 Summary

Wavelet analysis overcomes the disadvantages of Fourier methods with respect to time-frequency resolution, limited only by the uncertainty principle that establishes that time and frequency cannot be simultaneously localized, meaning that it is not possible to locate a point in a time-frequency map. Thus a localization area, which usually is an ellipsoid, can be located to represent the time-frequency resolution. The smaller the localization area, the better the resolution in a time-frequency map.

The wavelet transform is a very flexible windowing technique, with variable-sized regions, allowing a choice between different available analyzing functions and the use of long time intervals where we want more precise low frequency information, and shorter time regions where we want high frequency information. This becomes a great advantage over other data analysis techniques, because a “suitable” analyzing function or mother wavelet, can be used for a particular application.

In this case for non-stationary signals, the best resolution is obtained with the Gabor wavelet function, because its localization area, in time and frequency domains is smaller than any other analyzing wavelet, providing a better time-frequency resolution. However, care must be taken when using the gamma parameter within the Gabor Wavelet., specifically the “gamma value”. This value cannot be arbitrarily set because it controls the sharpness of the envelop of the Gabor function in time domain. Then it is not possible to get arbitrarily sharp localized Gabor wavelets in time without violating the zero mean condition (3.3) which is characteristic of a wavelet function, because increasing γ arbitrarily will produce a value different of zero at Eq. (3,3).. This results in loss of time resolution.

It can be seen from the figures 3.27 to 3.34 that as gamma is increased, the arrival time points become more scattered. It is easy to recognize a "trend" pattern with respect to time when using gamma values of G=2, 5.336, 10 and 20; not so for higher values. Nevertheless when curve fitting the data, all of them are between certain margins, but still with considerable differences. In addition, it can be seen on figures 3.24 to 3.31 that as the value of gamma becomes higher, more frequency components appear, but compromising time resolution. Then it can be concluded that variation in gamma could result in a variation of arrival times. In order to avoid this, it would be necessary to use different gamma values for each range of frequencies to be analyzed. A quick survey of the different frequencies that can be expected can be carried out by a FFT at different times. Alternatively, it is possible to choose that value according to the type of analysis, which could be for frequency components, in which case a higher value of gamma (γ>30) will be used, or for time localization, in such a case, lower values of gamma (γ<10) should be used. The fact of compromising time or frequency resolution is a typical example of the uncertainty principle, which states that time and frequency can not be simultaneously localized. Probably that is why a kind of "standard" value of gamma=5.336 was used on past studies because this value shows time localization for different frequency components between certain margins.

Time localization is important in order to calculate group velocities. Thus, low gamma values must be used. If on the other hand, frequency components should be identified then high gamma values would be used for that intent.

For this research both parameters, time and frequency are important. When analyzing experimental data of the particular cases studied in this research, two values were employed, γ=5.336 and γ=10, which according to the results of the actual Rayleigh wave, those values provide good time localization between a broadband of frequencies.

CHAPTER IV

EXPERIMENTAL SETUP FOR GENERATION AND DETECTION OF ULTRASONIC WAVES IN CYLINDERS

By using Thermo Acoustic Photonic Non Destructive Evaluation (TAP-NDE)[65,66], in conjunction with Wavelet transform signal processing, it is possible to get the dispersion information with only one detection point. Other techniques need multiple detection points for generation of dispersion curves of ultrasonic waves[67]. Several studies have been performed in order to understand the process of thermal generation of ultrasonic waves[68], mainly in metals[69], and several attempts to generate thermoacoustic waves in a determined direction[70], or a determined propagation mode[71]. Similar techniques based on laser ultrasonics have been used for development of dispersion curves[72], for characterization of subsurface flaws[73], for elastic modulus measurements in thin films[74], and for crack detection in thick annular components[75, 76]. The TAP-NDE Technique and the experimental setup for this purpose will be shown next.

4.1 TAP-NDE Technique

As shown in Figure 4.1, TAP-NDE has three integrated components for data collection

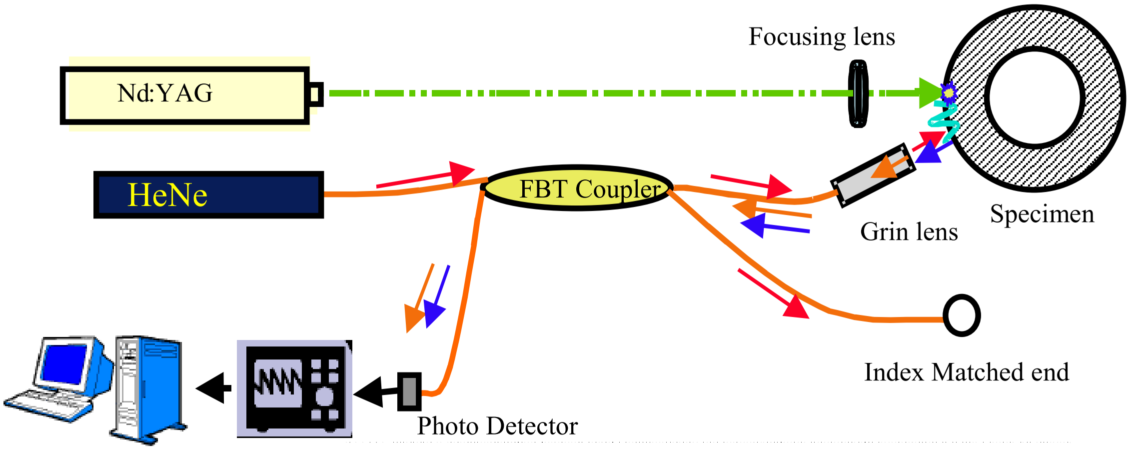

Fig. 4.1--Scheme of the configuration of the TAP-NDE setup used for this study.

and two for acquisition and analysis of data.

1. In the upper part of the figure a pulse from a Nd:YAG laser causes a sharp thermal shock on the surface of a component. This initiates a mechanical pulse (ultrasound) on the surface and also in the bulk of the material being evaluated. As the pulse propagates along the surface of the specimen it interrogates the material for defects and fro changes in properties.

2. The out of plane surface displacements caused by the pulse are detected with a fiber-based interferometric subsystem known as the fiber-tip interferometer (FTI). This is shown in the middle portion of figure 4.1. The FTI is the realization of integrating the concept of a Fizeau interferometer, Fig 4.2, with fiber optics, as in Burger[77], Gilbert[78] and Dudderar[79] into a sensing system for detecting transient surface acoustic waves or pulses. As such, remote generation and sensing is facilitated in a non-contact and non-invasive fashion.

3. The time varying intensity patterns in the output from the fiber-based Fizeau interferometer is registered by a photodetector. This record provides information on the dynamic changes in the length of the Fizeau cavity, as shown in Fig. 4.2.

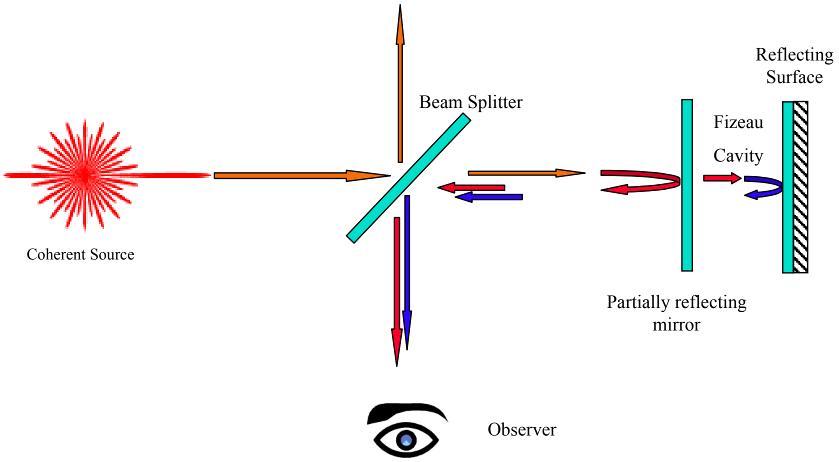

Fig.4.2-- Fizeau Interferometer.

The spot size of the generating beam was controlled by a focusing lens, which allows for variation of the laser energy density input to the material. In doing so, it is ensured that localized heating induces only thermal-elastic responses. Specimens of several geometric configurations including curvatures and thickness were experimentally examined using the described set up. These specimens were designed to get information regarding the wave dispersion as observed on cylindrical surfaces. This subsystem is explained with more detail in a work by Knab[80].

4. Data Acquisition System: The signal from the photodetector is sent to an oscilloscope where the signal was registered. Information extraction and data analysis are then performed on a computer.

5. Finally, the signal is processed by using a Wavelet transform.

The critical part of the Fizeau interferometer is the cavity. This becomes a disadvantage for this setup because the Fizeau cavity must be maintained. In practice this means that the distance between the grin lens and the test specimen must be carefully maintained (constant and perpendicular to the surface). Some other kinds of interferometers are widely used , like the one in Litters, et. al.[81] which is used for experimental verification of distribution of cracks.

Thus the TAP-NDE system can also be separated into a generation subsystem, a detection subsystem and a Signal processing Subsystem as shown in Fig. 4.3.

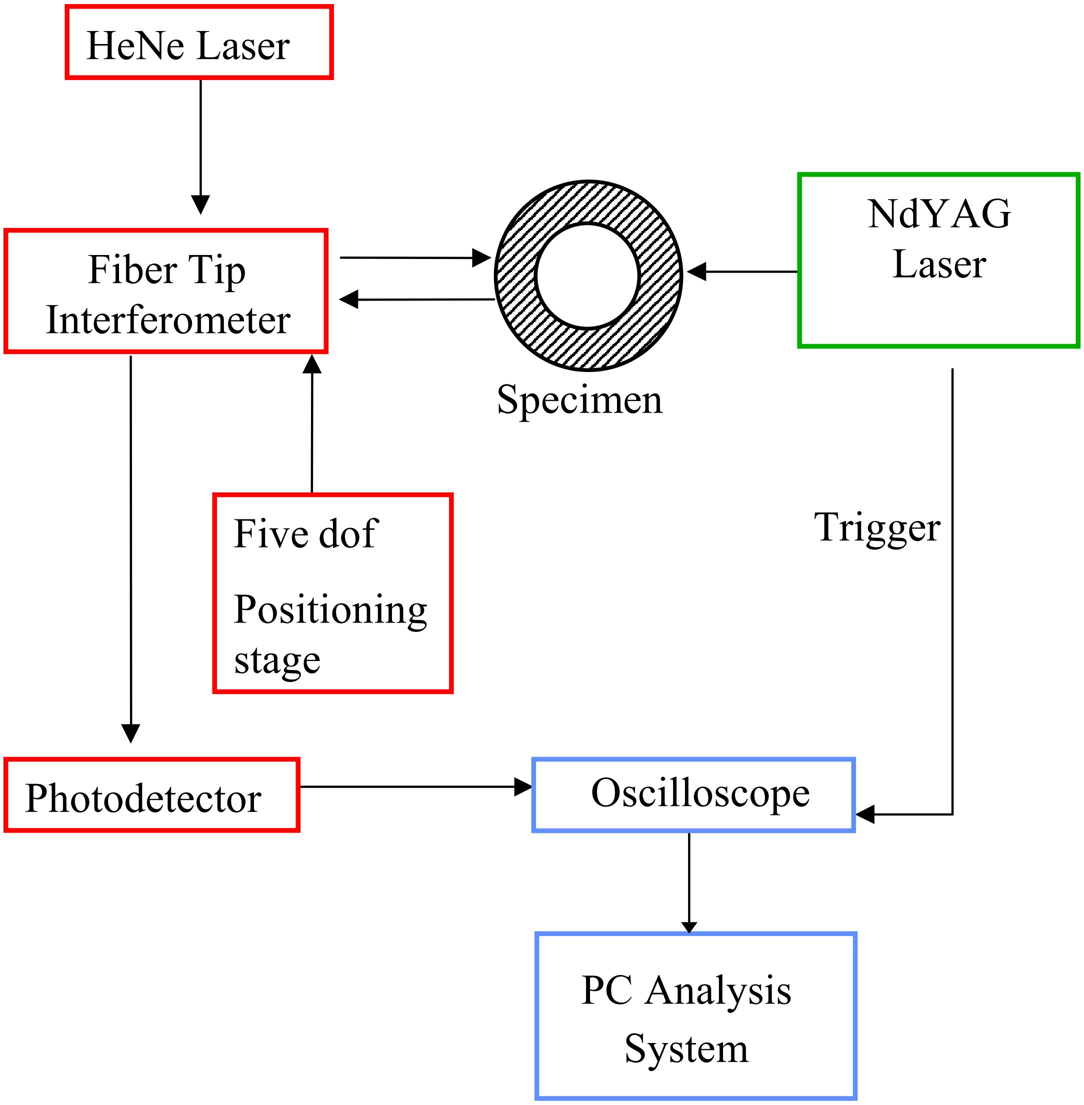

Figure 4.3--Typical TAP-NDE system. Generation subsystem is shown in green, detection subsystem in red and signal processing subsystem in blue.

A two channel version of the TAP-NDE system, shown schematically in Fig. 4.4, is known as a dual FTI system. It was also used in this research.

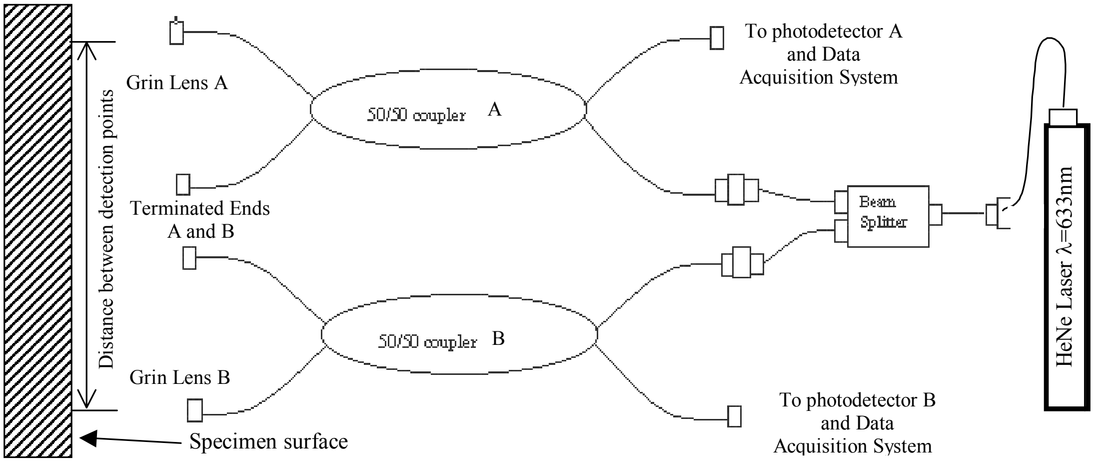

Fig. 4.4--Schematics of a dual FTI system.

A dual FTI system was implemented to get waveforms from the pipe by using an available laser-head collimator (OZ optics[82,83]- HPUC-2,A3A-633-5-6.2 AS-2 65417-1) attached to the 17mW HeNe laser (Research Electro-optics Inc. Model LHRP-1701) through a variable focus fiber cable (OZ optics-SMJ-A3A,3S-633-4/125-3-0.5). In an attempt to obtain a balanced source for both FTI's, the coherent beam from the HeNe laser was split with a FBT coupler (Oz Optics- Fused-12-633-4/125-50/50-3S3S3S-3-0.5). However, because of the large losses at the coupling, it was not possible to set it up. Another configuration using two laser sources was used instead. A second laser-head to fiber coupler, manufactured by the author of this work, was mounted with a five degree of freedom positioner (3 dof Klinger scientific + 2 dof Newport MM2-1A), and attached to the 4mW HeNe (Laboratory for science- "Ultra-stable laser" model 200). A FBT coupler with attached grin lens and collimator (Oz optics- LPC-04-633-4/125-5-1.3-6.2AS-40-1A-3-0.5 and LPC-01-633-4/125-S-0.4-1.81GR-40-1a-3-0.5) was used with this second HeNe laser and integrated into the dual setup for getting waveforms from pipes. The power outputs at the laser-head couplers were measured with a powermeter

(Newport Mod. 840) getting readings of 2.8 and 11.5mW respectively. Although the power input was not balanced for a dual FTI setup, it was equilibrated by using two different FBT couplers (Oz optics - Fused-12-633-4/125-50/50-3S3S3S-3-0.5), which provided different loss rates. The one with less loss was used with the 4mW laser and the coupler with integrated Pigtailed fiber Grin lens and collimator for the FTI 1 closest to the excitation point. The second FTI used the 17mW HeNe laser and a pigtailed grin lens (OZ optics- LPC-01-633-4/125-5-0.4-1.81GR-40-3S-3-0.5). The pigtailed grin lenses were attached by mounting links, manufactured by the author of this work, into five degree positioning stages (Newport 470-1 and MM-10 + CA-2). The FTI's are attached into two silicon amplified photodetectors (Electro Optic Technologies-ET-2030A).

The thermo-acoustic generation was carried out by using a 1.5J/8ns pulsed Nd:YAG laser (Spectra Physics DCR-3) equipped with harmonic generator (Spectra Physics Mod. HG-2). For all tests, the Nd:YAG laser was set up for 60 lamp joules at the oscillator and 60 lamp joules at the amplifier, with a wavelength of 1064nm, the laser's standard wavelength, which according to Knab[84], provides an output of approximately 86mJ/pulse. The beam was Gaussian in nature with a 8mm diameter and was focused onto the specimen by a plano-convex lens with 150mm of focal length (Newport KPX193). To isolate vibrations transmitted by the building, the measurements are performed on an optical table (Newport RS4000).

Finally the waveforms were captured in a 100MHz (200Msa/s) dual channel oscilloscope (HP 54645A[85]) triggered directly by the Q-Switch output of the Nd:YAG laser. The oscilloscope was attached to a PC computer via a GPB interface (HP PCI-HPIB 2078A).

Pictures of the actual dual setup are shown in Fig. 4.5. The focusing lens is marked as No. 1, No. 2 are the positioning stages, 3 and 4 are FTI 1 and FTI 2 respectively and No. 5 is the test specimen. Two fiber optic cables, No. 6 in pictures, are connected to the respective FBT couplers (not shown), which in turn are attached to the photodetectors. The signal is then transformed into voltage and carried from the photodetector into the Data Acquisition system composed by the oscilloscope and a computer.

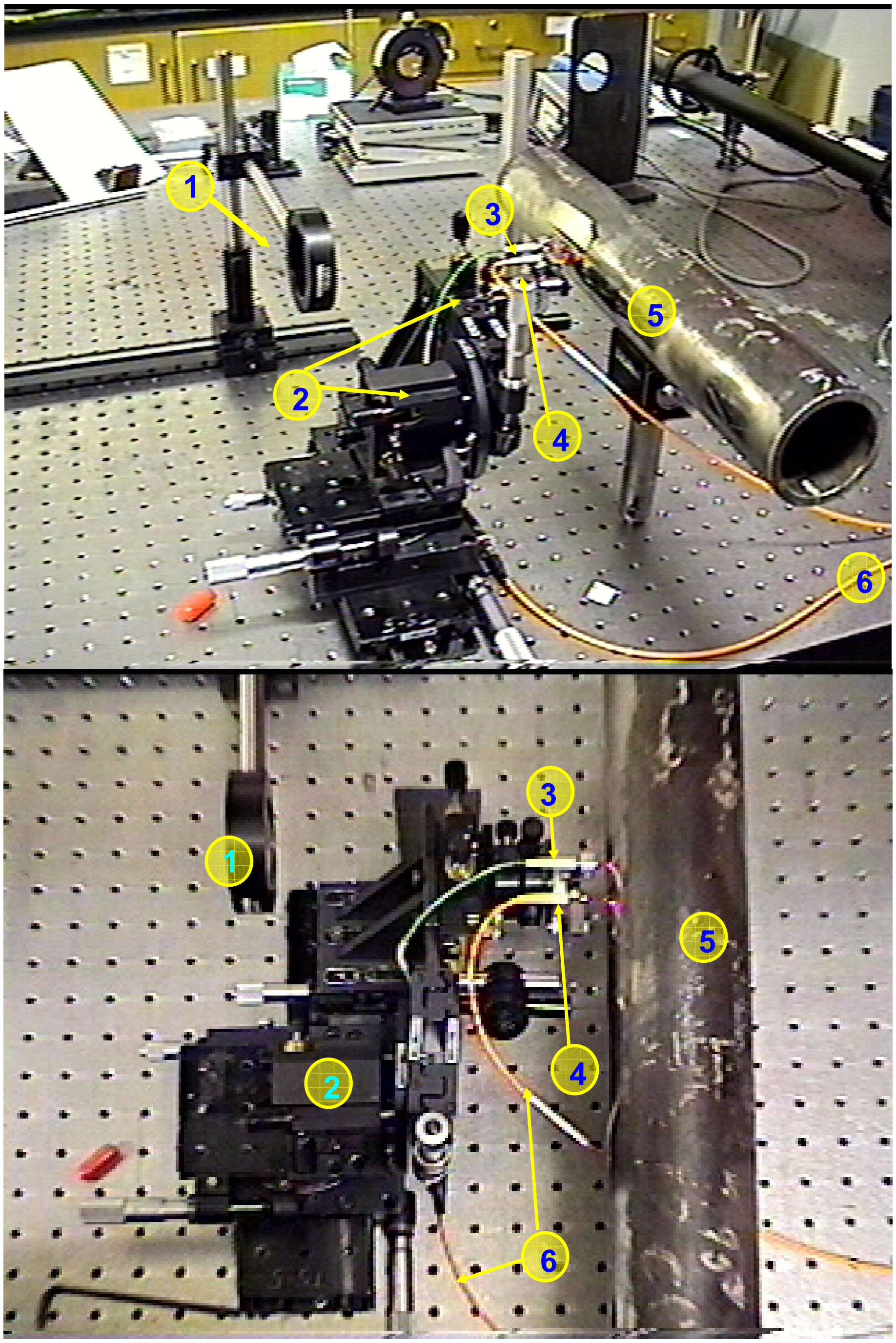

Fig. 4.5--Two views of a dual FTI setup for axial propagation.

4.2 Qualities of TAP-NDE

The advantages of using TAP-NDE are:

In Generation:

1. Point Source Generation that yields the broadband signals.
2. Could be delivered to remote areas by using Fiber optics. As in previous studies by Burger, et al.[86], Duffer[87] and Lanza di Scalea et al.[88] used fiber optics to transmit the laser pulse.
3. Does not require coupling to surface of test. It is thus non-contacting.

In Sensing:

1. High Resolution due to Point Source detection
2. The same pulse can be detected multiple times as it propagates through a material. Thus the same acoustic wave can be detected before and after a defect.
3. Can sense in remote areas.
4. Is thus non-contacting.
5. Is thus non-invasive.

Broadband produces different wave modes, each one having unique physical characteristics and, hence, a different degree of sensitivity to various states of the material.

4.3 Flat Plate Test Configurations

In order to have an experimental background, and to validate the method, several tests were performed on flat plate specimens. This was also useful because it provided a comparison between laser generated broadband ultrasonic waves on flat as well as cylindrical surfaces.

The first plate used was a “thick” steel plate to assure that only Rayleigh waves can propagate at the surface of the specimen. Since the highest Rayleigh wavelength for steel is of approx. 6mm for a 4MHz frequency, which is considered a usable range in this research. A plate thickness of 38mm (6X wavelength) is considered thick enough to ensure Rayleigh wave generation and propagation.

The second tested specimen was a steel plate 7.2mm (0.2835 in) thick, which is the same thickness as the pipe wall. In order to have a direct comparison between a pipe and a flat plate, a groove 400μm deep, 400μm width and 25.4mm long was machined in both, the flat plate and the tube. This was meant to simulate a surface crack (in the plate as well as in the pipe). Laser generated waves were recorded and processed trough the Gabor Wavelet Program described in Chapter III.

4.4 Pipe Test Configurations

Several tests on pipe specimens were done by assuming that the pipes are infinitely long cylinders. This assumption can be established because all measurements are made in the vicinity of the projected centerline on the external wall of the pipe (axially and circumferentially), and far from the ends of the pipe so that reflections from ends arrive well after the signals of interest have been recorded. In order to enable a true non-contact detection with no artificial surface treatments to increase back scattering of light, i.e. reflective paint, or tape, the cylindrical surface of the specimen is sanded and polished, this also provides a consistent surface for guided wave propagation.

The parameters taken into account, as shown on figure 2.8 are:

- Thickness of the pipe wall, h= 7.2mm (0.2835 in)
- Middle radius of the pipe, R= 33.07mm (1.3 in)

Also two frequency ranges are considered for the tests, one for transition-type waves below 200KHz and one for Rayleigh-type waves from 500KHz to 4MHz. Based on this information and the nominal Rayleigh wave velocity c_R= 2950 m/s (9679 ft/s):

- Generated broadband ultrasonic frequency useful range = 500KHz 0 to 4MHz
- Shortest wavelength (at highest frequency) = 0.7mm @4MHz
- Longest wavelength (at lowest frequency) = 5.9mm @500KHz
- The steel properties used are the same that were used for theoretical dispersion curves in Chapter II.

Several configurations (Fig. 4.7) were used to carry out the experiments, some of them used as a reference (with no crack) and some with crack (machined groove simulating a real surface crack, as shown in figure 4.6, along axial and circumferential directions.

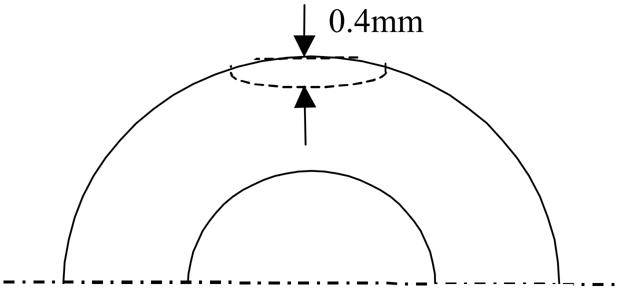

Fig. 4.6—Schematics of the machined groove simulating a crack along circumference of the cylinder.

For all cases:

Distance (a) between excitation point and FTI 1= 10mm

Distance (b) between excitation point and FTI 2= 30mm

Also for cases with crack:

Location of crack at the middle of the two FTI’s at 10mm from each FTI.

Length of crack = 2.54mm (1 in)

Width of Crack = 0.4mm (0.016in)

Depth of crack = 0.4mm (0.016in)

Case 1 : Reference of Propagation along axial direction.

Case 2: Propagation along axial direction with circumferential crack, perpendicular to the propagation direction, between two detection points.

Case 3 : Reference of propagation along circumferential direction.

Case 4: Propagation along circumferential direction with axial crack, perpendicular to the propagation direction, between two detection points.

Note that even though only one detection point is necessary for getting information on each case; a two point redundant detection system has been implemented in order to see the development of the wave propagating before and after the crack.

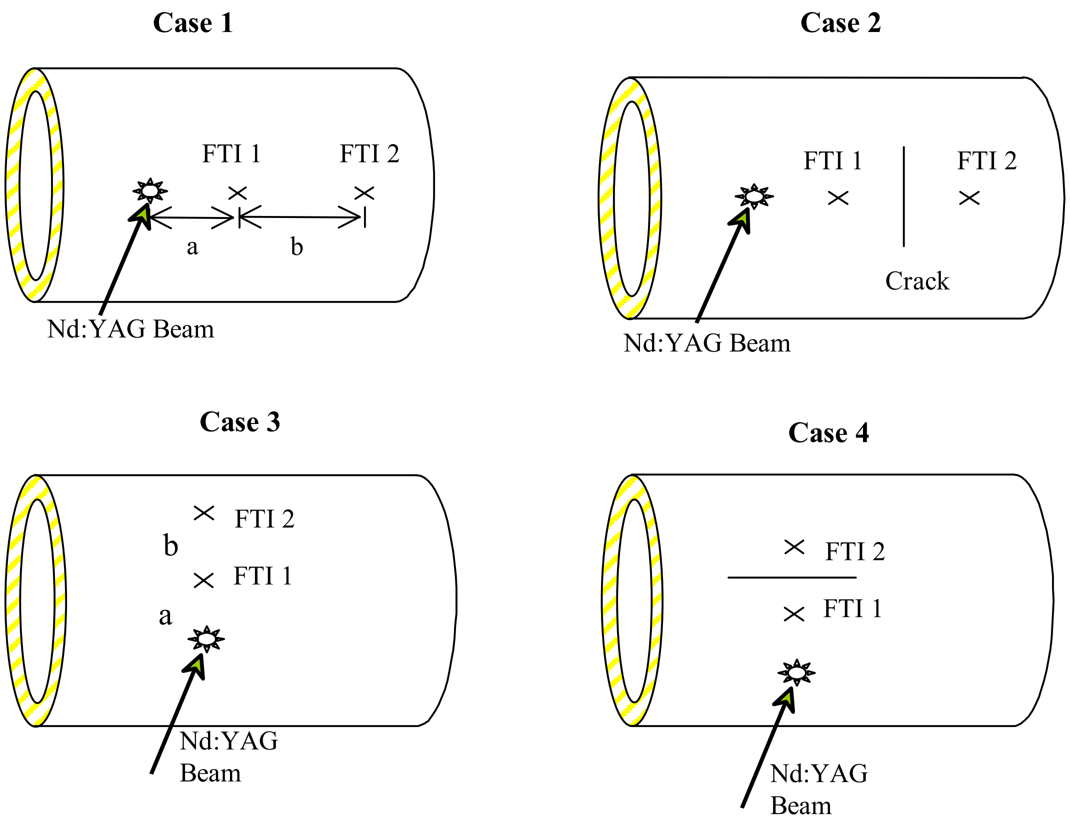
Case 1

Case 2

Case 3

Case 4

Fig. 4.7-- Test configurations on pipe.
Source= The excitation point or point of origin of the pulse.
FTI 1 = 1st. fiber tip interferometer (closest to the source and before the defect.
FTI 2 = 2nd fiber tip interferometer (furthest to the source and after the defect.

CHAPTER V

RESULTS AND DISCUSSIONS

It was necessary to make some adjustments and fine-tuning of the equipment through preliminary tests before obtaining acceptable waveforms, and, in order to validate the method.

The obtained waveforms were noisy and more research was done also to investigate if it was possible to reduce noise on the signal without affecting the usable range of frequencies, this issue will be addressed later on this chapter.

5.1 Thermoacoustic generated waves

Several doubts arose regarding the wave velocities of around 400m/s that were obtained. These velocities were not in accordance to Rayleigh wave velocities of around 2900m/s[89]. New work was necessary in order to find the problem in the experiment. The investigative process carried out to accomplish this was as follows.

1. Registry of all settings/variables in oscilloscope that were used on experiments.

2. Calibration of the oscilloscope by checking up all settings and variables. Several tests were performed changing one setting at a time by using a signal/wave generator. After these, the Oscilloscope could be considered working fine

3. Check up of FTI system, using also the wave generator and a piezo-electric positioner in order to verify the sensitivity of the detection system.

4. Check up of YAG laser, alignment, beam profile, spot diameter = 1mm, pulse duration = 13ns and variable Q-switch setting =8.5 for most efficient output (highest detected amplitude of the waveform). It was not possible to obtain a clean Gaussian profile, and this could be an additional source of noise. Nevertheless it can be discriminated and cleared with the Wavelet signal processing without altering the useful information.

5. After check up of generation, detection and data acquisition systems, a Re-taking of waveforms from a thick flat plate (38mm thick).Variation of one setting at a time was performed. Still Waveforms with speed of around 400 m/s were obtained.

6. Tried to detect Rayleigh waves generated with contact transducer mounted on a plastic wedge. FTI was not able to capture that signal. Reviewed past theses by Smith[90] and by Peters[91] in which this setup was used. They were able to capture Rayleigh waves but they used the Argon laser instead of the HeNe at the detection stage. I am assuming at this point, that because the higher intensity of the Argon laser, it was possible to have higher contrast and then easier to capture the waveforms.

7. Check up of the threshold level at the trigger input of the oscilloscope. In order to capture the signal, the oscilloscope is coupled to the Nd:YAG laser trough a trigger line. The Q-switch of YAG laser triggers at 7.5V, so the trigger level setting at the oscilloscope could be any voltage below 7.5V, however below 800mV a noise-triggering situation was observed. Then setting the level between 0.8V and 7.5V would work for triggering. A value of 3.5V for that particular setting was proved to be okay.

8. Regarding Laser-generated ultrasound, and according to Scruby and Drain[92], the circular spot of the YAG laser beam generates S-wave and P-wave dominated

ultrasound, and, in order to get a surface wave it is necessary to use a sacrificial layer. This layer could be a liquid, a gel or even a layer of paint, which allows for more energy absorption, especially when the surface of the specimen is smooth. Aindow[93] et al. and Hutchins et al.[69] also recommend use of a thin film of oil as a sacrificial layer. This is because great part of the energy is reflected back from the surface and just a small portion is absorbed and then transformed into thermal stress. In this case, the surface has been polished in order to have a good reflective surface for the FTI. Also the wave amplitudes are proportional to the incident energy in the laser pulse.

9. With this information at hand, proceeded to use a sacrificial layer at the generation point and to increase the energy by using the amplifier of the Nd:YAG laser. I used first a sacrificial layer of paint but it was burst and no wave was captured other than the ones that previously were shown. A second attempt was made using the sticky shear wave couplant as a sacrificial layer. Finally a Rayleigh wave, figure 5.1, with wave speed of 2978 m/s was seen by FTI 1, but this was too small in comparison of the other recorded waves arriving later.

10. P-wave couplant gel was used as a third material for sacrificial layer and a considerable increase in amplitude was registered for a Rayleigh wave but still only at FTI 1. Scruby and Drain[92] also recommend to use a cylindrical lens to focus the laser beam into a line source instead of a point for generating and amplifying Raleigh waves, by doing so, the number of excited modes is reduced because the generation process approaches to a narrow-band process limiting the usefulness of the dispersion approach. So, this will not be done in this research.

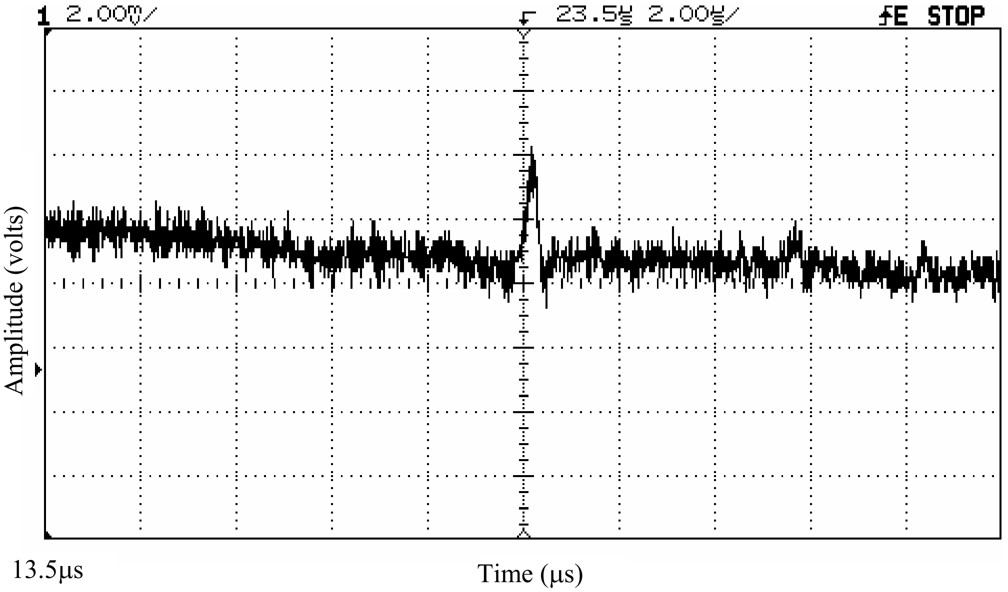

Fig. 5.1---Oscilloscope display showing a Rayleigh wave detected at channel 1 (FTI 1). Distance from source, ℓ =70mm, time after pulse t= 23.5µs. The calculated Rayleigh wave velocity for this arrival time was V_R=2978 m/s. At time zero (not shown) is the laser pulse. The parameters of the captured screen are as follow: the upper left No. 1 meaning that Channel 1 is being displayed, Amplitude scale = 2mV/division, time scale= 2µs/division, starts at 13.5µs at the left, it is centered around the arrival of the detected waveform at t= 23.5µs after the pulse, at the upper right the E means external triggering and the word STOP meaning that the measurement has been stopped and no test is currently running.

5.2 Preliminary tests

Regarding the "apparent" slower waves that were detected, several tests were carried out on flat thin and thick specimens, and invariably slower velocities than Rayleigh Wave velocity were obtained. We then proceeded to isolate (with a blocking paper shade) the generating beam from the FTI, and then realized that the waveform was diminished at both FTIs. Suspected then that what the FTI was "seeing" was an apparent interference between the generating beam striking the surface and forming plasma, and the FTIs. In this research, for steel pipe the energy used is high in order to produce ultrasonic waves. So there is a possibility to produce plasma and shock air waves. Another shade made of rubber, that completely blocks the FTIs from the generation point were used and my suspicion was confirmed, no waveform was detected. This phenomenon is explained by

Villagran-Muñiz et.al.[94] as shock wave and the thermal expansion of the hot air in the core of the decaying plasma formed by the laser focused into a point (a.k.a Laser-induced breakdown). The velocities of those shock waves being between 40 m/s and 528 m/s and arrival times going from micro seconds to milliseconds, depending on distances and atmospheric conditions. These waves affect directly the interference beams of the FTIs by refracting them. In the same article, a recommendation is made to avoid detection of laser scattered light *(*1.06 μm*)* and plasma into the photosensor, isolating them by the use of an interference filter.

Additionally, the intensity of the FTI 1 was of the order of five times greater than that of the FTI 2, due to the lower power (3.5mW) of the HeNe laser used at FTI 2, compared to the 17mW HeNe used for FTI 1. This contributes also to the fact that the Rayleigh wave could be seen only at FTI 1, but still with relative low amplitude. From all these I can say that the HeNe intensity used for the FTI is a significant issue in order to detect Rayleigh waves. That is why, in order to balance it, a second coupler, along with a beam splitter was tried for both FTIs working with the 17mW HeNe laser.

Regarding the noisy signals that were obtained, some tests were carried out to check the significance of this noise in the process of extracting information from the wavelet coefficients. As mentioned in Chapter III, the useful range of frequencies (range of dominant frequencies) of a Rayleigh-type signal, is below 4 MHz. Higher frequencies than 4MHz could be due to noise. One way of de-noise a signal is using the wavelets packet of the Matlab program, in this case to filter out high frequency noises. Figure 5.2, shows a laser-generated Rayleigh wave signal obtained experimentally.And figure 5.3 Shows the de-noised Rayleigh wave signal corresponding to the original signal in figure 5.2. The denoising is carried out by using a feature of one-dimensional wavelet packet analysis using the MATLAB Wavelet Toolbox. The Wavelet Toolbox provides these functions for wavelet packet analysis. The wavelet packet de-noising procedure involves thresholding of wavelet coefficients.

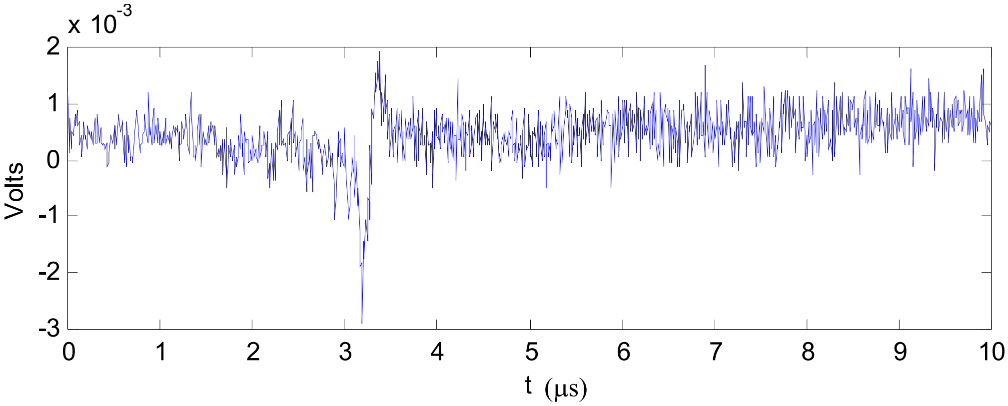

Fig. 5.2---Rayleigh wave obtained from a flat thick steel plate. Thickness of the plate h=38mm, propagation distance ℓ =10mm, Spot diameter d_s=10mm. The arrival time after pulse is t= 3.3μs. The calculated Rayleigh wave velocity for this arrival time was V_R=3030 m/s.

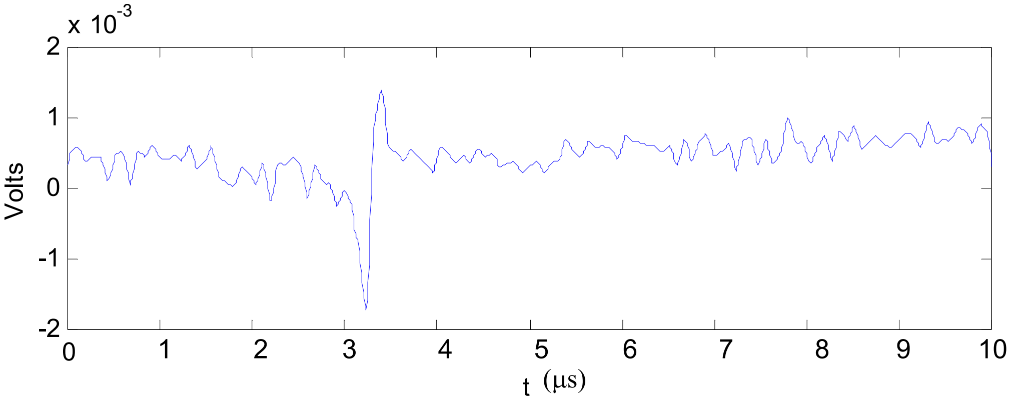

Fig. 5.3--- De-noised signal of the Rayleigh wave from figure 5.2. The de-noising is carried out by using wavelet packets from the Matlab® program. Note that, as expected, because the de-noising, the amplitude of the dipole is reduced.

In order to verify that effectively the noise is filtered out from the signal without altering the useful data, a full-frequency range (0 to 50MHz) wavelet transform analysis was carried out on the Rayleigh wave (before de-noising) from figure 5.2. The corresponding wavelets coefficients plot was obtained and it is shown in figure 5.4. Here , the arrival time after pulse is shown at the plot as a concentration of maxima coefficients around 3.3μs which expands in two frequency bands from 0 to 8MHz and then from 12MHz to approx. 15MHz. There is also a high frequency component at around 40Mhz.

Then the Rayleigh wave signal from figure 5.3 (after de-noising) was analyzed by wavelet transform and a very noticeable difference with respect to the noisy signal was obtained as shown in figure 5.5. Here, the arrival time after pulse is t= 3.3μs, which is shown at the plot as a concentration of maxima coefficients around 3.3μs which expands in a frequency band from 0 to approx 20MHz.. Additionally, when comparing this plot to the one in figure 5.4 (before de-noising), it can be shown that the high frequency component at around 40Mhz has been disregarded by the de-noising process. Nevertheless frequency components below 10MHz are present, and they would be enough for analysis within the selected useful range of 4MHz

This important clearance of higher frequencies was achieved as a result of the de-noising process previously explained and does not alter the considered useful range below 4 MHz, as defined in Chapter III.

Note that, as explained in Chapter III, the higher the frequency, the better time resolution, and vice versa, at low frequencies, the time resolution is bad. If a better time localization is needed, then the γ should be reduced, but doing so, will result in a decrease in frequency resolution

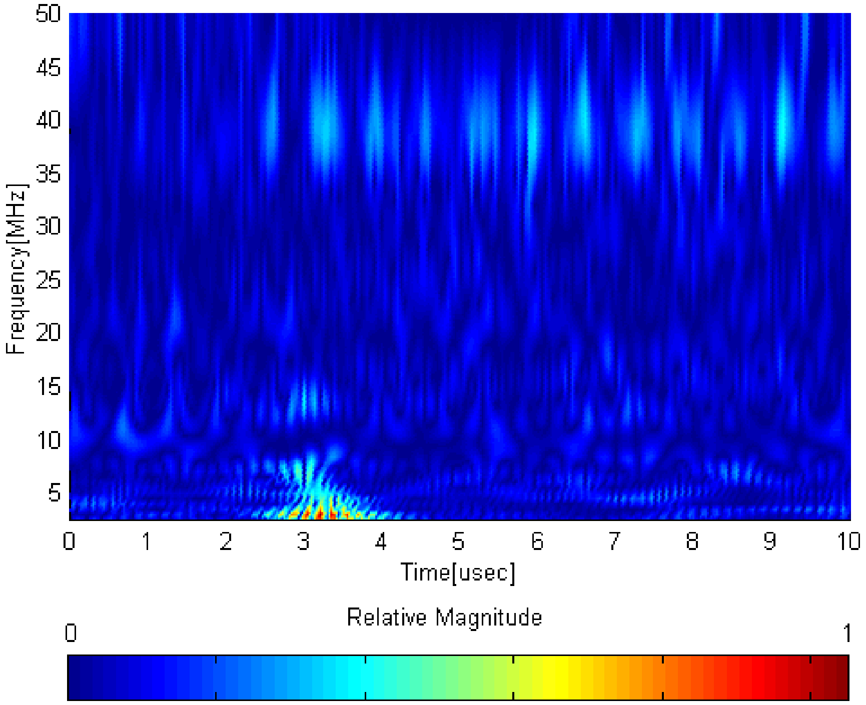

Fig. 5.4--- Gabor Wavelet transform plot for the Rayleigh wave signal from figure 5.2 (before de-noising), is showing the Max. resolvable frequency of 50MHz. The magnitude is represented by a color bar scale, which, goes from zero magnitude in dark blue to a maximum value in red. A γ = 5.336 was used. The specimen was a thick flat steel plate, h=38mm, propagation distance from the source ℓ=10mm, spot diameter d_s=10mm. The arrival time after pulse is t= 3.3μs, which is shown at the plot as a quasi-symmetric concentration of maxima coefficients around 3.3μs which expands in two frequency bands from 0 to 8MHz and then from 12MHz to approx. 15MHz. There is also a high frequency component at around 40Mhz. As explained in chapter III, if a better time localization is needed, then theγ should be reduced, but doing so, will result in a decrease in frequency resolution.

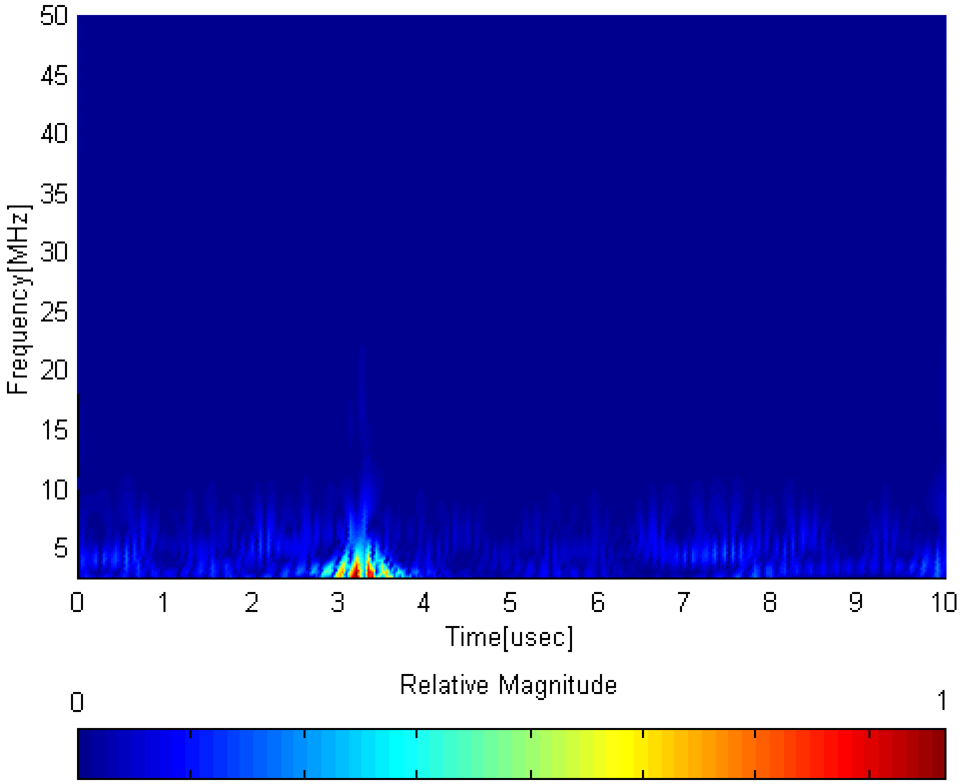

Fig. 5.5--- Gabor wavelet transform plot for the Rayleigh wave signal from figure 5.3 (after de-noising), showing the max. resolvable frequency of 50MHz. The magnitude is represented by a color bar scale which goes from zero magnitude in dark blue to a maximum value in red. A γ=5.336 was used. The specimen was a thick flat steel plate, h=38mm, propagation distance from the source ℓ=10mm, spot diameter d_s=10mm. The arrival time after pulse is t= 3.3μs, which is shown at the plot as a quasi-symmetric concentration of maxima coefficients around 3.3μs which expands in a frequency band from 0 to approx 20MHz. Note that, as explained in Chapter III, the higher the frequency, the better time resolution, and vice versa, at low frequencies, the time resolution is bad. If a better time localization is needed, then the γ should be reduced, but doing so, will result in a decrease in frequency resolution. Additionally, when comparing this plot to the previous one (before de-noising), it can be shown that the high frequency component at around 40Mhz has been disregarded by the de-noising process. Nevertheless frequency components below 10MHz are present, and they would be enough for analysis within the selected useful range of 4MHz

The fact that there is no significant difference within the useful range of frequencies (below 4MHz) can be corroborated when looking at the plots in figure 5.6 where amplified views of corresponding to figures 5.4 and 5.5, with a frequency range from 0 to 10 MHz are presented. Figure 5.6 (a) shows an arrival time after pulse of t= 3.3μs, which is shown at the plot as a concentration of maxima coefficients around 3.3μs which expands in a frequency band from 0 to 5MHz. There is another pulse arriving at 3μs and it is located at a frequency band from 6MHz to approx. 8.5MHz. This could be the shear wave arrival. Again a better time resolution is shown at higher frequencies and if a better time localization is needed at low frequencies, then the γ should be reduced, but doing so, will result in a decrease in frequency resolution There are also some low magnitude components all over the frequency-map. Additionally, at the lower right corner of the time-frequency map is observed an edge effect, which was explained in Chapter III. Figure 5.6(b) shows the arrival time after the pulse as a concentration of maxima coefficients around 3.3μs, which expands all over the frequency band from up to 10MHz with higher magnitude at lower frequencies. Again a better time resolution is shown at higher frequencies. Note that when comparing this plot with the one in figure 5.6(a), before de-noise, some of the higher frequencies have been disregarded by the de-noising process. Also an edge effect is observed at the lower right corner of the time-frequency map.

As shown in figures 5.4, 5.5 and 5.6, the assumed useable frequency range below 4 MHz, can be increased up to 5 MHz because there is not significant difference of the resulting wavelet coefficients before and after de-noising within this range when applying the Gabor Wavelet Transform (GWT). It is noticed that only higher frequencies are cleared out. This also was proved when plotting and comparing the Gabor Wavelet transforms of the new useable range (0 to 5 MHz) for both cases in which no significant difference was found.

(a) Rayleigh wave signal before de-noising

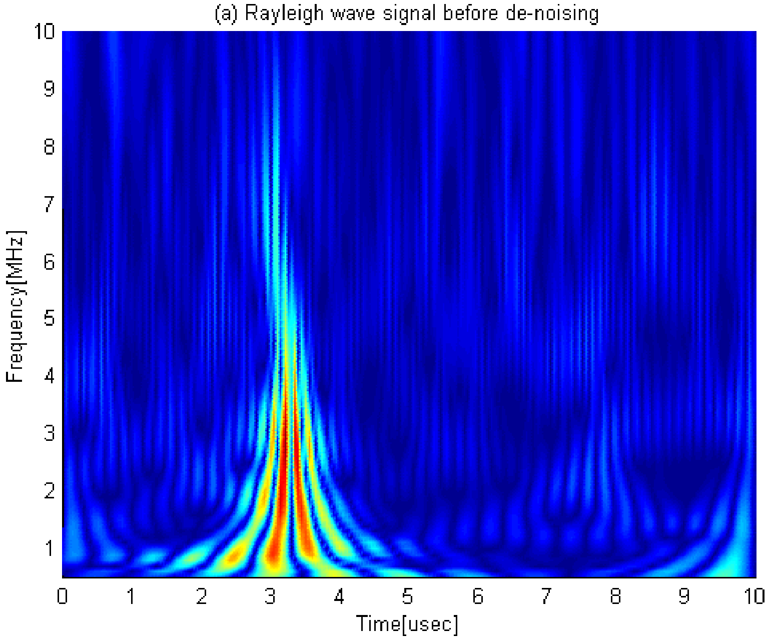

(b) Rayleigh wave signal after de-noising

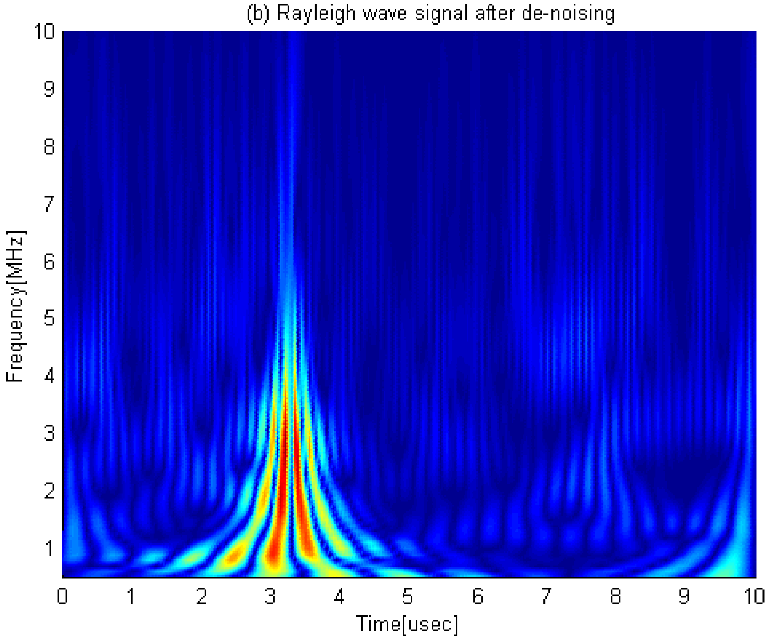

Fig. 5.6--- Gabor wavelet transform plots showing a frequency band of 0-10MHz.
(a) for the Rayleigh wave signal from figure 5.2 (before de-noising),.and
(b) for the Rayleigh wave signal from figure 5.3 (after de-noising).
The magnitude is represented by the color bar scale shown in figures 5.4 and 5.5 and goes from zero magnitude in dark blue to a maximum value in red. A γ=5.336 was used in the Gabor wavelet code. The specimen was a thick flat steel plate, h=38mm, propagation distance from the source ℓ =10mm, spot diameter d_s=1mm.

It was found that when the Rayleigh wave signal from fig. 5.2 is analyzed within the 5MHz range, the differences in the wavelet transform coefficients before and after de-noising, (figure 5.6) are practically nil. This proves that wavelet transform, under certain conditions can be insensitive to noisy signals. This simplifies the possibility of being able to extract all the useful information of the signal. The only difference when analyzing was the execution time of the program. As expected, the de-noised analysis takes more time to compute. From here, it was used the original noisy signal for analysis. Then it can be concluded that for a useable frequency range up to 5MHz there is no difference if the signal is de-noised or not by using the method mentioned above before being processed into the Gabor Wavelet Transform

A second set of tests of laser generated waves was carried out on a flat steel plate with the same thickness as the pipe wall specimen, h=7.2mm. The propagation distance from the source was ℓ=45mm, spot diameter d_s=1mm. Plots of the waveform, before and after de-noising as well as Gabor wavelet transform are shown on figure 5.7.

When the signal is analyzed trough wavelet transform, the time-frequency map obtained before and after de-noising would be practically the same. However it is included in figure 5.7(b) the de-noised signal because it allows visualizing details on the waveform, which otherwise would be difficult to see at the noisy signal.

In the wavelet transform plot on figure 5.7(c) there is a Rayleigh wave characteristic represented as an arrival time at around 16μs extending on a frequency band up to approximately 1.6MHz. At lower frequencies, however there is a dominant Lamb wave characteristic. In order to confirm such transition wave behavior, two amplifications are made from the original Wavelet plot from figure 5.7(c), and are shown on figure 5.8.

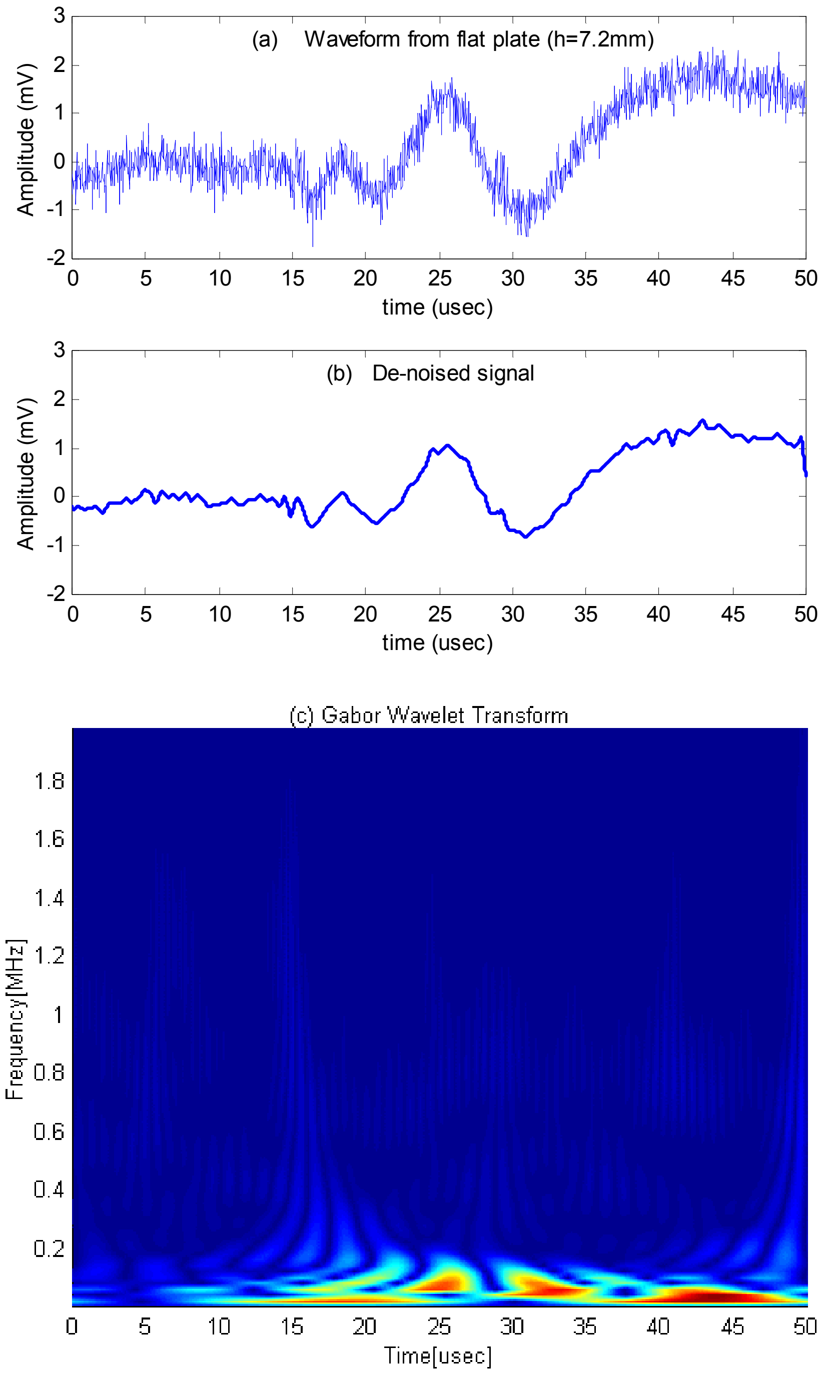

Fig. 5.7---Waveform obtained from laser generated waves on a flat steel plate with thickness h=7.2mm (same as the pipe wall specimen). (a) Before de-noising, (b) After de-noising and (c) corresponding wavelet transform. The propagation distance from the source was ℓ=45mm, spot diameter d_s=1mm. Note that when the signal is analyzed trough wavelet transform, the time-frequency map obtained before and after de-noising is practically the same. However the de-noised signal allows visualizing details on the waveform, which otherwise would be difficult to see at the noisy signal.

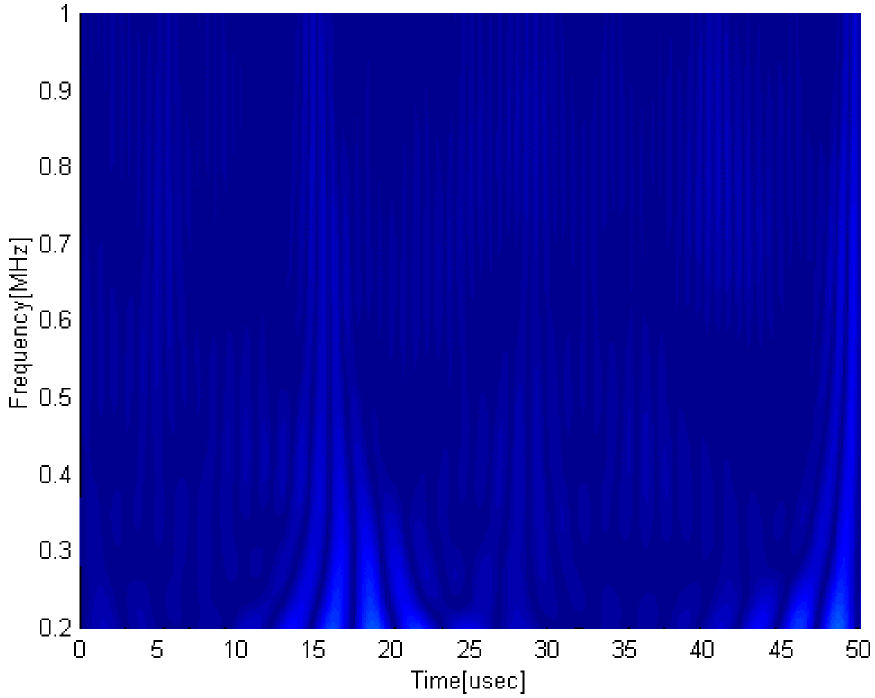

(a) surface wave behavior at relative High Frequencies

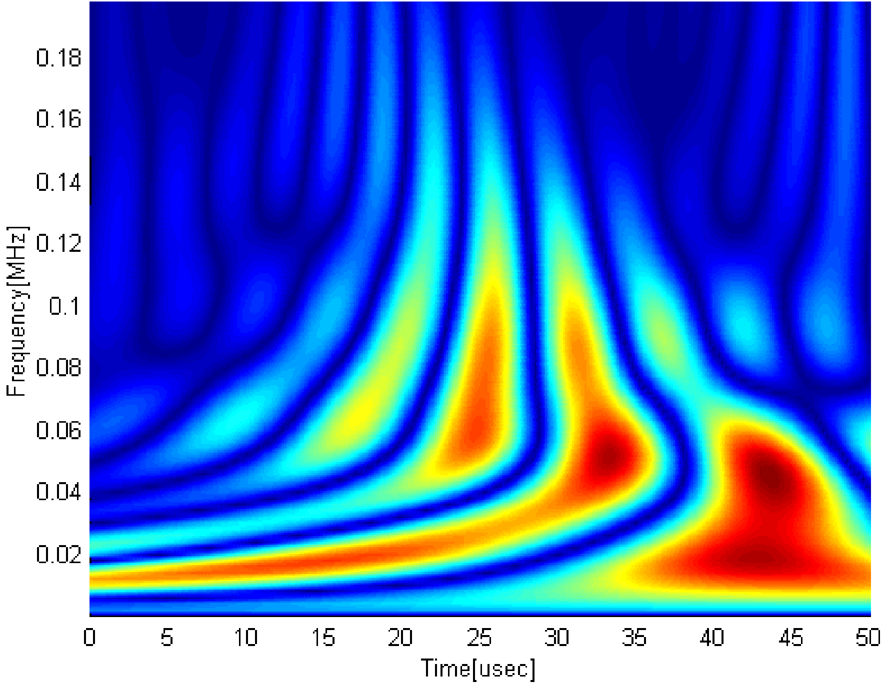

(b) Plate wave behavior at relative low frequencies

Fig. 5.8--- Gabor wavelet transform plots corresponding to the signal on figure 5.7(a) showing the transition behavior. (a) Surface wave characteristic at relative high frequencies, above 200KHz and (b) Plate wave characteristic at relative low frequencies, below 200KHz. The magnitude is represented by the color bar scale shown in figures 5.3 and 5.4 and goes from zero magnitude in dark blue to a maximum value in red. A γ = 5.336 was used in the Gabor wavelet code. The specimen was a flat steel plate, h=7.2mm, propagation distance from the source ℓ =45mm.

Figure 5.8 shows the Gabor Wavelet transform plots corresponding to the signal on figure 5.7 split into two in order to illustrate the transition behavior.

In Fig.5.8(a), above 200KHz, it is evident the surface wave characteristic at relative high frequencies. The Rayleigh-type trace in the plot is shown as a quasi-symmetric concentration of maxima coefficients located at around 16μs and extends in a frequency band all the way up to 1 MHz. Note that the scale of magnitude was maintained with respect to fig. 5.7(c) after amplification. Thus, there was no normalization with respect to a maximum. In addition it can be noticed that the lower the frequency, the worse time localization, and vice-versa, as seen on the previous example of the Rayleigh wave on a thick plate on Fig. 5.6. There are several low magnitude traces on the frequency-map plot and a second apparent pulse arriving at the end of the signal of the same order of magnitude of the Rayleigh trace, this could be due to the edge effect discussed on Chapter III.

In Fig. 5.8(b) the plate wave characteristic at relative low frequencies, below 200KHz is illustrated. The magnitude is represented as before, by the color bar scale shown in figures 5.3 and 5.4 and goes from zero magnitude in dark blue to a maximum value in red. The scale of magnitude was maintained with respect to fig. 5.7(c) after amplification. A $\gamma = 5.336$ was used in the Gabor Wavelet code. The specimen was a flat steel plate, h=7.2mm, propagation distance from the source ℓ=45mm. Note that there are several dominant frequency traces shown as colored bands. Each of these bands have a maximum value, which ultimately represents the arrival time of a pulse. Then it can be visualized up to six different arriving pulses as follows: At 43μs with a frequency of 100KHz, at 44μs with a 400KHz frequency, at 34μs with a 450KHz, at 25μs with a frequency of 570KHz, at 17μs with 600 KHz and at 9μs with 600KHz. From those bands it can be recognized the longitudinal wave component at 9μs, c_l=45mm/9μs = 5000m/s. The second recognizable trace is at 17μs, an approximate Rayleigh wave speed c_R = 45mm/a7μs = 2650m/s. the rest of the races contain velocities from 1000-1800m/s, which can be considered in a Lamb-transition wave zone. According to the band traces of the plot, each localized maximum is just a portion of one propagating mode assuming that there are several propagating modes. Thus the trend line formed by a sequence of those localization of maxima does not necessary represent one specific mode.

It can be concluded that for a particular plate thickness, h=7.2mm, the waves that were obtained were Rayleigh waves and transition-Lamb waves which are not completely Rayleigh-type waves nor completely Lamb-type waves, with characteristics that lie between those of surface waves and of plate waves.

5.3 Validation With Theory

Mirsky-Herrmann theory in its transformed form can be used to validate the experimental results here obtained for a steel pipe specimen with wall thickness is 7.2mm, and a middle Radius R= 33mm and four possible cases as explained in Chapter IV and as detailed in figure 4.7. The validation can be carried out thanks to the fact that the Gabor wavelet coefficients and the transformed M-H plots (figures 2.11-2.14) are in the same time-frequency domains. Then the comparison can be direct because arrival times maxima in Gabor wavelets are corresponding to specific modes in dispersion curves of M-H theory. This can be shown in figures 5.9 to 5.12, with comparisons of theoretical and experimental dispersion curves corresponding to the geometry of the actual pipe, R=33.2mm, h=7.2mm, whose dimensions corresponds to cylinder which is not thin ($m \leq 1/10$), nor thick ($m \geq 7/10$), as explained on section 2.4 of Chapter II, but somewhere between (m=h/R= 7.2/33=0.218) and then the wave phenomena will be a wave propagation in transition behavior.

Figures 5.9 and 5.10 compares the theoretical and experimental dispersion curves for Axisymmetric motion as studied in the M-H theory on section 2.4 in Chapter II, and an experimentally obtained Axial wave propagation. In figure 5.9 the first three modes of the transformed Mirsky-Herrmann dispersion curves are shown. While 5.10, shows the experimental Gabor Wavelet plot for the same conditions. There is a fair correspondence between the trend and shape of the theoretical values of figure 5.9 and the actual experimental results shown in figure 5.10, with an exception of the second mode S_2 in figure 5.10 at low frequencies below 50KHz, which present a kind of weak coupling with the other modes, and does not agrees with the non-dispersive situation shown on mode S_2 of figure 5.9. This is because the theory assumes pure axial propagation. Experimentally, this was not the case because the excitation point was on the outer face of the pipe. Then the propagation is not purely axial. Mode S_2 arrives at 16.2μs all over the frequency band. The corresponding Rayleigh wave velocity calculated for mode S_2 is: C_R=50mm/16.2μs=3090m/s. Mode S_1 is identified from both plots with a cut-off frequency converging to a value near zero and a third mode S_3 with a cut-off frequency of approx. 35KHz.

In Fig. 5.10, the mode S_1 predominates, indicated by the much higher wavelet coefficients. Here the magnitude of the wavelet coefficients are in accordance to the color bar scale from previous wavelet transform plots (i. e. Figs. 5.3 and 5.4) which increases from dark blue thru yellow to red. Figure 5.9 gives no indication of the relative magnitudes of the modes at different location along the three graphs. This is because the M-H dispersion curves are two-dimensional.

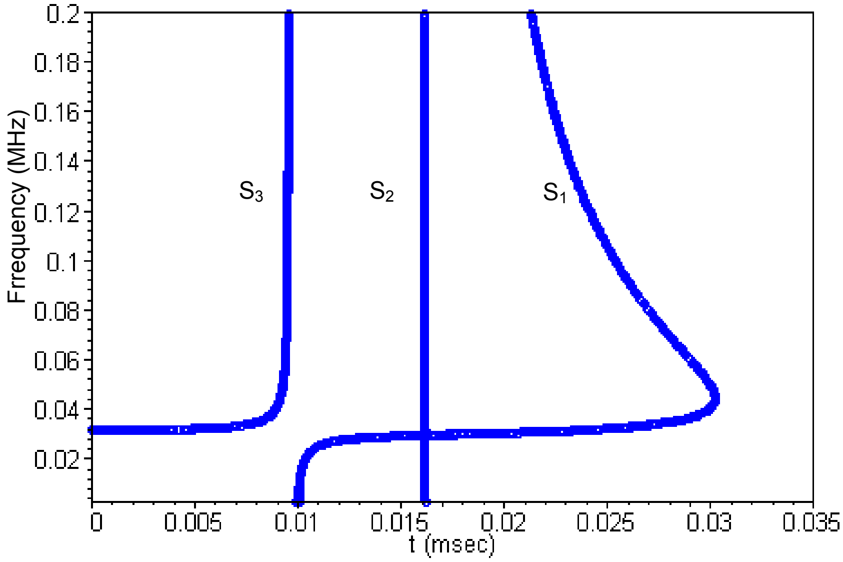

Figure 5.9-- Transformed Mirsky-Herrmann dispersion curves for axisymmetric wave motion (n=0). Steel pipe specimen with h=7.2mm, R=33.2mm, propagation distance = 50mm. Mode S_1 is the first flexural mode, mode S_2 is the first torsional mode which is non-dispersive for n=0 and arrives at 16.2μs. The mode S_3 is the second flexural mode and has a cutoff frequency at 35 KHz.

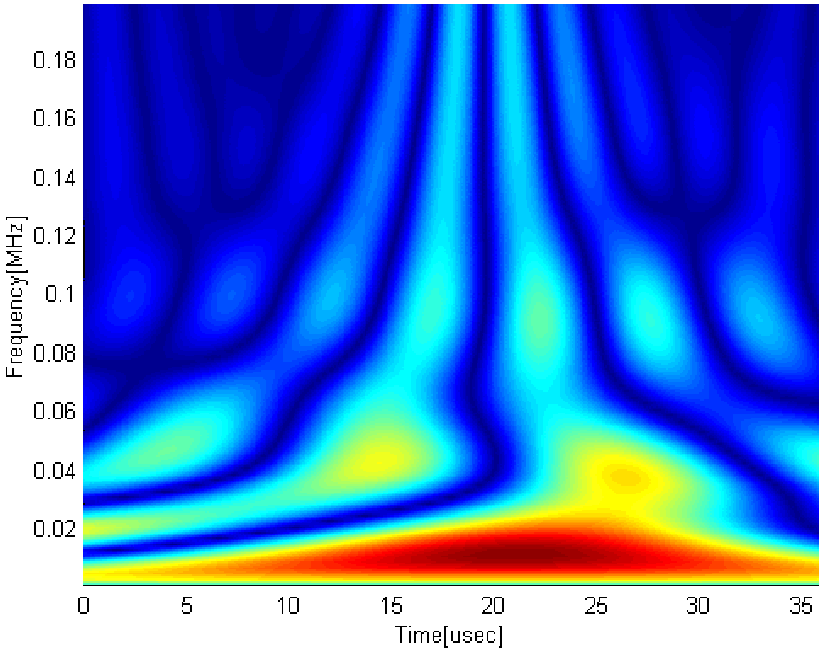

Figure 5.10--- Gabor wavelet transform for axial propagation direction. Steel pipe specimen with h=7.2mm, R=33.2mm, propagation distance ℓ = 50mm. The magnitude is represented by the color bar scale shown in figures 5.4 and 5.5 and goes from zero magnitude in dark blue to a maximum value in red A γ = 5.336 was used.

The comparison for the theoretical non-axisymmetric (flexural) wave motion is shown in figure 5.11 and the experimental values for a pulse with circumferential propagation is shown in figure 5.12.

When figures 5.11 and 5.12 are compared, the experimental Gabor Wavelet plots corresponds well in trend and shape to the theoretical values. Mode S_1 is identified from both plots with a cut-off frequency below 20KHz, Mode S_2 is identified with a cut-off frequency between 20 and 40 KHz. The third mode, S_3, with a cut-off frequency of approx. 60KHz. The remaining two out of five modes (see figure 2.14),. are not shown on these plots, because their cut-off frequencies are relatively high in comparison to those for the lower modes.

As noticed in Fig. 5.12, the mode S_1, indicated by the highest wavelet coefficient magnitude predominates, as it did in figure 5.10.

For this particular situation, at relatively low frequencies (below 200KHz), a value of 5.336 was chosen to give enough time localization without losing frequency content as explained in Chapter III. The remaining two out of five modes are not shown on those plots, because their cut-off frequencies are relatively high in comparison to the ones of the lower modes.

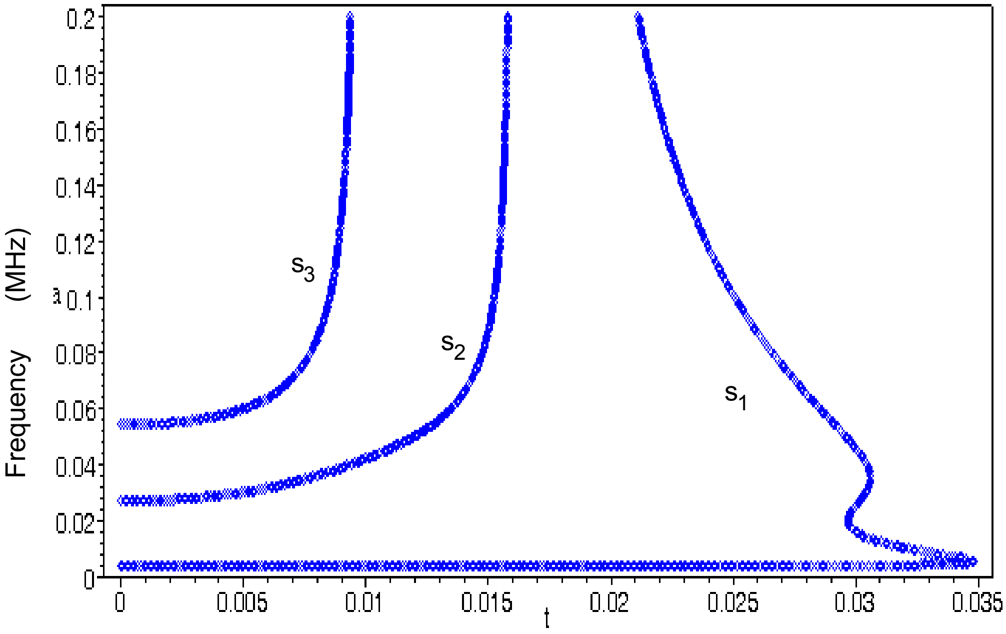

Fig. 5.11— Transformed Mirsky-Herrmann dispersion curves for flexural wave motion (n=1). Steel pipe specimen with h=7.2mm, R=33.2mm, propagation distance = 50mm. Mode S_1 is the first flexural mode, mode S_2 is the first torsional mode with a cut-off frequency of 30KHz.. The mode S_3 is the second flexural mode and has a cutoff frequency at 60 KHz.

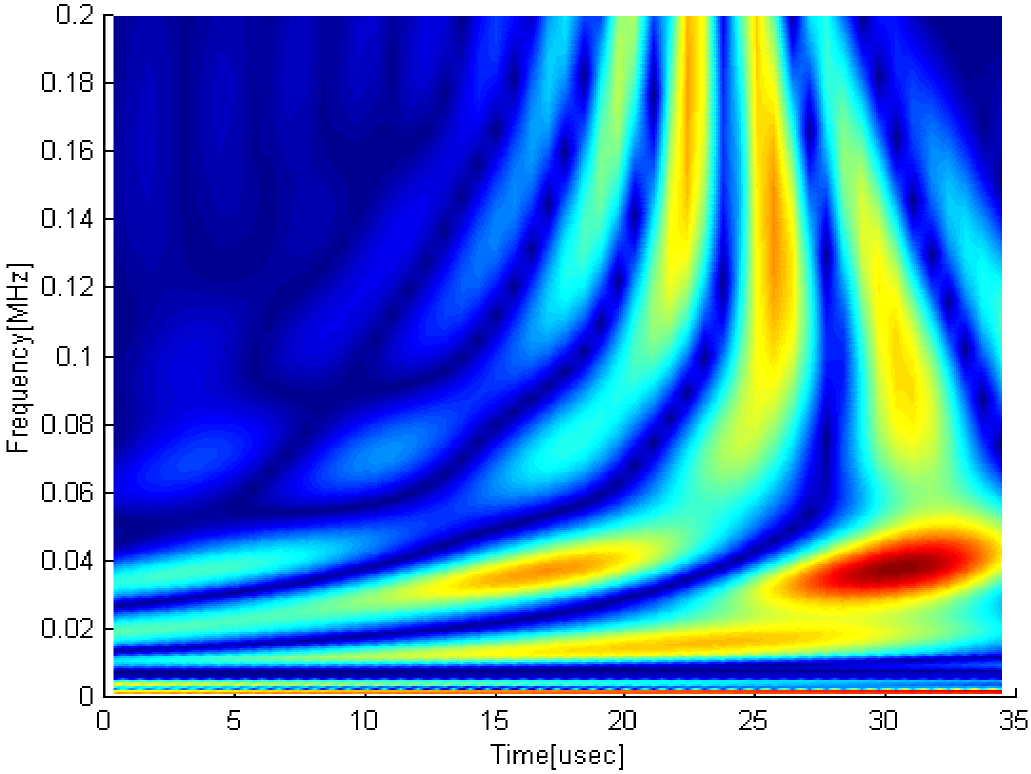

Fig. 5.12— Gabor wavelet transform for circumferential propagation direction. Steel pipe specimen with h=7.2mm, R=33.2mm, propagation distance ℓ = 50mm. The magnitude is represented by the color bar scale shown in figures 5.4 and 5.5 and goes from zero magnitude in dark blue to a maximum value in red A γ = 5.336 was used.

5.4 Results of tests on a pipe with axial propagating direction.

For the following set of figures refer to figure 4.7 for a steel tube. Figure 5.13 shows the Oscilloscope display screening the experimental waveforms at both channels. In figure 5.13(a) for case 1 (or reference) with axial propagation direction without defect. In figure 5.13(b) for case 2 with axial propagation direction with defect. The test specimen was a steel pipe with h=7.2mm, R=33.2mm. Channel 1 corresponds to FTI 1, which was located at 10mm from the source, and the corresponding trace is indicated by the number 1 (with an arrow) on the left side of the window. Channel 2 corresponds to FTI 2 located at 30mm from the source and the corresponding trace is indicated by the number 2 (with an arrow) on the left side of the window. On the top of the display the bold numbers 1 and 2 indicate the active channels, the letter E specifies that an external trigger, in this case from the Nd:YAG laser, was used. The word RUN or STOP shows that the oscilloscope is in that mode. The vertical scale is voltage and for both channels it is set to 2mV/div. The horizontal scale is time with 2μs/div with a center time of 10μs for a total captured window of 20μs. In figure 5.13(a) it can be seen pulses arriving at 3.2μs at channel 1, and 10μs at channel 2. The corresponding wave velocities are c_1=3120 and c_2 =3000 m/s which is very close to the Rayleigh wave in steel. In figure 5.13(b) the pulses are arriving at 3μs and 9.5μs with a corresponding wave velocities of c_1=3300 and c_2=3150. Again these velocities are in accordance to the Rayleigh wave velocity.

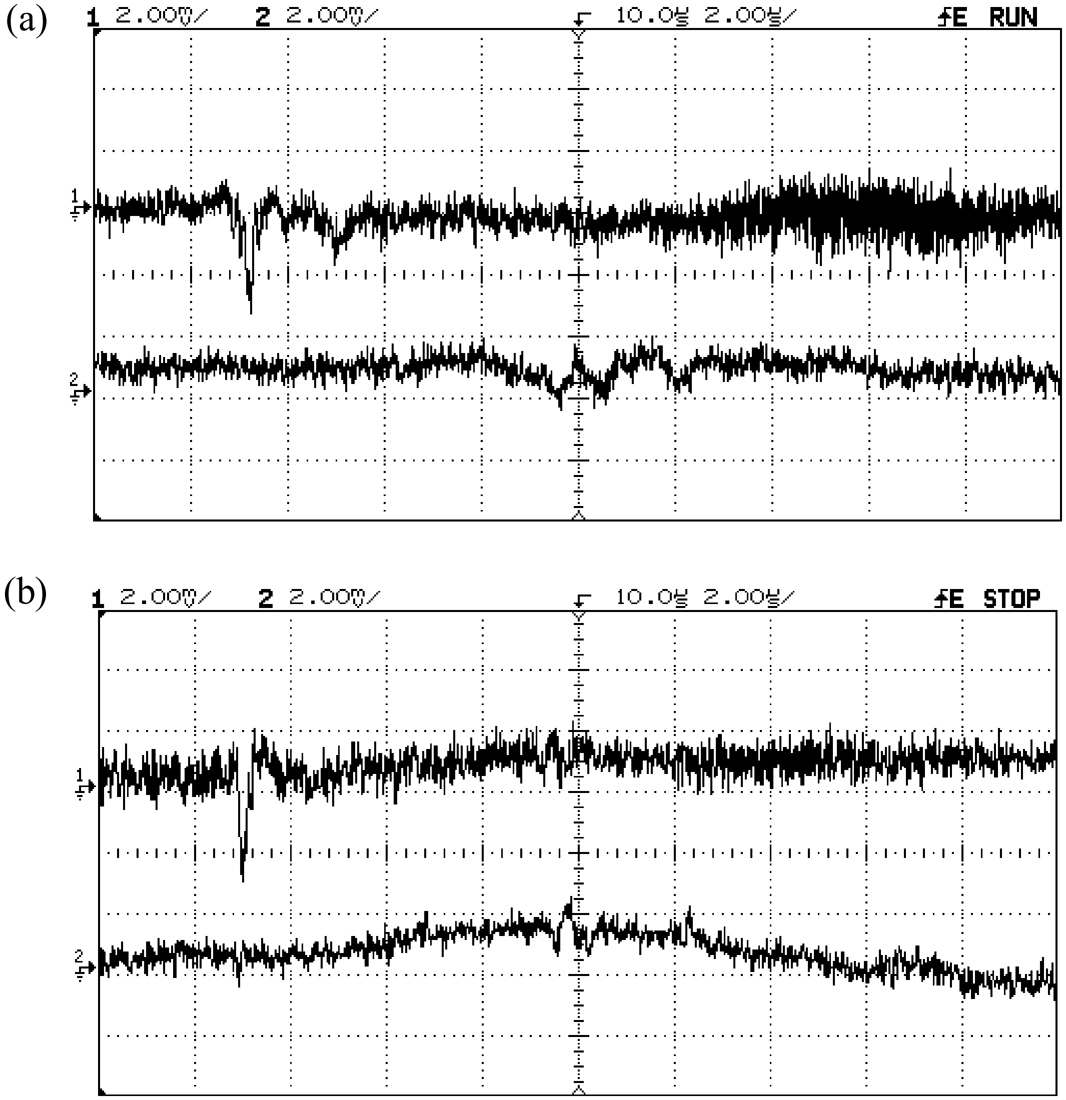

Figure 5.13—Oscilloscope display showing experimental waveforms at both channels (a) For case 1: Axial propagation direction without defect. (b) For case 2: Axial propagation direction with defect. The test specimen was a steel pipe with h=7.2mm, R=33.2mm. Channel 1 corresponds to FTI 1 which was located at 10mm from the source and the corresponding trace is indicated by the number 1 (with an arrow) on the left side of the window. Channel 2 corresponds to FTI 2 located at 30mm from the source and the corresponding trace is indicated by the number 2 (with an arrow) on the left side of the window. On the top of the display the bold numbers 1 and 2 indicate the active channels, the letter E specifies that an external trigger (from the Nd:YAG laser) was used, and the word RUN/STOP shows that the oscilloscope is in that mode. The vertical scale is voltage and for both channels it is set to 2mV/div. The horizontal scale is time with 2μs/div with a center time of 10μs for a total captured window of 20μs.

Figures 5.14 and 5.15, are the plots of wavelet transform coefficients of waves in axial direction at both locations of the fiber tip interferometers (FTIs). In both cases the top figure is for FTI 1 and the bottom figure for FTI 2. After the preliminary analysis , and being tested several γ values for the experimental data sets, it was found that values of $\gamma=5.336$ and $\gamma=10$ provide acceptable resolution, when comparing to theory. Then for all these plots, a $\gamma=5.336$ was used.

The reference conditions shown in figure 5.14 are for a defect free tube. Figure 5.15 is for data from a localization on the tube that placed “defect” between the two FTI’s. The defect was a machined slit 400μm wide, 400μm deep and 24.4mm long on the outer surface of the tube and located normal to the direction of propagation of the pulse. The specimen, as explained in section 4.4, was a tubular cylinder, made of steel with 7.2mm thickness and the locations of FTI’s are those depicted in figure 4.7. Travel distance, a, from excitation point to FTI 1 was 10mm. Travel distance ,a+b, from excitation point to FTI 2 was 30mm. For the case with a crack, this was located at 20mm from excitation point, at the mid point between both FTIs. Waveforms obtained for analysis are average of 8 consecutive sampled waveforms.

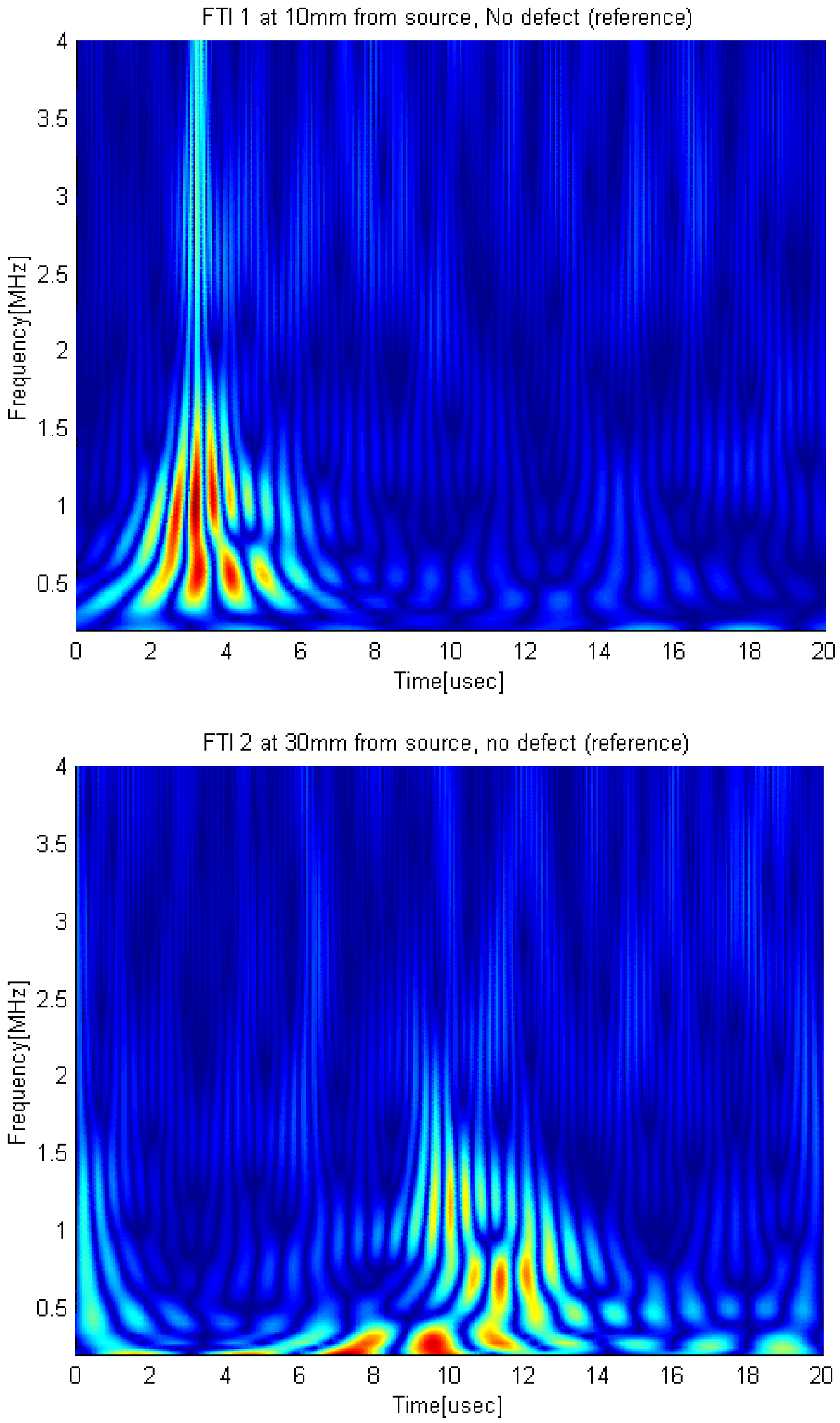
FTI 1 at 10mm from source, No defect (reference)

FTI 2 at 30mm from source, no defect (reference)

Fig. 5.14—Wavelet transform for propagation in axial direction, showing FTI 1 (above) and FTI 2 (below), case 1 on figure 4.7, no defect (Reference). A γ=5.336 was used for the program. The magnitude is represented by the color bar scale shown in figures 5.4 and 5.5 and goes from zero magnitude in dark blue to a maximum value in red.

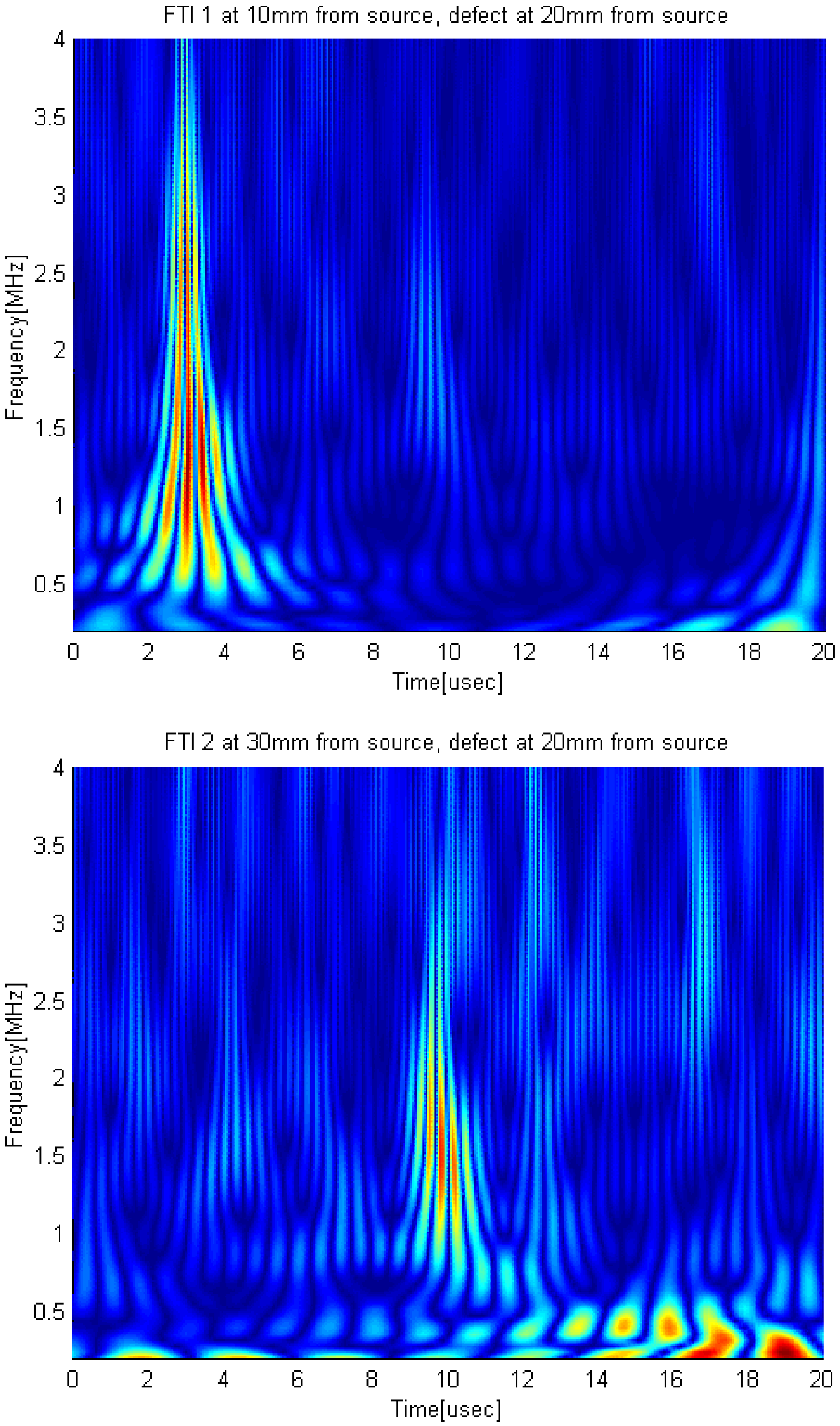

Fig. 5.15-- Wavelet transform for propagation in axial direction, showing. FTI 1 (above) and FTI 2 (below) case 2 on figure 4.7, defect (crack) in the middle of the propagation path between FTI 1 and FTI 2. A γ=5.336 was used for the program. The magnitude is represented by the color bar scale shown in figures 5.4 and 5.5 and goes from zero magnitude in dark blue to a maximum value in red.

Plots of Wavelet coefficients are able to provide information on the presence of defects as it can be seen on figures 5.14 and 5.15.

At location FTI 1, theoretically should be not variation but there are few differences between the cases before and after defect. These differences could be due to several factors. The main differences in the case 2 (after defect) with respect to the case 1 (before defect) are the appearance of a band of coefficients showing at around 10 μs with frequency band of 1.5 MHz-2.5 MHz at Figure 5.16 (FTI 1, with defect). This is because of reflections of the Rayleigh wave from the slit, which is actually showing on FTI 1 and allows the direct localization of the defect. In this case the higher frequencies are reflected by the defect and only low frequencies passes thru the second detection point FTI 2. It can be said that the slit is acting as a low-pass filter. The higher frequencies reflecting back from the slit travel with a Rayleigh wave velocity, this along the arrival time, which is counted for twice the distance from the FTI 1 to the defect, would provide the exact localization of the defect.

Other factors influencing changes could include:

- surface finishing at the detection point
- small blemishes between excitation point and detection point,
- changes of position of the pipe to adjust the actual surface to be interrogated.

At location FTI 2 however there are notable and important differences that indicate that a flaw is present in the path of the ultrasonic wave. At the reference pipe, case 1 (with no defect), dominant frequencies were found at bands of 170 KHz, 740 KHz and 1.2 MHz and arrival times around 10.5μs. At the case 2, with a crack, the dominant frequencies were found around 200 KHz, 350 KHz and 1.5 MHz. The two lower frequency bands were delayed for about 2μs.

5.5 Results of tests on a pipe with circumferential propagating direction.

For the following set of figures refer to figure 4.7 for a steel tube. Figure 5.16 shows the Oscilloscope display screening experimental waveforms at both channels. Figure 5.16(a) shows the waveform for case 3: Circumferential propagation direction without defect. Figure 5.16(b) for case 4: Circumferential propagation direction with defect. Channel 1 corresponds to FTI 1 and Channel 2 corresponds to FTI 2. FTI 1, was located at 10mm from the source and FTI 2 at 30mm from the source. The crack for figure 5.16(b) was located at the middle of both FTI's at 20mm from the source. In figure 5.16(a) it can be seen pulses arriving at 3.8μs at channel 1, and 10μs at channel 2.

The corresponding wave velocities are c_1=2630 m/s and c_2 =3000 m/s which is very close to the Rayleigh wave in steel. In figure 5.16(b) the pulses are arriving at 4.1μs with a wave velocity of c_1=2440 m/s and 9.5μs with a wave velocity of c=3150. Note that for FTI 1 the velocity does not agree with Rayleigh wave velocity. This could be due to the curvature.

Figure 5.17 and 5.18 show the plots of wavelet transform coefficients of waves in axial direction at both locations, of the fiber tip interferometers (FTIs). In all cases the top figure is for FTI 1 and the bottom figure for FTI 2. After the preliminary analysis , and being tested several γ values for the experimental data sets, it was found that values of γ=5.336 and γ=10 provide acceptable resolution, when comparing to theory. Then for all these plots, a γ=5.336 was used in the Gabor wavelet code.

The reference conditions shown in figure 5.17 are for a defect free tube. Figure 5.18 is for data from a localization on the tube that placed "defect" between the two FTI's. The defect was a machined slit 400μm wide, 400μm deep and 24.4mm long on the outer surface of the tube and located normal to the direction of propagation of the pulse. The specimen, as explained in section 4.4, was a tubular cylinder, made of steel with 7.2mm thickness and the locations of FTI's are those depicted in figure 4.7. Travel distance, a, from excitation point to FTI 1 was 10mm. Travel distance ,a+b, from excitation point to FTI 2 was 30mm. For the cases with a crack, this was located at 20mm from excitation point, at the mid point between both FTIs. Waveforms obtained for analysis are average of 8 consecutive sampled waveforms.

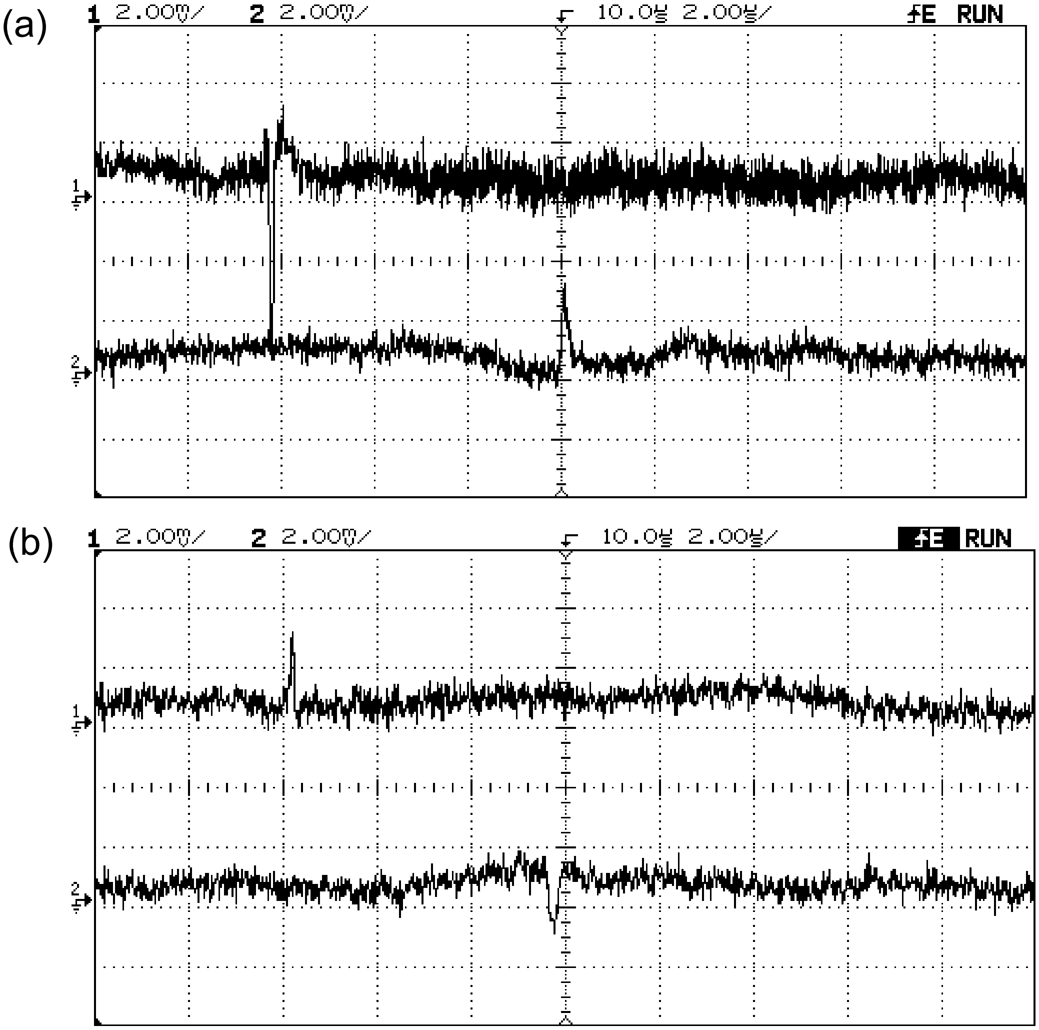

Figure 5.16—Oscilloscope display showing experimental waveforms at both channels (a) for case 3: Circumferential propagation direction without defect. (b) for case 4: Circumferential propagation direction with defect. The test specimen was a steel pipe with h=7.2mm, R=33.2mm and a crack at 20mm from the source. Channel 1 corresponds to FTI 1 which was located at 10mm from the source and the corresponding trace is indicated by the number 1 (with an arrow) on the left side of the window. Channel 2 corresponds to FTI 2 located at 30mm from the source and the corresponding trace is indicated by the number 2 (with an arrow) on the left side of the window. On the top of the display the bold numbers 1 and 2 indicate the active channels, the letter E specifies that an external trigger (from the Nd:YAG laser) was used, and the word RUN/STOP shows that the oscilloscope is in that mode. The vertical scale is voltage and for both channels it is set to 2mV/div. The horizontal scale is time with 2µs/div with a center time of 10µs for a total captured window of 20µs.

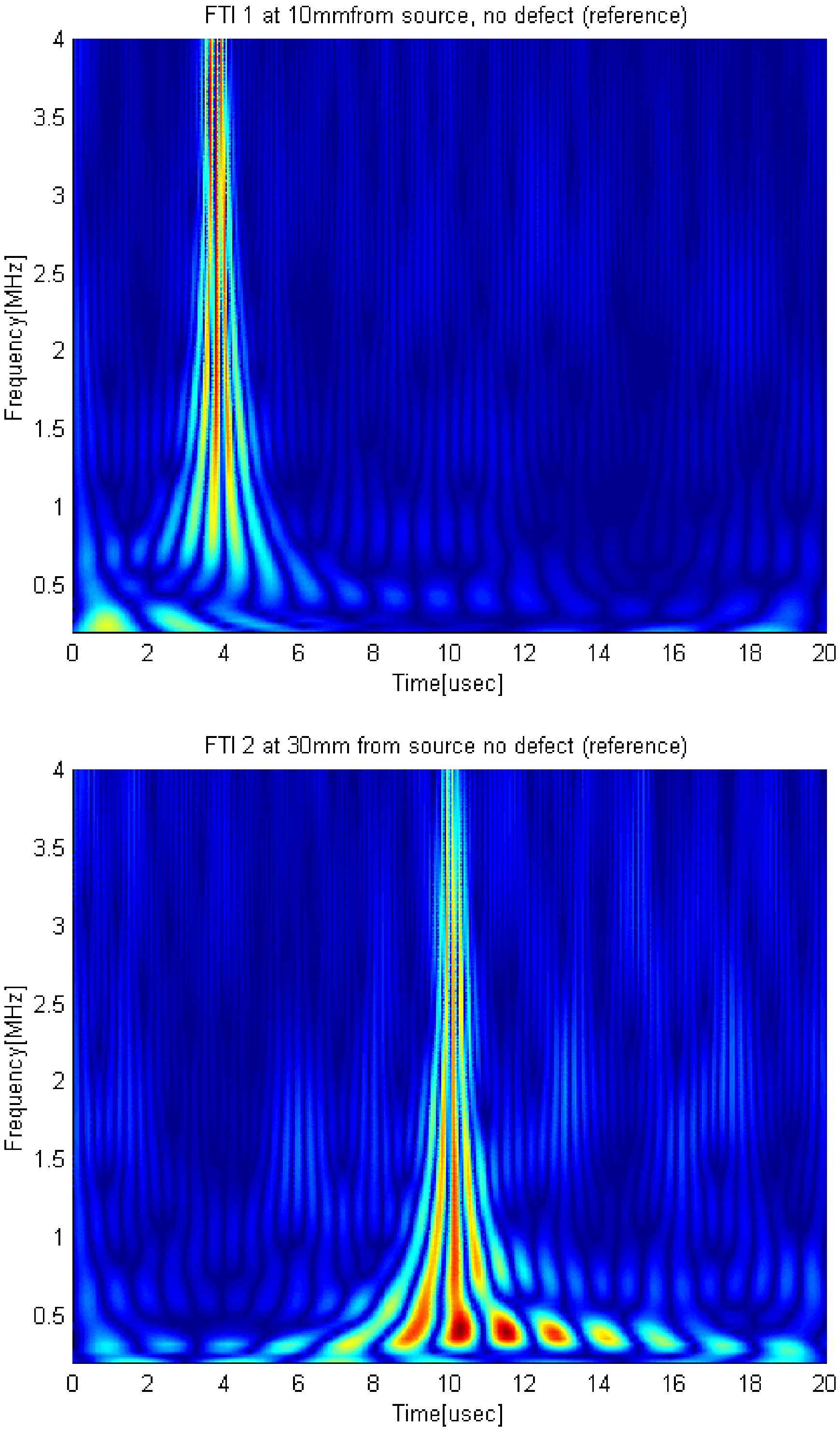

Fig. 5.17— Wavelet transform for propagation in circumferential direction, showing FTI 1 (above) and FTI 2 (below), case 3 on figure 4.7, no defect (reference). A γ=5.336 was used for the program. The magnitude is represented by the color bar scale shown in figures 5.4 and 5.5 and goes from zero magnitude in dark blue to a maximum value in red.

FTI 1 at 10mm from source, defect at 20mm from source

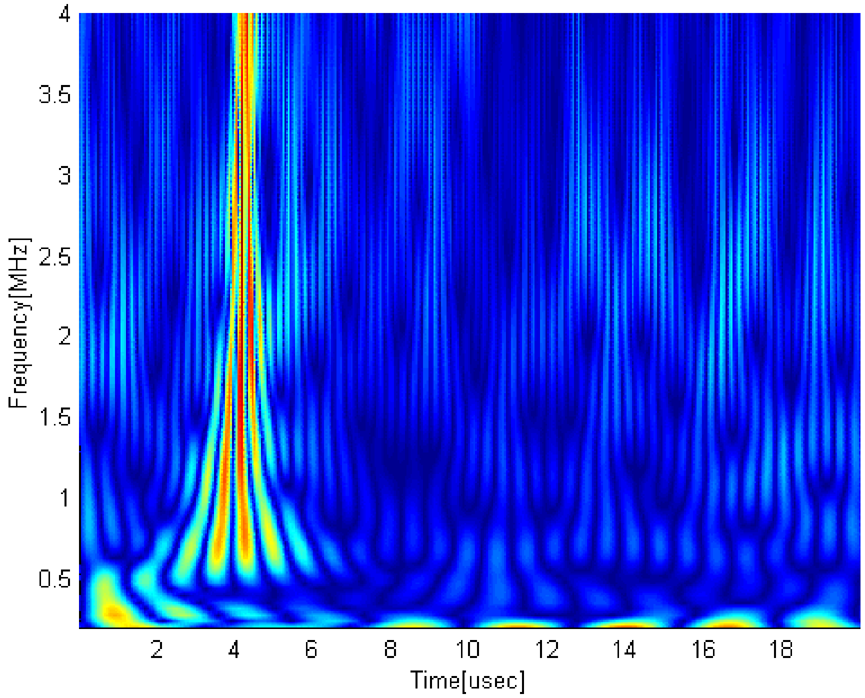

FTI 2 at 30mm from source, defect at 20mm from source

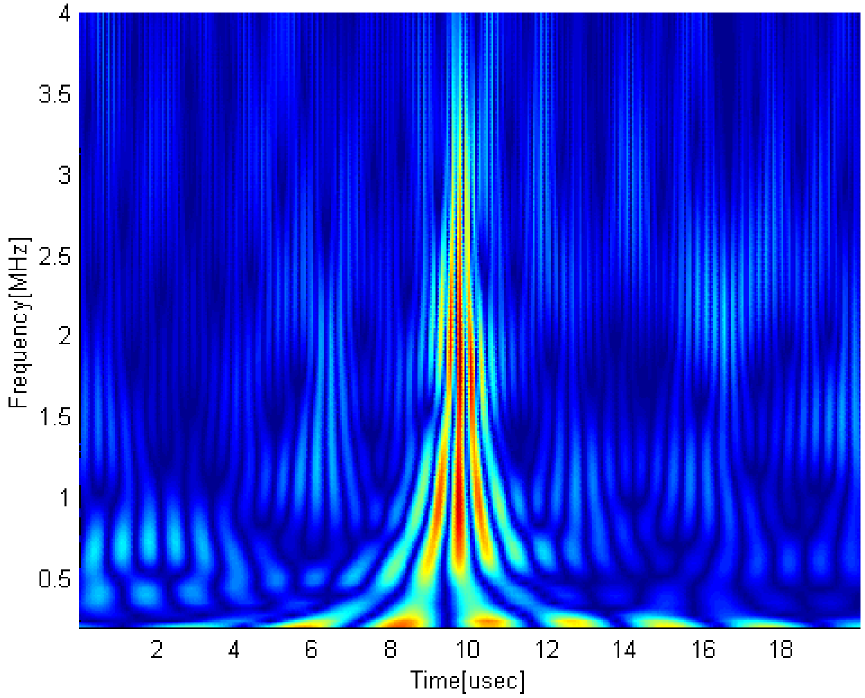

Fig. 5.18— Wavelet transform for propagation in circumferential direction, showing FTI 1 (above) and FTI 2 (below), case 4 on figure 4.7, defect (crack) in the middle of the propagation path between FTI 1 and FTI 2. A γ=5.336 was used for the program. The magnitude is represented by the color bar scale shown in figures 5.4 and 5.5 and goes from zero magnitude in dark blue to a maximum value in red.

In circumferential direction A γ=5.336 was used for the program. The magnitude is represented by the color bar scale shown in figures 5.4 and 5.5 and goes from zero magnitude in dark blue to a maximum value in red.

As in the previous cases, at location FTI 1, theoretically should be not variation. There are few differences at FTI 1 between case 3 (before defect) and case 4 (after defect) product of reflections from the slit of lower mode components. At location FTI 2 however there are also notable and important differences that indicate that a flaw is present in the path of the ultrasonic wave.

These results are shown in figures 5.17 and 5.18. At the reference pipe (with no defect), dominant frequencies were found at bands of 380KHz, 800KHz and 1.4MHz and arrival times around 10µs. At the pipe with a crack, the dominant frequencies were found around 200KHz, 680KHz, 1MHz and 1.8MHz.There are a fast 700MHz component arriving around 2µs and also a slow 2.2MHz component arriving at 16.5µ..

When comparing the plots of circumferential propagation, Figs, 5.17 and 5.18, to those of the axial propagation, Figs 5.14 and 5.15, it is clear that the Rayleigh wave predominates over circumferential direction. This could be due to the dimensions of the pipe, which makes the pipe stiffer along the circumference resisting the Lamb-mode propagation.

5.6 Summary

For a pipe with the dimensions used in this research, the waveforms obtained were neither completely surface nor completely plate waves, but a combination of the characteristic feature of both families of ultrasonic waves. These are referred as transition waves.

In a study of the feasibility to detect flaws in cylinders with propagation paths along axial and circumferential directions, it was found that the experimental data processed through the Gabor wavelet transform are directly related to the transformed Mirsky-Herrmann dispersion curves. This is because the arrival times obtained from the frequency-time combined with a fixed propagation distance would give the velocity of the wave. Thus this alternative representation of dispersion curves can be used to analyze transition waves, which were obtained for four cases without and with defect.

The validation of the process was carried out by direct comparison between the theoretical dispersion curves and experimental data. For cases first and third (with no defect), the results were compared directly with theory by using a transformation process. The experimental curves matched well with those of the Mirsky-Herman theory for circumferential motion. Also it was noticed that the Rayleigh wave component is predominant on circumferential propagation, Figs. 5.17 and 5.18, when compared to axial propagation, figures 5.14 and 5.15. This is because the pipe specimen interrogated is stiffer on cylindrical direction due to its dimensions and resists the Lamb-type oscillations.

The significant difference in dispersion spectrums between both cases, when analyzed with Gabor wavelets, are indicative that defects can be identified directly from the dispersion graphs. This was evident in the plots after defect Fig. 5.15 and 5.18, where reflections and changes on frequency components and arrival times were observed. Therefore the methodology can be used to detect flaws in cylindrical surfaces within an inspection system with a completely non-contact and non-invasive fashion, without disturbing the wave propagation.

CHAPTER VI

CONCLUSIONS AND FUTURE RESEARCH

Laser generated ultrasonic waves have unique advantages when compared to traditional contact ultrasonic generation. Some of these advantages include: non-contact and non-invasive transduction, testing can be in hostile environments or hard to reach places, possibility of interrogation of curved surfaces and inspection of large areas using mirror scanning systems. The particular synergy obtained by the use of the non-contact ultrasonic generation and detection technique with a signal processing, which allows resolutions in time and frequency domains, makes this methodology very promising for implementation in inspection systems of pipes.

6.1 Conclusions

This research shows how the synergy obtained from combining the use of the Thermo-Acoustic Photonic Non destructive Evaluation (TAP-NDE) with the wavelet transform method for signal analysis can be used to inspect tubulars.

By employing a transformation step, as described in Chapter II, it is possible to have a direct comparison between the theoretical dispersion curves and experimental dispersion curves. The Mirsky-Herrmann theory dispersion curves are originally expressed in terms of normalized velocity vs. normalized wave number, Fig. 2.9 and Fig. 2.10. Experimental dispersion curves are usually available in terms of time and frequency. With the transformation explained in Chapter II it is possible to have both theoretical and experimental dispersion curves expressed in terms of time Vs. frequency thus enabling a direct comparison between them, as shown in figures. 5.9-5.12. The experimental curves were obtained directly from the Gabor wavelet coefficients by localizing the arrival times when the wavelet coefficients were maximum for each frequency content in the plots.

It was experimentally demonstrated that the “apparent” slower Rayleigh waves that were obtained during tests, were not Rayleigh waves. The waves detected by the FTI were refractions of the HeNe beam when exiting from the grin lens. Those refractions are due to the shock waves and the thermal expansion of the hot air in the core of the decaying plasma formed by the laser focused into a point. Remembering that for steel pipe specimens, the energy used is considerably high in order to produce ultrasonic waves and there is no way to work only within thermoelastic regime without forming plasma.

It was shown in this research, that noisy signals can be characterized with wavelet transform without affecting the useful information contained in the signal for a useable frequency range up to 5MHz. Also was proved that, for the experiments carried out in this research, there is no difference in the Gabor Wavelet plots, whether the signal is de-noised or not, by using the method mentioned in Chapter V.

Additionally it was found that for the particular pipe specimen thickness used here, the waves that were obtained were transition waves, with characteristics that lie between surface waves and plate waves. This is shown in Fig. 5.8.

Some degree of agreement between the Mirsky-Herrmann theory of dispersion in cylinders and the experimental data was obtained as shown in figures 5.9-5.12.

Finally, the research showed that if the Gabor wavelet transform is used, significant differences are revealed in the dispersion plots from guided ultrasonic pulses that propagate in good sections of pipe wall and when they encounter defects. This suggests that defects can be identified directly from the dispersion graphs. Therefore the methodology can be used to detect flaws on cylindrical surfaces in a completely non-contact and non-invasive fashion.

Then it can be said that this methodology may be implemented in a inspection system of cylinders, tubulars or pipes. The wavelet transform can be easily adapted into hardware as filter banks making it suitable for real time in-line inspections. The principal advantage of this new method is that parts can be inspected without any coupling media like water so that guided waves can be used to interrogate large areas at a time.

6.2 Future Research

Some work is needed in order to extrapolate the methodology from the laboratory to field inspection. These are:

1. Develop a substitute for the Laser used in the generation stage. Now the Nd:YAG laser is huge and bulky and could not be suitable for field inspections. There is a need for a more compact high power and short-pulsed laser. It would be better if that laser had a "tunable" pulse duration, whose broadband frequency could be adapted to the test specimen's thickness in such a way that it could be used to control the surface wave penetration depth.

2. For industrial applications, the FTI has several limitations. The sensitivity of the FTI to detect out of plane displacements depends on the reflectivity of the surface being interrogated, and an accurate alignment of the sensor. In order to overcome these limitations it is necessary to:

    a. Find a way to increase the contrast on the FTI's without polishing the surface of the test specimen. With the actual system, it is necessary to have a good reflecting surface in order to have the interference (object beam). Some suggestions are:

        - Use of a larger collimating lens, allowing more scattered light coming into the sensing system.

    - Optical tuning of the beams in the fiber optic systems by using back-reflecting devices and attenuators, in such a manner that the intensity of both beams, reference beam and object beam can be controlled. Then increasing the contrast to provide higher intensity of the interference pattern.

    - Increase the beam intensity by using a higher power HeNe laser.

   b. Use a positioning system to automate the alignment of the FTI, specifically the grin lens. The grin lens should be perfectly perpendicular to the test surface in order to detect the out of plane displacements. This is difficult to achieve, particularly for curved surfaces. At the actual detection subsystem, the alignment is made by hand. In order to have a good interference pattern in a short time, the person doing the alignment must be highly experienced, otherwise it could take hours before a good intensity is shown at the photodetector.

3. Another approach, as an alternative to the problems encountered in the FTI system, could be to use other types of interferometers as non-contact sensors that will not need special specimen preparation. For example, the Infrared Fizeau interferometer[95] which uses a CO_2 laser as a light source and the out of plane displacements can be detected from a rough surface. Alternatively, the Injected Locked Laser (ILL) sensor technology developed by J. Smith[96], can be used with a heterodyne interferometer system.

4. With respect to the Data analysis system, it could be useful to try another techniques, such as the Hilbert transform and compare them to the Gabor wavelet transform. More study is needed regarding the influence of changing some

parameters of the Gabor wavelet, and how they can be used to get an optimum representation of dispersion to characterize flaws in the coefficients' plots.

5. A deeper knowledge, both experimentally and theoretically of the thermo-acoustic generation process on curved surfaces is needed. Most of the research done in this respect has been focused considering thermo-acoustic generation on flat surfaces.

6. The whole system could be customized for a particular material, dimensions, etc. by tuning the frequency bandwidth, assuming that the laser in use is as proposed in point 1, or by using frequency controlled narrow-band generation.

7. At the moment of reporting this work, no mathematical model was known to take care of the defects on the propagation path of dispersive waves on curved surfaces. Mirsky-Herrmann theory, as well as other available dispersion theories, assumes a "clean" propagation path with no defects. A new theoretical model of dispersion on cylindrical surfaces taking into account defects is necessary to have the theoretical frame complete with respect to the experiments shown in this work.

8. Finally, more work is needed in order to characterize and to quantify defects by using the methodology presented in this research.

REFERENCES

1. Stefani, S.A; Nagarajah, C.R.; Toncich, D.J. “Non Contact Inspection for the Detection of Internal Surface Defects in Hollow Cylindrical Work-pieces”, International Journal of Advanced Manufacturing Technology, **11** (2), 146-154 (1996).

2. Burger, C.P., Schumacher, N.A., Duffer, C.E. and Knab, T.D. “Fiber Optic Techniques for Generating and Detecting Ultrasonic Waves for Quantitative NDE”, Optics and Lasers in Engineering, **19**, 121-140 (1993).

3. Suh, C.S., Rabroker, G.A., Chona, R., and Burger, C.P., **“**Lamb Wave Propagation as a Temperature Diagnostic in Silicon Wafer Processing: Experimental Implementation and Results”, Proceedings of the 1998 SEM Spring Conference on Experimental Mechanics, 455-458 (1998).

4. Suh, C.S., Rabroker, G.A., Chona, R., and Burger, C.P., **“**Thermal-Acousto-Photonics for Non-contact Temperature Measurement in Silicon Wafer Processing”, 1999 SPIE Proceedings of Optical Diagnostics for Fluids/Heat/Combustion and Photomechanics for Solids, **3783**, 184-193 (1999).

5. Burger, C. P., Dudderar, T. D., Gilbert, J. A., Peters, B.R., Smith, J. A., Raj, B., “Thermal Acousto-Optic Excitation for Non-Contacting NDE”, Proceedings of the 1986 SEM Spring Conference on Experimental Mechanics, New Orleans, LA, Soc. for Experimental Mechanics Inc, Bethel, CT, 680-685, (1986).

6. Sahn Q.; Chen, C. M.; Dewhurst, R. J. “Detection of Laser-generated Ultrasound with a Conjugate Interferometer Scheme”, Ultrasonics, **34** ,173-175 (1996).

7. Hayashi, Y., Ogawa, S., Cho, H., Takemoto, M., " Non-contact Estimation of Thickness and Elastic Properties of Metallic Foils by Wavelet Transform of Laser-generated Lamb Waves", NDT&E International, **32** , 21-27 (1999).

8. Strang, G. and Nguyen, T, Wavelets and Filter Banks, Wellesley-Cambridge Press, Wellesley, MA (1996).

9. Jeong, H., Jang, Y.-S., "Wavelet Analysis of Plate Wave Propagation in Composite Laminates", Composite Structures, **49**, 443-450 (2000).

10. Wu, T.-T., Chen, Y.-Y., "Wavelet Analysis of Laser-Generated Surface Waves in a Layered Structure with Unbound Regions", ASME, Journal of Applied Mechanics, **66**, 507-513 (1999).

11. Hansch, M.K.T., Rajana, K. M., Rose, J.L., "Characterization of Aircraft Joints Using Ultrasonic Guided Waves and Physically Based Feature Extraction", Proceedings of the IEEE 1994 Ultrasonics Symposium, IEEE, Piscataway, NJ, 1193-1196 (1994).

12. Lowe, M.J.S., Alleyne, D.N., Cawley, P., "Defect Detection in Pipes Using Guided Waves", Ultrasonics, **36**, 147-154 (1998).

13. Park, H.M., Kim, S.. Yoon, Y.K., "Ultrasonic Inspection of Long Steel Pipes Using Lamb Waves", NDT & E International, **29**(1), 13-20 (1996).

14. León, F., Maze, G., "Radiation of Guided Waves at the Extremity of a Semi-infinite Cylindrical Shell", Proceedings of the Third International Congress on Air- and Structure-borne Sound and Vibration, June 13-15, Montreal Canada, 53-58 (1994).

15. Ditri, J. J., Hongerholt, D.,"Stress Distribution Determination in Isotropic Materials via Inversion of Ultrasonic Rayleigh Wave Dispersion Data", Int. J. Solids Structures, **33**(17), 2437-2451 (1996).

16. Koshiba, M., Okada, M., Suzuki M., "Numerical Analysis of Acoustic Wave Propagation along the Azimuthal Direction in Cylindrically Layered Waveguides by Finite-Element Method", The Transactions of the IECE of Japan, **E66** (1), 1-5 (1983).

17. Sachse, W and Pao Y. H. "On the Determination of Phase and Group Velocities of Dispersive Waves in Solids" ,J. Appl. Phys., **49**(8), 4320-4327 (1978).

18. Alleyne D. and Cawley P., " A Two-dimensional Fourier Transform Method for the Measurement of Propagating Multimode Signals", J. Accoust. Soc. Am. **89**(3), 1159-1168 (1991).

19. Kishimoto K., Inoue H. Hamada M., and Shibuya T., "Time Frequency Analysis of Dispersive Waves by Means of Wavelet Transform", Journal of Applied Mechanics, **62**, 841-846 (1995).

20. Abbate A., Frankel J. and Das P. "Wavelet Transform Signal Processing for Dispersion Analysis of Ultrasonic Signals", Proceedings of the 1995 IEEE Ultrasonics Symposium, 751-755 (1995).

21. Wooh, S.C. and Veroy K. "Spectrotemporal Analysis of Guided-Wave Pulse-echo Signals: Part 2. Numerical and Experimental Investigations", Experimental Mechanics, **41**, 332-342 (2001).

22. Park H.C., Kim D. S., "Evaluation of the Dispersive Phase and Group Velocities Using Harmonic Wavelet Transform", NDT & E International, **34**, 457-467 (2001).

23. Eisenhardt C., Jacobs L. J. and Qu J., "Application of Laser Ultrasonics to Develop Dispersion Curves for Elastic Plates", Journal of Applied Mechanics, **66**, 1043-1045 (1999).

24. Pierce, S.G., Culshaw, B., Philp, W.R., Lecuyer, F., Farlow R., “Broadband Lamb Wave Measurements in Aluminum and Carbon-glass Fibre Reinforced Composite Materials Using Non-contacting Laser Generation and Detection”, Ultrasonics, **35**, 105-114 (1997).

25. Valle C., "On Characterizing Multi-Mode, Dispersive Lamb Waves", Review of Progress in Quantitative Nondestructive Evaluation, **20**, 1047-1052 (2001).

26. Valle, C., Qu, J., Jacobs, L.J., “Guided Circumferential Waves in Layered Cylinders”, International Journal of Engineering Science, **37**, 1369-1387 (1999).

27. Rose, J. L., Ultrasonic Waves in Solid Media, Cambridge University Press, New York (1999).

28. Viktorov, I. A. , Rayleigh and Lamb Waves-Physical Theory and Applications, Plenum Press, New York (1967).

29. Huang, J., Krishnaswamy, S. and Achenbach, J. D., “Laser Generation of Narrow-band Surface Waves”, Journal of the Acoustical Society of America, **92**(5), 2527-2531 (1992).

30. Berthelot, Y. H; Jarzynski, J., “Directional Laser Generation and Detection of Ultrasound with Arrays of Optical Fibers”, Review of Progress in Quantitative Nondestructive Evaluation. **9A** , Plenum Press, New York, 463-470, (1990).

31. Solie, L P; Auld, B A., “Elastic Waves in Free Anisotropic Plates (Dispersion Curve Computation for Elastic Acoustic Waves Propagation in /001/-cut Cubic Free Anisotropic Plate, Noting Relationship with Slowness Curves for Bulk Waves)”, Journal of the Acoustical Society of America, **54**, 50-65 (1973).

32. Graff, K. F., Wave Motion in Elastic Solids, Dover Publications Inc., Reprint, New York, (1991)

33. Achenbach, J. A., Wave Propagation in Elastic Solids, American Elsevier, New York, 5th Edition, (1987).

34. Wilcox, P., Lowe, M., Cawley P., “The Effect of Dispersion on Long-range Inspection Using Ultrasonic Guided Waves”, NDT&E international **34**,1-9 (2001).

35. Mirsky I. and Herrmann G., “Nonaxially Symmetric Motions of Cylindrical Shells”, J. of Acoust. Soc. Am., **29**(10), 1116-1123 (1957).

36. Mirsky, I., “Wave Propagation in Transversely Isotropic Circular Cylinders Part I: Theory and Part II: Numerical Results”, Journal of Acoust. Soc. Am, **37**(6), 1016-1026 (1965).

37. Mirsky I. and Herrmann G. “ Axially Symmetric Motions of Thick Cylindrical Shells”, J. of Appl. Mechanics, **25**, 97-102 (1958).

38. Heimann, J. H. and Kolsky, H., “The Propagation of Elastic Waves in Thin Cylindrical Shells”, J. of Mech. Phys. Solids, **14**, 121-130 (1966).

39. Love A.E.H., A Treatise on the Mathematical Theory of Elasticity, Dover Publications, New York, fourth Edition (1944)

40. Naghdi, P. M. and Cooper R. M., “Propagation of Elastic Waves in Cylindrical Shells, Including the Effects of Transverse Shear and Rotary Inertia”, J. Acoust. Soc. Am., **28**, 56-63 (1956).

41. Herrmann G. and Mirsky I., “Three-Dimensional and Shell-Theory Analysis of Axially Symmetric Motions of Cylinders”, J. of Applied Mechanics, **23**, 563-568 (1956).

42. Gazis ,D.C., “Three-Dimensional Investigation of the Propagation of Waves in Hollow Circular Cylinders. I, Analytical Foundation and II. Analytical Results”, J. Acoust. Soc. Am., **31**, 568-578(1959).

43. Goldsmith, W.; Lee, P.Y. ; Sackman, J.L., “Pulse Propagation in Straight Circular Elastic Tubes”, J. Appl. Mech., **39**, 1011-1018 (1972).

44. Shul'ga, N.A., “Propagation of Axisymmetric Elastic Waves in an Orthotropic Elastic Cylinder”, Sov. Applied Mech. **10** (9) ,936-939 (1974).

45. Ramskaya E.I. and Shul'ga N.A., “Study of the Velocities and Modes of Propagation of Axisymmetric Waves along an Orthotropic Hollow Cylinder”, Sov. Applied Mech., **19**(3), 207-211(1983).

46. Rulf B., “Rayleigh Waves on Curved Surfaces”, J. Acous. Soc. Am. **45**, 493-499 (1968).

47. Mindlin, R.D., “Influence of Rotatory Inertia and Shear on Flexural Motions of Isotropic Elastic Plates”, Journal of Applied Mechanics, Trans. ASME, **73**,31-38 (1951).

48. Greenspon, J.E., “Vibrations of a Thick-Walled Cylindrical Shell – Comparison of the Exact Theory with Approximate Theories”, Journal of the Acoustical Society of America, **32**(5), 571-578 (1960).

49. Armenakas, A. E., Gazis, D. C., Herrman, G., Free Vibrations of Circular Cylindrical Shells, Pergamon Press, New York (1969)

50. Waterloo Maple Inc., Maple VI User’s Guide, Waterloo, Ontario Canada (2000).

51. Legendre, S., Goyette, J., Massicotte, D. “Ultrasonic NDE of Composite Material Structures Using Wavelet Coefficients”, NDT & E International, **34**, 31-37 (2001).

52. Chen, Y.J.; Shi, Y. W; Lei, Y.P. “Use of a Wavelet Analysis Technique for the Enhancement of Signal-to-noise Ratio in Ultrasonic NDE”, Insight: Non-Destructive Testing and Condition Monitoring, **38**(11),800-803 (1996).

53. Gaberson, H.A., “The Use of Wavelets for Analyzing Transient Machinery Vibration”, Sound and Vibration,12-17, September (2002).

54. Chang, R.-S., Sheu, J.-Y., Lin, C.-H., Liu, H.-C., “Analysis of CCD Moiré Pattern for Micro-range Measurements Using the Wavelet Transform”, Optics & Laser Technology, **35**, 43-47 (2003).

55. Strang, G., "Wavelets", American Scientist, **82**, 250-255 (1994).

56. Ramirez, R.W., The FFT Fundamentals and Concepts, Prentice Hall, Englewood Cliffs, NJ (1985).

57. Gabor D., "Theory of Communication", Journal of Institute of Electrical Engineering, **93**, 429-457 (1946)

58. Shin, H.J., Song, S.J., "Time Frequency Analysis of Lamb Waves for Distance and Thickness Measurement", Review of Progress in Quantitative Nondestructive Evaluation, **20**, 149-155, (2001).

59. Sheng, Y. "Wavelet Transform." The Transforms and Applications Handbook: Second Edition. Chapter 10. Ed. A. D. Poularikas,: CRC Press, Boca Raton FL (2000)

60. Poularikas A. D. "Wavelet Transforms" The Handbook of Formulas and Tables for Signal Processing, Chapter 42. Ed. A. D. Poularikas, CRC Press, Boca Raton FL (1999)

61. Daubechies, I., Ten Lectures on Wavelets, 2nd. Ed., SIAM, Philadelphia, PA (1992).

62. Niethammer, M., Application of Time Frequency Representations to Characterize Ultrasonic Signals, M.S. Thesis, Georgia Institute of Technology (1999).

63. Matlab® High Performance Numeric Computation and Visualization Software, Reference Guide, The Math Works Inc. Natick, MA (2001).

64. Goupillaud, P. Grossmann, A; and Morlet J., “Cycle-octave and Related Transforms in Seismic Signal Analysis”, Geoexploration, **23**, 85-102 (1994).

65. Smith, J.A., “Thermal Acousto-Photonics for the Generation and Detection of Ultrasonic Waves”, Master’s Thesis, Texas A&M University, (1987).

66. Burger, C. P., Dudderar, T. D., Gilbert, J. A., Peters, B.R., Smith, J. A., Raj, B., (1986) “Thermal Acousto-Optic Excitation for Non-Contacting NDE”, Proceedings of the 1986 SEM Spring Conference on Experimental Mechanics, New Orleans, LA, Soc. for Experimental Mechanics Inc, Bethel, CT, 680-685, (1986).

67. Costley, R.D., Berthelot Y.H., “Dispersion Curve Analysis of Laser-generated Lamb Waves”, Ultrasonics, **32**(4), 249-253 (1994).

68. Scruby, C.B., Dewhurst, R.J., Hutchins, D.A., Palmer, S.B.,” Quantitative Studies of Thermally Generated Elastic Waves in Laser-irradiated Metals”, Journal of Applied Physics, **51**(12), 6210-6216 (1980.)

69. Hutchins, D.A., Dewhurst, R.J. ., Palmer, S.B., Scruby, C.B., ”Laser Generation as a Standard Acoustic Source in Metals”, Journal of Applied Physics, **38**(9), 677-679, (1981).

70. Vandervort, K.D., “Wavelength Reinforced Thermo-Acousto-Photonic NDE of an Elastomer to Steel Adhesive Bond”, Ph.D. Dissertation, Texas A&M University (1997).

71. Sanderson, T., Ume, C., Jarzynski, J., “Longitudinal Wave Generation in Laser Ultrasonics”, Ultrasonics, **35**, 553-561 (1998).

72. Kley, M., Valle, C., Jacobs, L. J., Qu, J., Jarzynski,J., “Development of dispersion Curves for Two-layered Cylinders Using Laser Ultrasonics”, J. Acoust. Soc. Am., **106**(2), 582-588 (1999).

73. Aindow, A.M., Dewhurst, R.J., Palmer S. B., Scruby, C. B., “Laser-based Non-Destructive Testing Techniques for the Ultrasonic Characterization of Subsurface Flaws”, NDT International, **17**(6), 329-335 (1984).

74. Bobbin, S.E., Wagner J. W., Cammarata, R. C., “Interpretation of Laser-generated Low-order Lamb Waves for Elastic Modulus Measurements in Thin Films”, Ultrasonics, **30**(2), 87-90 (1992).

75. Qu, J., Berthelot, Y.H., Jacobs, L.J., “Crack Detection in Thick Annular Components Using Ultrasonic Guided Waves”, Proceedings of the Institution of Mechanical Engineers., **214**(C),1163-1171 (2000).

76. Valle, C., Jacobs, L. J., “Scattering of Circumferential Waves in a Cracked Annulus”, Review of Progress in Quantitative Nondestructive Evaluation, **19**, 217-224 (1994).

77. Burger, C. P., Dudderar, T. D., Gilbert, J. A., Smith, J. A., Peters, B.R, “Use of Fiber Optic Interferometry to Sense Ultrasonic Waves”, ISA Transactions, **28**(2), 51-55 (1989)

78. Gilbert, J.A., Burger, C.P., Dudderar, T. D., Smith, J.A., Peters, B. R., “Detection and Evaluation of Ultrasonic Waves Using Single Mode Optical Fiber Interferometry”, Proceedings of the International Congress on Experimental Mechanics, 6th, Portland, OR, June 6-10, 1988, Society for Experimental Mechanics, Inc., Bethel, CT, **1**, 441-448 (1988).

79. Dudderar, T. D., Burger, C. P., T. D., Gilbert, J. A., Smith, J. A., Peters, B.R, "Fiber Optic Sensing for Ultrasonic NDE", Journal of Nondestructive Evaluation, **6**(3), 135-146, (1987)

80. Knab, T. D. "Improvements and Applications of Non-contacting Interferometry", Master's Thesis, Texas A&M University (1994).

81. Litters, J. W., Jacobs, L. J., Qu, J., "Laser Interferometric Investigation of Scattering from a Distribution of Cracks", Review of Progress in Quantitative Nondestructive Evaluation, **13**, 61-68 (1994).

82. Oz Optics Ltd., "Fiber Optic Components Handbook and Catalog", www.ozoptics.com (1999)

83. Oz Optics Ltd., "Standard Tables", Tables 1, and 6-12, www.ozoptics.com, (1999).

84. Knab,T.D., "Improvements and Applications of Non-contacting Interferometry", chapter II, Master's Thesis, Texas A&M University (1994).

85. Hewlett Packard, "HP 54645A Oscilloscope and HP 54645D Mixed-Signal Oscilloscope, user and service Guide", Palo Alto, CA (1997).

86. Burger, C. P., Dudderar, T. D., Gilbert, J. A., Peters, B.R., Smith, J. A., "Laser Excitation Through Fiber Optics for NDE", Journal of Nondestructive Evaluation, **6**(1), 57-64 (1987)

87. Duffer, C.E., "Use of Fiber Optic Guided, Laser Induced Acoustic Waves for NDE", Master's Thesis, Texas A&M University (1990).

88. Lanza di Scalea F., Berndt T.P., Sicer, J.B., Djordjevic B.B., “Remote Laser Generation of Narrow-Band Surface Waves Through Optical Fibers”, IEEE Transactions on Ultrasonics, Ferromagnetics and Frequency Control, **46**(6), 1551-1557 (1999).

89. Baltazar, M.E., Chona, R., Suh, S., Burger, C.P., “Non-contact Inspection Method in Tubulars by Laser-generated Ultrasound and FTI”, Optical Methods I, paper 113, Proceedings of the SEM Annual Conference and Exposition of Experimental & Applied Mechanics, June 10-12, Milwaukee, WI, (2002).

90. Smith, J.A, “Thermal Acousto-Photonics for the Generation and Detection of Ultrasonic Waves”, Master’s Thesis, Texas A&M University, (1987).

91. Peters, B.R., “A Fiber Optic Based Thermal Acousto-Photonic System for Noncontacting Nondestructive Evaluation”, Ph.D. Dissertation, Chapter V, University of Alabama in Huntsville (1990).

92. Scruby C. B and L. E. Drain., “Laser Ultrasonics: Techniques and Applications”, Institute of Physics Publishing, Philadelphia (1990).

93. Aindow, A.M., Dewhurst, R. J., Palmer, S. B., and Scruby C. B., Laser-based Non-destructive Testing Techniques for the Ultrasonic Characterization of Subsurface Flaws”, NDT International, **17**(6), 329-335 (1984)

94. Villagrán-Muniz, M., Sobral H.,Navarro-González, R., “Shock and Thermal Wave Study of Laser-induced Plasmas in Air by the Probe Beam Deflection Technique”, Measurement Science & Technology, Institute of Physics Publishing,**14**(5), 614-618,(2003).

95. Verma, K. and Han, B., "Far Infrared Fizeau Interferometry: Theory and Applications to Microelectronics Packaging", Session 74, Dr. C.P. Burger Symposium-Non destructive Evaluation, Paper No. 374, 2003 SEM Annual Conference, Charlotte, NC, June 2-4 (2003).

96. Smith, J.A., "Heterodyne Interferometry Using Digital Phase Demodulation and Injection Locked Lasers for NDE", PhD Dissertation, Texas A&M University, (1995).

APPENDIX A

MATLAB® PROGRAM FOR CALCULATION AND PLOT OF A THEORETICAL SINGLE-POINT-EXCITED RAYLEIGH WAVE

```
%This Routine plots a Theoretical single-point-excited Rayleigh Wave
c=3.010;% Rayleigh Wave velocity in steel (Km/s)
x=10;% Propagation distance (mm)
d=5; % Spot diameter (mm)
t=0:0.05:10; %time vector
Color = [0.0 0.0 0.0]; % White background
figure;
h=(x-c*t).*exp(-4*(x-c*t).^2/d);
plot(t,h);
 grid;
xlabel('time [us]')
ylabel('Relative Displacement');
%color(1,1,2);
title('Theoretical Single-point-excited Rayleigh Wave ');
```

APPENDIX B

MAPLE® PROGRAMS FOR PLOTTING OF DISPLACEMENT COMPONENTS , AND STRESS OF A RAYLEIGH WAVE

```
# Program for plotting of Rayleigh Wave Displacement Components
#
> u[R];#  and
> w[R];#  of a Rayleigh Wave
# Displacement u
> restart:
> with(linalg):
>

> lambda := nu*E/((1+nu)*(1-2*nu)):
> mu := E/(2*(1+nu)):
> k[l] := omega*sqrt(rho/(lambda+2*mu)):
> k[t] := omega*sqrt(rho/mu):
> q := sqrt(k^2-k[l]^2):
> s := sqrt(k^2-k[t]^2):
> omega := k/.205506086e-3:#    => Calculated from first problem
Warning, new definition for norm
Warning, new definition for trace
#
> u[r] := A*k*(exp(-q*z)-2*q*s*exp(-s*z)/(k^2+s^2))*sin(k*x-omega*t):
#

>
#
> DisplFn := Re(simplify(evalf(subs(s = %,q = %,A = .1,x = .1e-1,z =
> .1e-1,omega = %,E = .207e12,nu = .27,rho = 7850,k = 1,u[r])))):
#
#
> plot3d(DisplFn, z = 0 .. 2, t = 0 .. .2, labels = ["   z", "time
",
> "Displacement[z]  "], axes = ('boxed'), title = "x-direction
> Displacements in a Rayleigh Wave", style = hidden, color = red,
> orientation = [0, 90]);

>
# Displacement w
#
>
> restart:
> with(linalg):
>

> lambda := nu*E/((1+nu)*(1-2*nu)):
> mu := E/(2*(1+nu)):
> k[l] := omega*sqrt(rho/(lambda+2*mu)):
> k[t] := omega*sqrt(rho/mu):
> q := sqrt(k^2-k[l]^2):
> s := sqrt(k^2-k[t]^2):
> omega := k/.205506086e-3:
Warning, new definition for norm
Warning, new definition for trace
#
> w[r] := A*q*(exp(-q*z)-2*k^2*exp(-s*z)/(k^2+s^2))*cos(k*x-omega*t):
```

```
#
> DisplFnw := Re(simplify(evalf(subs(s = %, q = %, A = .1, z = .1e-1, x
> = .1e-1, omega = %, E = .207e12, nu = .27, rho = 7850, k = .5,
> w[r])))):
#
> plot3d(DisplFnw, z = 0 .. .1e-1, t = 0 .. .2, labels = ["   z", "time
>   ", "Displacement[z]  "], axes = ('boxed'), title = "z-direction
> Displacements in a Rayleigh Wave", style = hidden, color = red,
> orientation = [0, 90]);

# There is a phase shifting of  Pi/2;#   in the displacements
# components along x and z axis. Also the
# displacement amplitude values are bigger for z direction. This
# shifting makes the particle motion behave elliptically, being the
# motion in z direction the major of the semiaxis of the ellipse.
```

```
# Plotting of Rayleigh Wave Stress
> sigma[zz];
> restart:
> with(linalg):
>
Warning, new definition for norm
Warning, new definition for trace
> phi := A*exp(-q*z)*exp(I*k*x-omega*t);
#

> C := I*A*2*k*q/(k^2+s^2):#

> psi := C*exp(-s*z)*exp(I*k*x-omega*t);

               phi := A exp(-q z) exp(I k x - omega t)


                    I A k q exp(-s z) exp(I k x - omega t)
           psi := 2 --------------------------------------
                                    2    2
                                   k  + s

> dx := diff(phi,x,x);

> dz := diff(phi,z,z);
#

> dxz := diff(psi,z,x);#
#

                                  2
              dx := -A exp(-q z) k  exp(I k x - omega t)


                       2
              dz := A q  exp(-q z) exp(I k x - omega t)


                       2
                    A k  q s exp(-s z) exp(I k x - omega t)
           dxz := 2 ---------------------------------------
                                     2    2
                                    k  + s

> sigma[zz] := simplify(lambda*(dx+dz)+2*mu*(dz+dxz));
>
  sigma[zz] := A (-lambda k  - lambda k  s  + lambda q  k

         + lambda q  s  + 2 mu q  k  + 2 mu q  s

                   2
         + 4 mu q k  s exp(-z (-q + s))) exp(-q z + I k x - omega t)

           /   2    2
```

```
          /  (k  + s )
         /

# Elastic Constants
> lambda := nu*E/((1+nu)*(1-2*nu)):
> mu := E/(2*(1+nu)):
> k[l] := omega*sqrt(rho/(lambda+2*mu)):
> k[t] := omega*sqrt(rho/mu):
> s := sqrt(k^2-k[l]^2):
> q := sqrt(k^2-k[l]^2):
>
> omega := k/.205506086e-3:#               => Calculated previously
#
> StressFn := Re(simplify(evalf(subs(s = %,q = %,A = .1e-2,x = 0,omega
=
> %,E = .207e12,nu = .27,rho = 7850,k = .5,sigma[zz]))));

                           8
 StressFn := .1217606571 10  Re(exp(-2433.017969 z - 2433.017969 t))

#
> plot3d(StressFn,z = .1e-3 .. .1e-2,t = 0 .. .1e-2,labels = ["   z",
> "time    ", "Stress[zz]  "],axes = ('boxed'),title = "'Stress
> Amplitude for Rayleigh Wave",style = hidden,lightmodel = ('light2'));
```

APPENDIX C

MAPLE® PROGRAMS FOR MIRSKY AND HERRMANN DISPERSION CURVES

```
# Program for the Dispersion Theory of Mirsky and Herrmann for
Cylindrical Shells (in
# terms of Non dimensional Wave Velocities  s = c/c2)
# An approximate theory of nonaxially symmetric motions of thick,
# elastic, cylindrical shells, in which the effect of transverse normal
# stress is retained, is deduced from the three-dimensional theory of
# elasticity. The present theory contains, in addition to the usual
# membrane and bending terms, also the influence of rotatory inertia
and
# transverse shear deformation. Thus it may be specialized to a variety
# of shell, plate, and solid-cylinder equations. The propagation of
free
# harmonic waves in an infinite shell is studied on the basis of the
# present theory and the three-dimensional theory of elasticity.
# Excellent agreement between this theory and the three dimensional
# theory is obtained for the phase velocity for a wide range of the
# parameters involved.

# Frequency Equation
#
> restart:
> with(plots):
> with(linalg):
Warning, new definition for norm
Warning, new definition for trace
> F:= matrix(5,5):
> F[1,1] := 4*Pi^2*delta^2*(s^2-2*N)-m^2*n^2*(1+m^2/12):
> F[1,2] := m*Pi^2*delta^2/3*(s^2-2*N)+m^3*n^2/12:
> F[1,3]:=2*N*Pi*m*n*delta*(1+nu)*I:
> F[1,4]:=0:
> F[1,5]:=4*N*Pi*nu*m*delta*I:
> F[2,1]:=F[1,2]:
> F[2,2] := 1/3*Pi^2*delta^2*(s^2-2*N)-m^2*n^2/12-k[x]^2:
> F[2,3]:=0:
> F[2,4]:=Pi*N*m*n*delta/6*(1+nu)*I:
> F[2,5]:=-2*k[x]^2*Pi*delta*I:
> F[3,1]:=F[1,3]:
> F[3,2]:=0:
> F[3,3] := m^2*(k[theta]^2+2*N*n^2)*(1+m^2/12)-4*Pi^2*delta^2*(s^2-1):
> F[3,4] :=
> -m*Pi^2*delta^2*(s^2-1)/3-k[theta]^2*m*(1+m^2/12)-N*m^3*n^2/6:
> F[3,5]:=m^2*n*(1+m^2/12)*(k[theta]^2+2*N):
> F[4,1]:=0:
> F[4,2] := F[2,4]:
> F[4,3]:=F[3,4]:
> F[4,4] := k[theta]^2*(1+m^2/12)+N*m^2*n^2/6-Pi^2*delta^2*(s^2-1)/3:
> F[4,5]:=-k[theta]^2*m*n*(1+m^2/12)+N*m^3*n/6:
> F[5,1]:=F[1,5]:
> F[5,2]:=F[2,5]:
> F[5,3]:=F[3,5]:
> F[5,4]:=F[4,5]:
> F[5,5] :=
> -4*Pi^2*delta^2*(s^2-k[x]^2)+m^2*(1+m^2/12)*(k[theta]^2*n^2+2*N):
#
```

```
# The Characteristic Equation is obtained by calculating the
determinant
# of the frequency Equations where: m=h/R  , N = 1/(1-nu),s =
c/c2,delta
# = h/lambda; , and lambda; is the wavelength given by 2*Pi/alpha;,
# being alpha; the wavenumber. The phase velocity  c  is non
# dimensionalized by the shaer wave velocyty (c2) and is related to the
# natural frequency by omega = 2*Pi*c/lambda; . There are thus five
# roots for s^2;, and then Five possible modes exist for each case.
# Also for Axisymmetrical Motion n=0, and for flexural motion n=1, the
# adjustment coefficients k[x]; and k[theta]; are obtaining by
comparing
# the cutoff frequencies of the thickness shear modes in the axial and
# circumferential directions to those of  the so called exact theory.
# Now, introducing variable changes to have the equation in terms of
# frequency instead of s:
> FreqEqn := det(F):

# Data
#
> data:=proc()global h,R,m,nu,n,E,rho,k,N;
> h := 1:#7.2:
> R := 3:#33.2:
> m := h/R:
> nu :=0.30:
> n := 1:
> E = .207e12:
> rho = 7850:
> k[x] := evalf(Pi/sqrt(12));
> k[theta] := .9274127096:# ( For nu = .3;)
# N := 1/(1-nu);
# end:
# Mode I
#
> data():
> poly := evalf(subs(m = %,n = %,k[x] = %,k[theta] = %,N = %,nu = %,E =
> %,rho = %,FreqEqn));

> implicitplot(poly,delta = 0 .. 1,s = 0 .. 3.5,grid = [100,
> 100],thickness = 2,color = blue,style = point,axes = BOXED,titlefont
=
> ['HELVETICA', 'BOLD', 12],title = "Mirsky & Herrmann dispersion for
> Steel Pipe h = 7.2mm, R = 33.2mm");

>
> implicitplot(poly,delta = 0 .. .2,s = 0 .. 3.5,grid = [80,
> 80],thickness = 2,color = blue,style = point,axes = BOXED,titlefont =
> ['HELVETICA', 'BOLD', 12],title = "Mirsky & Herrmann dispersion for
> Steel Pipe h = 7.2mm, R = 33.2mm, (Zoomed View)");

>
>
```

```
# Program to plot the Transformed Mirsky-Herrmann Dispersion curves
# Frequency Spectra derived from Dispersion
# Theory of Mirsky and Herrmann for Cylindrical Shells
# An approximate theory of non-axially symmetric motions of thick,
# elastic, cylindrical shells, in which the effect of transverse normal
# stress is retained, is deduced from the three-dimensional theory of
# elasticity. The present theory contains, in addition to the usual
# membrane and bending terms, also the influence of rotatory inertia
and
# transverse shear deformation. Thus it may be specialized to a variety
# of shell, plate, and solid-cylinder equations. The propagation of
free
# harmonic waves in an infinite shell is studied on the basis of the
# present theory and the three-dimensional theory of elasticity.
# Excellent agreement between this theory and the three dimensional
# theory is obtained for the phase velocity for a wide range of the
# parameters involved.

# Frequency Equation
#
> restart:
> with(plots):
> with(linalg):
Warning, new definition for norm
Warning, new definition for trace
> F:= matrix(5,5):
> F[1,1]:=4*Pi^2*delta^2*(s^2-2*N)-m^2*n^2*(1+m^2/12):
> F[1,2]:=m*Pi^2*delta^2/3*(s^2-2*N)+m^3*n^2/12:
> F[1,3]:=2*N*Pi*m*n*delta*(1+nu)*I:
> F[1,4]:=0:
> F[1,5]:=4*N*Pi*nu*m*delta*I:
> F[2,1]:=F[1,2]:
> F[2,2]:=1/3*Pi^2*delta^2*(s^2-2*N)-m^2*n^2/12-k[x]^2:
> F[2,3]:=0:
> F[2,4]:=Pi*N*m*n*delta/6*(1+nu)*I:
> F[2,5]:=-2*k[x]^2*Pi*delta*I:
> F[3,1]:=F[1,3]:
> F[3,2]:=0:
> F[3,3]:=m^2*(k[theta]^2+2*N*n^2)*(1+m^2/12)-4*Pi^2*delta^2*(s^2-1):
> F[3,4] :=
> -m*Pi^2*delta^2*(s^2-1)/3-k[theta]^2*m*(1+m^2/12)-N*m^3*n^2/6:
> F[3,5]:=m^2*n*(1+m^2/12)*(k[theta]^2+2*N):
> F[4,1]:=0:
> F[4,2] := F[2,4]:
> F[4,3]:=F[3,4]:
> F[4,4] := k[theta]^2*(1+m^2/12)+N*m^2*n^2/6-Pi^2*delta^2*(s^2-1)/3:
> F[4,5]:=-k[theta]^2*m*n*(1+m^2/12)+N*m^3*n/6:
> F[5,1]:=F[1,5]:
> F[5,2]:=F[2,5]:
> F[5,3]:=F[3,5]:
> F[5,4]:=F[4,5]:
> F[5,5]:=-4*Pi^2*delta^2*(s^2-
k[x]^2)+m^2*(1+m^2/12)*(k[theta]^2*n^2+2*
> N):
```

```
#
# The Characteristic Equation is obtained by calculating the
determinant
# of the frequency Equations where: m=h/R  , N = 1/(1-nu),s =
# c/c[2],delta = h/lambda; , and lambda; is the wavelength given by
# 2*Pi/alpha;, being alpha; the wavenumber. The phase velocity  c  is
# related to the natural frequency by omega = 2*Pi*c/lambda; . There
are
# thus five roots for s^2;, and then Five possible modes exist for each
# case.
# Also for Axisymmetrical Motion n=0, and for flexural motion n=1, the
# adjustment coefficients k[x]; and k[theta]; are obtaining by
comparing
# the cutoff frequencies of the thickness shear modes in the axial and
# circumferential directions to those of  the so called exact theory.
# Now, introducing variable changes to have the equation in terms of
# frequency instead of s:
> FreqEqn := subs(s = omega*h*sqrt(2*rho*(1+nu)/E)/(2*Pi*delta),delta =
> omega*t*h/(2*Pi*d),det(F)):

# Data
#
> data:=proc()global h,R,m,nu,n,E,rho,k,N;
> h := 1:#7.2:
> R := 30:#33.2:
> m := h/R:
> nu :=0.30:
> #n := 1:
> n:=0:
> E = .207e12:
> rho = 7850:
> k[x] := evalf(Pi/sqrt(12));
> k[theta] := .9274127096:# ( For nu = .3;)
# N := 1/(1-nu);
# end:
# Dispersion Curves (omega; vs. time)
#
> data():
> # Substituting distances d1=0.01m y d2=0.03m from excitation point to
# FTI 1 and FTI 2 respectively
#
#
# poly1 := evalf(subs(d = .1e-1,m = %,n = %,k[x] = %,k[theta] = %,N =
# %,nu = %,E = %,rho = %,FreqEqn)):poly2 := evalf(subs(d = .3e-1,m =
%,n
# = %,k[x] = %,k[theta] = %,N = %,nu = %,E = %,rho = %,FreqEqn)):
> implicitplot(poly1,t = 0 .. .5e-1,omega = 0 .. 3.5,grid = [100,
> 100],resolution = 1000,thickness = 2,color = blue,style = point,axes
=
> BOXED,titlefont = ['HELVETICA', 'BOLD', 12],title = "Mirsky &
Herrmann
> dispersion for Steel Pipe h = 7.2mm, R = 33.2mm");

#
```

```
# Because implicitplot samples the function being plotted and builds
the
# final image from the sample, it will not detect discontinuities in
the
# function. Instead, the function is interpolated across the
# discontinuities.
> implicitplot(poly1, t = 0 .. .35e-1, omega = 0 .. .2, grid = [150,
> 150], thickness = 2, color = blue, style = point, axes = BOXED,
> titlefont = ['HELVETICA', 'BOLD', 12], title = "Mirsky & Herrmann
> dispersion for Steel Pipe h = 7.2mm, R = 33.2mm, (Zoomed View)");

>
> implicitplot(poly2,t = 0 .. .7e-1,omega = 0 .. .5,grid = [150,
> 150],thickness = 2,color = blue,style = point,axes = BOXED);

>
#
Warning, computation interrupted
```

```
# Calculation of k[theta];
> restart:
> eqkt:=abs(sqrt((n^2-k^2)*(1-k^2)))-n*(1/2*k^2-1)^2=0;
> n:=sqrt((2*(1-nu))/(1-2*nu));

      eqkt := sqrt(| (n  - k ) (1 - k ) |) - n (1/2 k  - 1)  = 0


                                    1 - nu
                    n := sqrt(2) sqrt(--------)
                                   1 - 2 nu

# In this case a value of Poisson's ratio of 0.3 is considered. Also
# valid values are between 0< k[theta];<1
> k[theta] := solve(subs(nu = .3,n = %,eqkt),k);

  k[theta] := -.00003146337980, .00003146337980, -.9274127096,

        .9274127096, -1.033389292, 1.033389292, -1.804887977,

        1.804887977

> for i from 1 to 8 do
>   s[i]:=type(k[theta][i],nonneg):
>   if (s[i]=true) then
>     if (k[theta][i]<1) and (k[theta][i]>0.01) then
>       kt:=k[theta][i]:
>     fi
>   fi
> od:
> k[theta]:=kt;

                       k[theta] := .9274127096
```

APPENDIX D

MATLAB® PROGRAMS FOR GABOR WAVELET TRANSFORM

```
This Program performs data analysis of a dual Chanel setup:
% Discrete Fourier Transform  (DFT)
% Gabor Wavelet Transform  (GWT)
% and Dispersion Spectrum
clear all;
DataFile=input('Name of Data File ');
t=clock;
x=load ([DataFile '.txt']);
gamma=sqrt(2/log(2))*pi;
ndt=200; % No. of divisions in time scale
ndf=100; %No. of divisions in frequency
figure;subplot(2,1,1);
plot(x(:,2));title(['Waveform Chanel 1']);
A=[x(:,1),x(:,2)];   % time and voltage Chanel 1
subplot(2,1,2);
Denoise(A,DataFile,1);
dx=load(['Dnx.txt']);
A=[x(:,1),dx(:,1)];
clr=[0,0,0]
dft(B,1,5e7,clr,DataFile);
Gdual(A,ndf,ndt,gamma,DataFile,1);
if size(x,2)==3
   figure;plot(x(:,3));title(['Waveform Chanel 2']);
   B=[x(:,1),x(:,3)];   % time and voltage Chanel 2
   Denoise(B,DataFile,1);
   dx=load(['Dnx.txt']);
   B=[x(:,1),dx(:,1)];
   clr=[0,0,0]
   dft(B,1,5e7,clr,DataFile);
   Gdual(B,ndf,ndt,gamma,DataFile,2);
end
disp('------Elapsed time in minutes -------');
tt=etime(clock,t)/60

%___________________________________________________________________________

%Gabor wavelet transform and Plotting of Arrival times

function WT=GW(x,nf,nt,gamma,Filename,FTI)

if (nargin ~= 6)
        disp('Check Arguments:data in x, step distance, Frequency range, Gamma,
File Name and FTI#')
       return
end

N=length(x);                            %number of data

dt=x(3,1)-x(2,1);                       %sampling time

%X=x(:,2)';

sam_freq=1/dt;

%disp('------The Maximum Frequency of the signal[Hz]-------');

Max_frequency=sam_freq/2;
fprintf('\nThe Maximum Frequency of the signal %8g Hz \n',Max_frequency);
fr=4e6;%Max_frequency %upper frequency limit
fprintf('\nSelected Frequency range : fr = %8g Hz \n',fr);
```

```
if (fr > Max_frequency)
       disp('Frequency range, should not be bigger than Maximum frequency
range');
       return;
end

M=fr*N/Max_frequency;

st=dt*N/nt;% 10;%step in time
fprintf('\ntime interval: %8g sec \n',st);


sf=fr/nf;
fprintf('\nfrequency interval: %8g Hz \n\n',sf);

%startTime = time sweep: starts at "n" times "step distance" msec

% Variable "factor" establishes the time length basis for calculation
% i.e. if factor=1, the whole recorded time is used,
% if factor=0.5, only half of the available time recordrd is used.

if FTI==1
   startTime=x(1,1);%1*sd;
   finalTime=x(N,1);
   X=x(1:N,2)';
   factor=1;
else
   startTime=x(1,1);%40*sd;
   finalTime=x(N,1);
   X=x(1:N,2)';
   factor=1;
end

startFreq=5*sf;%0.001;%sd;%Min_frequency_range;%1*sd

W=startFreq:sf:fr;

a=1./W;
G=gamma;
clr='b*'
fprintf('\nGamma = %g \n',G);
ite=0;
disp('                               COMPLETED:    ');
for b=startTime:st:dt*N*factor;
    ite=ite+1;
    fprintf('\b\b\b\b%3.0f%%',ite*100/nt);
    m=0;
    for k=startFreq:sf:fr;
       m=m+1;
       y(m,ite)=sum(1/sqrt(a(m)).*X.*1.883/sqrt(G).*exp(-(2*pi/G)^2/2*(((0:N-
1)*dt-b)./a(m)).^2).*cos(2*pi*((0:N-1)*dt-b)./a(m))*dt);
    end
    Mag=abs(y);
end
Timeiters=ite-1
FreqIters=m
M
T=[startTime:st:N*dt*factor];%.*1e6; %microseconds
%//To find out the maximum wavelet coefficients and corresponding time;
[W_max, row_index]=max(Mag');
```

```
K=1:length(W);
Arrival_time=T(1,row_index(1,K));
Freq_Arrive=[W,Arrival_time];
finalTime=T(1,ite-1);
finalFreq=W(1,m);
FitT=polyfit(W,Arrival_time,5);
ffit=linspace(0,finalFreq,m); %fitting frequency
TimeFit=FitT(1)*ffit.^5+FitT(2)*ffit.^4+FitT(3)*ffit.^3+FitT(4)*ffit.^2+FitT(5)
*ffit+FitT(6);%5th order
%___________________________________________________________________________
%Plotting of Arrival time
    figure;
    plot(Arrival_time*1e6,W*1e-6,clr);grid;%real data
    plot(Arrival_time*1e6,W*1e-6,clr,TimeFit*1e6,ffit*1e-
6,'r.','linewidth',2);grid; %fitted
    xlabel('Arrival Time [us]');ylabel('Frequency[MHz]');
    title(['Arrival Time of ',Filename, ' G= ',num2str(G)]);
%___________________________________________________________________________

if FTI==1
   Tdistance=0.02; %travel distance(m) for FTI 1
      else
      Tdistance=0.04; %travel distance(m) for FTI 2
end
Gvel=Tdistance ./ (TimeFit*1e3); %Group Velocity
%___________________________________________________________________________
%Plotting of Group Velocity
    figure;
    axis manual;
    plot(Tdistance./(Arrival_time*1e3),W*1e-6,'b*',Gvel,ffit*1e-6,'r-
','linewidth',2);
    xlabel('Velocity [10e3 m/s]');ylabel('Frequency[MHz]');grid;
    title(['Group Velocity ', Filename,' FTI ',int2str(FTI),'G= ',num2str(G)]);
    axis tight;
%___________________________________________________________________________
figure;
%contour(T*1e6,W*1e-6,Mag,8);
surf(T*1e6,W*1e-6,Mag);
shading interp;
view(2);grid;%colorbar;
xlabel('Time[usec]');
ylabel('Frequency[MHz]');
zlabel('Magnitude');
title(['GWT ', Filename,' FTI ',int2str(FTI),'G= ',num2str(G)]);
axis tight;
%__________________________________________________________________________
% Discrete Fourier Transform
function DFT=DFT(x,sd,fr,cp,Filename)
%cp is the plot color
if (nargin ~= 5)
        disp('Please load Data Set,Step distance, Frequency range, color and
File Name')
       return;
end

N=length(x);                              %number of data
dt=x(2,1)-x(1,1);                         %sampling time
X=x(:,2)';
sam_freq=1/dt;
disp('------The Maximum Frequency of the signal[Hz]-------');
```

```
Max_frequency=sam_freq/2
step_dist=sd;
w=fr;
if (w > Max_frequency)
       disp('Frequency range, w, should not be bigger than Maximum frequency
range');
       return;
end

M=2*w*N/sam_freq;
W=sam_freq*(0:step_dist:ceil(M/2))/N;

     m=0;
 for k=0:step_dist:(M+1)/2;
     m=m+1;
     Mag(m)=abs(sum(X.*exp(-i*2*pi*(0:N-1)/N*k)));
 end
 Color = [0.0 0.0 0.0]; % White background
 figure;
 set(plot(W,Mag),'Color',cp);
 grid;
xlabel('Frequency[Hz]')
ylabel('Magnitude');
%color(1,1,2);
title(['DFT ',Filename]);

%_____________________________________________________________________________
% Routine used to De-noise signal
function [denx]= DEnoise(x,Filename,FTI);
s=[x(:,1),x(:,2)]; %Time and voltage channel 1
figure;
subplot(2,1,1);
plot(s);title(['Original signal',Filename,'FTI ',int2str(FTI)]);
%use wpdencmp for signal de-noising
n=length(s);
thr=sqrt(2*log(n*log(n)/log(2)));
xwpd=wpdencmp(s,'s',4,'sym4','sure',thr,1);
Dn=xwpd(:,2)
%figure;
subplot(2,1,2);
plot (Dn);
title(['denoised signal by wavelet packets']);
file_DEnx=['Dnx.txt '] %File name to write Denoised Signal
eval(['save ' file_DEnx 'Dn  -ascii']);
```

VITA

Martín Eduardo Baltazar-López was born in México City, México on August 19, 1966. He attended high school at CECyT #1 of the National Politechnical Institute (IPN). Then he enrolled at the Instituto Tecnológico de Aguascalientes where he completed his undergraduate studies as Industrial Mechanical Engineer in December of 1989. He was involved in automotive mechanics, small engine and construction equipment maintenance working as a Technical Manager at ESTEC, Aguascalientes, Mex. from 1988 to 1990. He started his graduate studies in August of 1990 at the Centro Nacional de Investigación y Desarrollo Tecnológico (CENIDET), Cuernavaca Mor., México. During his graduate studies he served as an assistant professor and then as a titular professor, teaching courses in Mechanical Engineering. A Masters of Science in mechanical engineering specialized in design was awarded to Martín E. Baltazar-López in August 1994. In 1997 he was awarded a scholarship by the government of México through the Secretaría de Educación Pública (SEP) and the Consejo Nacional de Ciencia y Tecnología (CONACYT) to carry out his doctoral studies in Interdisciplinary Engineering at Texas A&M University, College Station TX. He worked as a research assistant from September 2001 to August 2003 at the Dynamic Photomechanics Laboratory of Texas A&M University. He specialized in mechanical design and experimental mechanics with emphasis on Laser Ultrasonics. His permanent address is: Ignacio Lomas No. 201, San Marcos, Aguascalientes, Ags. C.P. 20070, México.